SEMMELWEIS EGYETEM

DOKTORI ISKOLA

Ph.D. értekezések

3069.

TURBUCZ MÁTÉ

A támasztó és mozgató szervrendszer működésének fiziológiája
című program

Programvezető: Dr. Szőke György, egyetemi tanár

Témavezetők: Dr. Éltes Péter Endre, gerincsebész szakorvos, laborvezető és

Dr. Lazáry Áron, főigazgató helyettes, gerincsebész főorvos

IN SILICO INVESTIGATIONS OF SURGICAL INTERVENTIONS IN THE THORACOLUMBAR AND LUMBOPELVIC REGION

PhD thesis

Máté Turbucz

Semmelweis University Doctoral School

Surgical Medicine Division

Supervisors: Péter Endre Éltes, MD, Ph.D
Áron Lazáry, MD, Ph.D

Official reviewers: László Rudolf Hangody, MD, Ph.D
Fabio Galbusera, Ph.D

Head of the Complex Examination Committee:
Miklós Szendrői, MD, D.Sc

Members of the Complex Examination Committee:
Gábor Skaliczki, MD, Ph.D
Károly Pap, MD, Ph.D

Budapest
2024

TABLE OF CONTENTS

LIST OF ABBREVIATIONS

Abbreviation	Definition
2D	Two-dimensional
3D	Three-dimensional
AF	Annulus fibrosus
BMD	Bone mineral density
CEP	Cartilaginous endplate
CLR	Closed-loop reconstruction
CT	Computed tomography
DICOM	Digital imaging and communications in medicine
FE	Finite element
FEA	Finite element analysis
FJF	Facet joint force
FRR	Four-rod reconstruction
GAP	Global alignment and proportion
GS	Ground substance
HD	Hausdorff distance
HU	Hounsfield Unit
ICR	Improved compound reconstruction
IDP	Intradiscal pressure
ISS	Iliosacral screw
IVD	Intervertebral disc
IVR	Intervertebral rotation
L1, L2, L3, L4 and L5	First, second, third, fourth and fifth lumbar vertebrae
LBM	Literature-based model
LPDR	Lumbopelvic distance reduction
LPRT	Lumbopelvic reconstruction technique
MRF	Multiple-rod fixation
MRI	Magnetic resonance imaging
NP	Nucleus pulposus
PACS	Picture archiving and communication system
PEEK	Polyetheretherketone
PJK	Proximal junctional kyphosis

PRF	PEEK rod fixation
PSM	Patient-specific model
QCT	Quantitative computed tomography
RID	Relative interfragmentary displacement
ROM	Range of motion
S1 and S2	First and second sacral vertebrae
SFT	Semirigid fixation technique
SIJ	Sacroiliac joint
SK	Segmental kyphosis
SRR	Sacral rod reconstruction
STL	Stereolithography
T6, T7, T8, T9, T10, T11 and T12	Sixth, seventh, eighth, ninth, tenth, eleventh and twelfth thoracic vertebrae
TISS	Transverse iliosacral screw
TPH	Transverse process hooks
TRF	Titanium rod fixation
UIV	Upper instrumented vertebra
VS	Vertical stiffness

LIST OF NOTATIONS

Notation	Definition
C10, C01, D1	Hyperelastic material constants
C3D4	Four-node tetrahedral element
C3D5	Five-node tetrahedral element
C3D6	Six-node tetrahedral element
C3D8H	Eight-node tetrahedral hybrid element
E	Young’s modulus
SPRINGA	Axial spring element
T3D2	Linear truss element
ν	Poisson’s ratio
ρ	Density

1. INTRODUCTION

1.1. In silico medicine and finite element analysis

In general, investigation of the human body encompasses methodologies conducted in vitro, in vivo, or in silico. In vitro denotes the execution of procedures within a controlled environment external to a living organism. In vivo involves experimentation utilising a complete, living organism instead of an incomplete or deceased organism. The term in silico denotes experiments conducted on a computer or via a computer simulation (1).

The term “in silico medicine” is frequently employed to denote the translational application of modelling and simulation in diagnosing, treating, or preventing diseases (2). Emerging as a developing science, in silico medicine generally employs synthetic and cellular biology, tissue engineering, animal experimentation, and various branches of experimental biophysics, including biomechanics, bioelectricity, and biochemistry (3).

This PhD thesis discusses biomechanics-based in silico medicine, which employs the finite element (FE) method. The FE method is a numerical technique used to approximate solutions to partial differential and integral equations, enabling the analysis of complex structures by starting from their material properties (2).

The first biomechanical application of finite element analysis (FEA) was reported by Brekelmans et al. in 1972 (4). Their study demonstrated the FE method's suitability for assessing stresses and strains in complex structures under different loading conditions. Subsequently, in 2002, Fagan et al. conducted a comprehensive review of the contributions of FEA to the understanding of the spine, its behaviour in healthy, diseased or damaged states (5). Fagan emphasised the FE method's ability to reduce reliance on animal and cadaver experiments and presented FEA as a valuable adjunct to clinical studies (5). Since Fagan’s study, FEA has been recognised as an effective predictive tool for assessing spinal biomechanics (6). Applying FEA can eliminate the difficulties, limitations and ethical concerns associated with in vitro experiments. Furthermore, FEA is more cost-effective than in vivo or in vitro experimental studies (5,7). The possibility of employing complex load cases and boundary conditions allows the investigation of biomechanical parameters that are difficult to measure by experimental methods (8). Recently, in silico studies using the FE methods have become more widespread (2,9,10), enabling patient-specific investigations and the development of new treatments and medical devices (11–13).

1.2. Patient-specific and literature-based finite element models

Musculoskeletal FE models in the literature vary in patient-specificity depending on the modelling strategy (7,14,15). Two main bone material modelling strategies are used: the "hybrid patient-specific" approach, where geometry relies on the patient's medical imaging data while the homogenous material properties are derived from literature, and the "fully patient-specific" approach, where both the geometry and heterogenous bone material properties are defined based on medical images (CT, QCT, MRI).

This PhD thesis first presents the development and validation of a "fully patient-specific" FE model of the lumbar spine. For the thoracolumbar and lumbopelvic regions, the "hybrid patient-specific" modelling approach was utilized. In the sacropelvic region, both methods were employed and compared.

The "fully patient-specific" models can be used to investigate the load-fracture mechanism of bony structures, either with single vertebra models (14,16,17) or motion segments (15,18). Crawford et al. created a voxel-based vertebral body FE model to investigate vertebral compressive strength with CT-derived bone material properties and geometry (17). Costa et al. assessed the biomechanical characteristics of vertebrae with lytic lesions using a subject-specific FE model (14). Xiao et al. developed an FE model of the L4–L5 lumbar motion segment using patient-specific bone material properties to analyse its kinematics by measuring the range of motion (ROM) and comparing it with experimental results (15). The effects of medical imaging-based bone material properties were evaluated in the literature by comparing their results with simulations employing literature-based material properties. O'Reilly and Whyne compared geometrically parametric models with "fully patient-specific" models to analyse the strain and displacement patterns in healthy and metastatically involved vertebrae in a T6-T8 spinal motion segment. However, only the trabecular bone's material property was assigned based on the CT scans. They found that both the geometry and material properties have a notable effect on vertebral strain and displacement (19). Sapin-de Brosses et al. compared the effect of medical imaging-derived bone material definition with literature-based bone material characteristics using an FEA of fourteen vertebrae. Their study concludes that applying patient-specific bone material properties reduces the relative error of the failure load estimation (20).

1.3 Clinical needs finding

The National Center for Spinal Disorders (Budapest, Hungary) is a recognized regional clinical institute specializing in the treatment of spinal conditions. The extensive clinical observations from surgeries related to spinal deformities, tumours, or trauma provide valuable insights for in silico investigations. This approach aligns with the principles of the Stanford Biodesign program, a pioneering life science initiative that emphasizes training innovators to focus on clinical needs (21). Unlike traditional approaches that often start with a promising technology, the Stanford Biodesign process prioritizes identifying and characterizing the clinical need first. By adopting this clinical need-driven methodology, the work presented in this PhD dissertation aims to address some specific questions encountered in the everyday clinical practice.

1.3.1. Proximal junctional kyphosis

In recent years, the upward shift in age demographics has led to a significant increase in the prevalence of adult spinal deformity (22). In treating patients with adult spinal deformities, the application of surgical fixation techniques has grown significantly. However, these surgical techniques remain a cause for concern as they are associated with increased revision and complication rates (22). Proximal junctional kyphosis (PJK) is a complication with an incidence rate ranging from 17% to 39% within two years of surgery (23). PJK is an abnormal kyphotic deformity affecting the vertebral components proximal to the upper instrumented vertebra (UIV). PJK is described by the segmental kyphosis (SK) defined by the proximal junctional Cobb angle measured between the UIV and the vertebra two levels cranial to the UIV (UIV+2) (24). PJK occurs if the SK between the UIV and UIV+2 is at least 10° or if the SK increases by at least 10° after surgery. In more severe cases, PJK includes vertebral subluxation, vertebral body fracture, implant failure, damage to the posterior ligament complex, or adjacent level degeneration (25). Various patient-specific risk factors have been linked to PJK, such as older age, higher body mass index, lower bone mineral density (BMD), and comorbidities (26). Surgery-related risk factors have also been identified, such as the position of the UIV, given that PJK is more likely to occur in the lower thoracic and thoracolumbar regions (26). Furthermore, a high construct rigidity, a high degree of corrected deformity, and the number of fused vertebrae were also considered surgical risk factors (27). In addition, the quantitative GAP score

was found to be an efficient tool for predicting mechanical complications such as PJK (28). Besides these, the sudden change in rigidity between the instrumented and non-instrumented segments was also identified as a contributing (29). To address this problem, various semirigid fixation techniques (SFTs) (29) were introduced in the literature, such as transverse process hooks (TPH) (30), transition rods (31), or the use of PEEK instead of metallic alloys (32). The purpose of such implants is to provide a more gradual transition to normal motion at the UIV level following long instrumented posterior spinal fusion, thereby reducing the probability of developing PJK (33). Previously, various in vitro experiments were performed to investigate the effect of different spinal constructs on the development of PJK. Thawrani et al. analysed the biomechanical effect of placing TPHs at the UIV level (30) and found that TPHs can provide a more gradual transition in motion than more rigid constructs and thus reduce the incidence of postoperative PJK (30). Viswanathan et al. published their findings that the SFTs could effectively extend the transition zone and reduce peak stress at the UIV level of long-segment thoracolumbar fixations (34). Doodkorte et al. analysed different SFTs, such as TPHs, and the use of sublaminar tapes at the cranial end of the construct (33). They found a more beneficial transition in mobility at the junctional levels in all semirigid constructs compared to the conventional pedicle screw fixation (33). Besides the in vitro measurements, FE analyses were also used to understand the biomechanical background of PJK. Bess et al. evaluated the effect of posterior anchored polyethylene tethers and concluded that the tethers provided a more gradual transition in ROM and reduced the load in the posterior ligament complex and in the pedicle screws at the UIV level (35). Zhang et al. investigated the application of PEEK rods and found that the risk of PJK is lower in the case of SFTs (36). As pointed out, these studies agree that the biomechanical assessment of the instrumented spinal segments may help predict and prevent postoperative PJK. In part II of this PhD thesis, two different SFTs were investigated and compared to the conventionally used titanium rod fixation (TRF) technique. The multiple-rod fixation (MRF) technique, based on the arrangement of thinner titanium rods in a shield pattern, was introduced by Farkas and Varga in 2002 (37). MRF aims to improve angular mobility while maintaining the stability resulting from the titanium material (37). The PEEK rod fixation (PRF) technique consists of PEEK material at the cranial end of the construct to decrease its rigidity. Among the previous in vitro and in silico studies of SFTs, the MRF technique

has not been previously investigated in relation to PJK. Furthermore, the effect of PEEK material at the cranial end of the construct on mobility and load distribution in long posterior spinal fixations has not been previously analysed.

1.3.2. Sacral fractures and their impact on biomechanical properties

The sacrum serves as a biomechanical keystone by transmitting the load of the upper body to the lower extremities (38). Sacral fractures are usually caused by high-energy traumas such as road accidents or falls from a greater height. Due to its biomechanical properties as a load-transition zone, sacral fractures are subjected to increased mechanical stress and can lead to an unstable pelvic ring (39,40). These traumatic, non-osteoporotic sacral fractures occur with a relatively low incidence of 2.1 per 100,000 (41). However, Bydon et al. reported a fivefold increase in traumatic sacral fractures between 2002 and 2011 (42). The exact reason remains unclear. Potentially, the increased availability of CT scans could enhance the detection of sacral injuries (38,42). Although sacral fractures are recognised more frequently and treated surgically (38), there is still debate regarding optimal surgical management (43). The surgical options include iliosacral screw (ISS) and transverse iliosacral screw (TISS) (44), posterior plating (45), transiliac internal fixator (46), unilateral or bilateral triangular fixation (47,48) and S2-alar-iliac techniques (49,50). Especially in cases of minor or non-displaced sacral fractures, achieving high stability with as little invasiveness as possible is crucial (38). Therefore, ISS and TISS emerge as suitable techniques from all those described (44). Osteosynthesis can typically be performed through a small lateral incision, percutaneously, and minimally invasively (51). Furthermore, the sacroiliac joint (SIJ) usually characterised by robust cortical bone, provides good screw purchase with a screw trajectory perpendicular to the fracture plane (38). This allows for fracture compression, potentially leading to improved fracture healing according to AO principles (52). However, screw placement requires a thorough understanding of the sacral anatomy as individual morphological variations exist (53). Screw loosening and hardware failure have been reported at relatively high rates, at 11.8% - 17.3%, with uncertain clinical relevance (44). Several biomechanical studies have been conducted to assess fixation techniques used for sacral fracture treatment (43,48,54–58). Acklin et al. and Hu et al. compared ISS fixation with different lumbopelvic fixations for treating Denis Type II sacral fractures (48,59). They concluded that lumbopelvic fixations are biomechanically more stable. However, such fixation techniques significantly

compromise the mobility of the lumbar region and require a larger surgical approach (60). Zhao et al. compared three ISS and three TISS configurations to evaluate their biomechanical stability for treating unilateral transforaminal sacral fractures, while Fu et al. analysed the same configurations in the case of bilateral sacral fractures (54,55). Both studies concluded that two TISSs at the S1 and the S2 levels are biomechanically the most stable configuration. Previous biomechanical studies employing FE analysis assumed identical bone quality at the S1 and S2 levels and employed averaged, homogeneous bone material properties (43,54–57,59,61). However, the study by Radley et al. revealed that bone quality significantly varies between the S1 and S2 vertebral bodies (62). Their analysis of 50 pelvic CT scans revealed significant variations in bone quality between the S1 and S2 vertebral bodies, with a 28.4 % lower regional BMD in S2. Their result indicates the need for locally defined bone material properties when assessing sacral fracture's biomechanical characteristics. In a lumbar spine FE study, Turbucz and Pokorni et al. have revealed that medical imaging-based bone material properties are more accurate for predicting internal mechanical parameters, although its use is coupled with increased computational cost (63). However, regarding sacral fracture fixations, no previous biomechanical in silico study included patient-specific bone material properties.

1.3.3. Lumbopelvic reconstruction techniques after total sacrectomy

The lumbosacral complex serves as a biomechanical keystone, transmitting the forces from the axial skeleton to the lower limbs (64,65). It plays a crucial role in maintaining an upright posture and enabling the ability to walk (66). If this region is affected by malignant tumours, surgical interventions invariably emerge as the preferred treatment strategy (67–69). However, the surgical treatment of sacral tumours is technically demanding and necessitates careful consideration of anatomical and biomechanical factors (65,70,71). En bloc resection of a sacral tumour with a sufficiently wide oncological margin significantly influences the biomechanics of the lumbopelvic region (65), as it disrupts the continuity between the pelvis and spine (64). Therefore, lumbopelvic reconstruction is essential to provide sufficient biomechanical stability, enabling load-bearing and patient mobilization (65,70,72,73).

For lumbopelvic stabilization, the Harrington rod technology was initially employed, although it rarely provided sufficient stability to enable bony fusion (68,74,75). Since the 1990s, the predominant approach shifted to the Galveston-rod technique and its

modifications. These techniques included pedicle and iliac screws connected with rods (76–81). Technical progress in lumbopelvic reconstruction techniques (LPRTs) has been continuous since the early 2000s. In 2003, Kawahara et al. introduced the sacral rod reconstruction (SRR) technique, including a horizontal sacral rod attached to L5, combined with conventional posterior stabilization components (82). They also presented that SRR has a reduced risk of hardware failure and screw loosening (82). In 2006, Shen et al. presented the four-rod reconstruction (FRR) technique, employing four longitudinal spinal rods (78). The FRR technique has been analysed in numerous in vitro and in silico studies (74,83–87), revealing significantly reduced lumbopelvic motion compared to conventional LPRTs (84,85). In 2009, Varga et al. introduced the closed-loop reconstruction (CLR) technique, consisting of a single U-shaped rod, for lumbopelvic stabilization (67,88). The CLR technique is a non-rigid fixation approach, as concluded by a comprehensive six-year retrospective clinical investigation (88). Nevertheless, this non-rigidity did not cause hardware failure or limit the bony fusion between the ileum and the lumbar spine (88). Following its introduction, the CLR technique gained acceptance (89) and underwent further development (90). Furthermore, in 2011, Cheng et al. developed the improved compound reconstruction (ICR) technique, which anteriorly included the horizontal sacral rod and a bilateral fibular graft construct, while the posterior aspect was identical to the FRR technique (83). The ICR technique has been investigated in vitro (83,87) and in silico (74), demonstrating high structural stability.

Previous investigations have unveiled that common mechanical failure modes of the LPRTs include screw-loosening and hardware failure (74,82). These have been associated with the concentrated stress at the screw-bone interface and within the rods (76). Bony fusion between the lumbar spine and the iliac bones is crucial for long-term clinical stability and better quality of life following a total sacrectomy (65,70). Reducing the distance between the bonny host surfaces - the caudal vertebral body and the iliac wings – increases the probability of successful bony fusion according to the biological process of bone formation. Furthermore, reducing this distance can also result in less soft tissue tension, leading to better wound healing. Lumbopelvic distance reduction (LPDR) is often achieved by pulling down the L5 vertebra and rotating the iliac wings towards the lumbar spine (70). Despite these mentioned clinical benefits of LPDR, the biomechanical impact of this procedure has not been previously investigated in the existing literature.

2. OBJECTIVES

The main objective of this PhD thesis was to perform in silico investigations to provide scientific evidence for the clinicians performing surgical procedures at the National Center for Spinal Disorders. These in silico studies aimed to understand the biomechanics related to various surgical procedures and provide supporting evidence for clinicians.

1. The aim of part I was to introduce the validation processes of different healthy anatomical regions, such as the lumbar spine, the thoracolumbar spine and the pelvis. In addition, the patient-specific bone material assignment technique is presented. The outcomes of the finite element model underwent comparison with data from in vivo and in vitro and established in silico results taken from the literature, aiming to validate the healthy anatomical finite element models.
2. The aim of part II was to investigate proximal junctional kyphosis, a frequently encountered mechanical complication following long posterior spinal fusion surgeries. While existing literature has identified various risk factors, biomechanical investigations suggest that a significant contributor to proximal junctional kyphosis is the sudden change in mobility between the instrumented and healthy spinal segments. This section of the thesis aims to evaluate the biomechanical impact of three spinal fixation techniques, one rigid and two semirigid, on the development of proximal junctional kyphosis.
3. The aim of part III was to assess and compare the biomechanical effectiveness of three iliosacral screw and three transverse iliosacral screw fixation techniques employed in the treatment of unilateral AO Type B2 (Denis Type II) sacral fractures. This evaluation was conducted utilising both literature-based and patient-specific bone material properties using the finite element method.
4. The aim of part IV was to assess and compare the biomechanical characteristics of four lumbopelvic reconstruction techniques. This evaluation considered the impact of lumbopelvic distance reduction. Although many lumbopelvic reconstruction techniques have been previously analysed, the biomechanical effect of lumbopelvic distance reduction has not been investigated yet.

Contributions of this thesis work:

1. Part I of this PhD thesis work is based on the scientific article entitled *Development and Validation of Two Intact Lumbar Spine Finite Element Models for In Silico Investigations: Comparison of the Bone Modelling Approaches* by Turbucz and Pokorni et al. Ágoston Jakab Pokorni contributed to developing the literature-based FE model of the healthy lumbar spine. He shares co-first authorship in the aforementioned publication detailing the development and validation process of the lumbar spine FE models (63). In this PhD thesis work, only the development and validation of the patient-specific FE model are presented.
2. Part II of this PhD thesis work is based on the scientific article entitled *Can semirigid fixation of the rostral instrumented segments prevent proximal junctional kyphosis in the case of long thoracolumbar fusions? A finite element study* by Turbucz and Fayad et al. Jennifer Fayad contributed to developing the thoracolumbar spine FE model. She shares co-first authorship in the aforementioned publication, presenting the FE-based investigation on the onset of PJK (91).

3. METHODS

3.1. Part I. Development and validation of the healthy finite element models

In all in silico investigations presented in this PhD thesis, FE models were developed using the quantitative computed tomography (QCT) scans (Hitachi Presto, Hitachi Medical Corporation, Tokyo, Japan) of a 24-year-old male without any musculoskeletal pathology. The studies involving the human participant underwent review and approval by the National Ethics Committee of Hungary and the National Institute of Pharmacy and Nutrition (reference number: OGYÉI/163-4/2019). The individual provided written informed consent for the publication of potentially identifiable images or data in this article. All methods were conducted following relevant guidelines and regulations.

The QCT scans with a voxel size of $0.6 \times 0.6 \times 0.6$ mm^3 were employed to capture the geometry of the FE models. This process followed a previously reported imaging protocol (92). For each specific FE analysis, the QCT dataset (in DICOM extension) was sourced from the National Center for Spinal Disorders's PACS and subsequently anonymised using Clinical Trial Processor software (Radiological Society of North America) (93). This approach ensured consistency across all investigations.

All the FE simulations presented in this thesis work were solved using Abaqus Standard (Dassault Systemes, Vélizy-Villacoublay, France).

3.1.1. Development of the healthy lumbar spine finite element model

The 2D images from the QCT scans were imported into Materialise Mimics software (Materialise, Leuven, Belgium) to generate a patient-specific surface geometry model through a Hounsfield Unit-based segmentation process. Subsequently, the surface mesh was exported to 3-Matic software (Materialise, Leuven, Belgium) in STL format. To enhance mesh quality and eliminate spikes and cavities on the vertebral surfaces, the surface mesh underwent smoothing and remeshing with a target edge length of 1 mm (94) (Figure 1a).

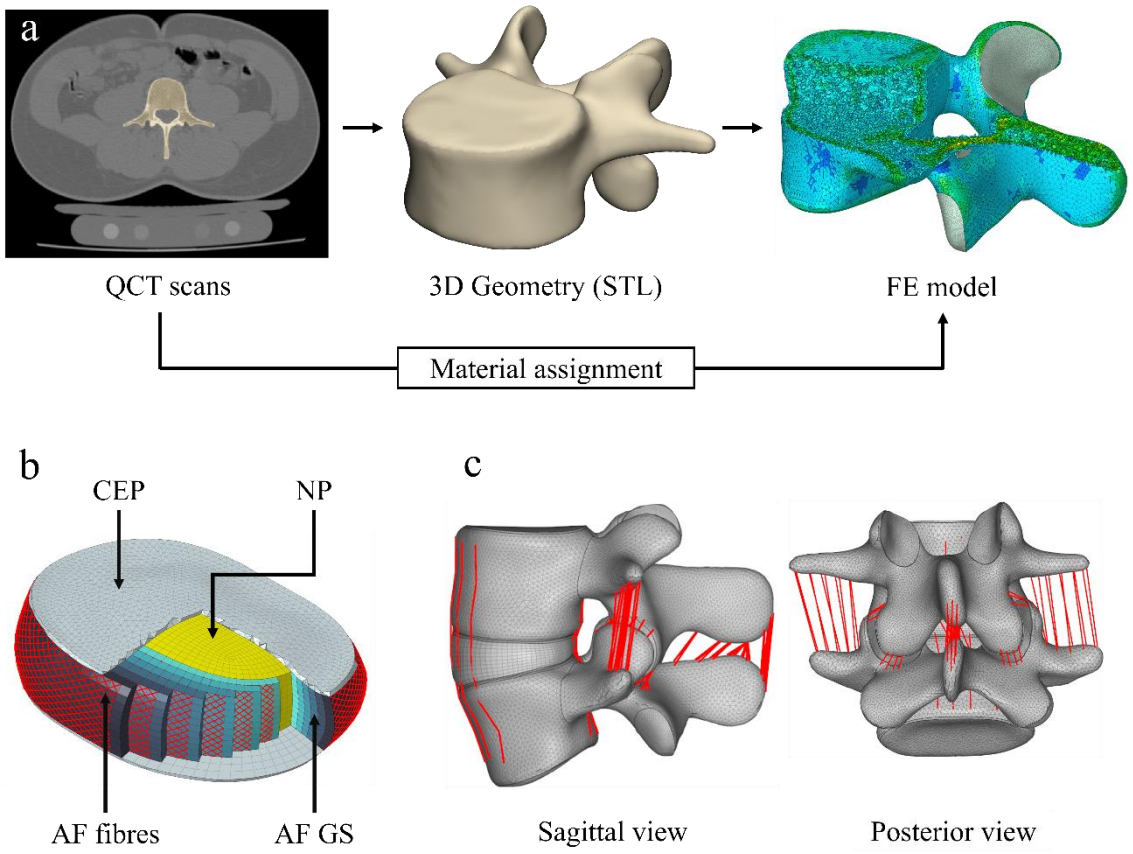

Figure 1. a) The geometry of the FE model was defined by segmentation from the QCT scans. The bone material properties were assigned according to the HU values. b) The FE model of the IVD includes the CEP, the NP, the AF GS, and the AF fibres. c) Ligaments are illustrated on the L4–L5 FE model in sagittal and posterior views.

In the lumbar spine FE model, vertebrae were meshed with a uniform element size of 1 mm with linear tetrahedral elements. Locally defined material properties were applied to model bone heterogeneity, as the mechanical properties of the bone tissues were assigned to each element based on the QCT scans (Figure 1a). Hydroxyapatite calibration phantoms (Hitachi Presto, Hitachi Medical Corporation, Tokyo, Japan) were used to determine the relationship between the Hounsfield Units (HU) and elastic moduli. The determined equations are provided in Table 1.

Table 1. The applied formulas between the HU values and elasticity moduli (63).

Formula	No. of equation
$\varrho_{QCT} = 5.2 \times 10 - 3 + 8 \times 10 - 4 \times HU$ [g/cm^3]	1
$\varrho_{QCT} = \varrho_{ash}$	2
$\varrho_{ash} = \varrho_{app} \times 0.6$	3
$\varrho_{app} = 8.667 \times 10^{-3} + 1.333 \times 10^{-3} \times HU$ [g/cm^3]	4
$E = 4{,}730 \times \varrho_{app}^{1.56}$ [g/cm^3]	5

The HU values were converted to equivalent BMD (ρ_{QCT}) by using calibration phantoms (equation no. 1) with known densities of 50, 100, 150, and 200 mg/cm^3 (95). Equivalent BMD was equal to ash density (ρ_{ash}) (equation no. 2) (14,96,97), while the apparent density (ρ_{app}) was calculated as 60% of ash density (equation no. 3) (14,98). The relationship between apparent density and HU (equation no. 4) was calculated employing the equations no. 1, 2 and 3. The isotropic elastic modulus (E) was calculated from apparent density based on a relationship from the literature (99).

For the assignment of the calculated elastic moduli to the elements, the volume meshes were imported into Materialise Mimics software. Elements were categorised into ten equal-sized groups based on their average HU value (100). Elements with negative HU values were placed in an eleventh group, representing fat- and marrow-like materials with lower density (101). The median HU value of each group served as the representative value and was assigned to all elements within the group. The Poisson's ratio of all bony tissues was uniformly set at 0.3 (96–98).

Soft tissues, such as the facet joints were modelled as a 0.25 mm thick cartilage layer with an initial gap of 0.5 mm between adjacent surfaces (102) and then meshed with 6-node wedge elements (103). The intervertebral discs (IVD) consisted of the nucleus pulposus (NP) and the annulus fibrosus (AF), including both the ground substance (GS), the fibres, and the 0.5 mm thick cartilaginous endplates (CEP). The AF GS was constructed as six concentric layers (104) around the NP, which accounted for 45% of the IVD (105) and was shifted posteriorly in accordance with the literature and general anatomy (106). The AF GS and the NP were represented with 8-node hybrid hexahedral elements (104), while CEP was meshed with linear tetrahedral and pyramid elements. The fibres were modelled with tension-only truss elements in a criss-cross pattern with an alternating angle of ±30°

to the axial plane of the IVD (107). The cross-sectional area values of the fibres in each layer were calculated from the volume ratio of the fibres to the GS: 23% (outermost), 20%, 17%, 13%, 9%, and 5% (innermost), respectively (108) (Figure 1b).

All seven major spinal ligaments were modelled: anterior longitudinal ligament, posterior longitudinal ligament, ligamentum flavum, interspinous ligament, supraspinous ligament, intertransverse ligament, and capsular ligament (Figure 1c).

Table 2. Material properties and element types of the lumbar spine FE model.

Material	Element type	Material properties	Reference
Bone	C3D4	Relationship between HU and E from equations (1)–(5); ν = 0.3	(96–98)
CEP	C3D4, C3D5	E = 23.8, ν = 0.42	(109)
Facet Cartilage*	C3D6	C10 = 5.36; D1 = 0.04	(109)
NP †	C3D8H	C10 = 0.12; C01 = 0.03	(110)
AF GS †	C3D8H	C10 = 0.18; C01 = 0.045	(111)
AF fibres	T3D2	Nonlinear stress-strain curve; cross-section area values calculated at each layer from AF volume.	(111–113)
Ligaments	SPRINGA	Nonlinear stress-strain curve	(114)

C10, C01, D1: Material constants; E: Young's modulus (in MPa), ν: Poisson's ratio

* = Neo-Hooke hyperelastic model, † = Mooney-Rivlin hyperelastic model

CEPs were assigned with linear elastic material properties obtained from the literature (109). The NP and AF GS were modelled with a 2-parameter hyperelastic Mooney-Rivlin formulation to represent their incompressible behaviour. The mechanical behaviour of the annulus' collagenous fibres followed a nonlinear stress-strain curve from Shirazi-Adl (113). Given the stiffer nature of the outer layers compared to the inner layers of the IVD, collagen fibres were weighted by scalar factors defined for each layer (111). Facet cartilage was modelled with a hyperelastic Neo-Hooke formulation (109). Tension-only, nonlinear uniaxial spring elements (115) were employed to simulate ligament behaviour. The material properties used for the lumbar spine FE model are presented in Table 2.

3.1.2. Loading and boundary conditions for the finite element analysis of the healthy lumbar spine

Three loading cases were employed to validate the lumbar spine FE model accurately. First, a pure bending moment of 7.5 Nm was applied in the three anatomical planes at the superior endplate of L1 to simulate flexion, extension, lateral bending, and axial rotation (Supplementary Figure 1) (116). Second, a compressive follower load of 1000 N was employed to measure the IDP without bending moments (117). Third, a combination of a follower load and a bending moment was used with magnitudes adopted from Dreischarf et al. for flexion, extension, lateral bending, and axial rotation.: 1175 N with 7.5 Nm, 500 N with 7.5 Nm, 700 N with 7.8 Nm, and 720 N with 5.5 Nm, respectively (7). During the simulations, the most caudal endplate of L5 was fixed in all degrees of freedom (Supplementary Figure 1). The contact behaviour between the facet joint surfaces was assumed to be frictionless (118).

The outcomes were compared with in vivo (119–122) and in vitro experimental measurements taken from the literature (123–126). In the case of pure bending, the ROM, the intervertebral rotations (IVR), and the facet joint forces (FJF) were compared with in vitro (123,124,126) and in silico data (7,103). In addition, the load-deflection curves of L1–L5 were plotted with an in vitro measurement, and a range from numerical results. In the case of pure follower load, the intradiscal pressure (IDP) in the L4–L5 NP was averaged over all elements and then compared with in vitro (125) and in silico results (7). A combined compressive and bending load was applied to the FE models to measure the IVR, FJF, and IDP values at each spinal level and compared with in silico (7) and in vivo measurements (119–122), as the combined loads are assumed to be the most representative for in vivo experiments (127).

To ensure that the mesh resolution did not affect the accuracy of model predictions, all elements of the bony parts of the L4 vertebra were investigated with five different element sizes (0.607, 1, 1.65, 2.73, and 4.505 mm) (14). The edge length of the most refined mesh was determined based on the resolution of the CT. The mesh was considered convergent when the difference in the von Mises stress values was less than 10% compared to the most refined mesh (14,118). As the results are most sensitive to axial rotation, a 7.5 Nm was applied on the upper vertebral endplate, while the lower endplate was fixed at all degrees of freedom (118,128).

3.1.3. Development of the healthy thoracolumbar spine finite element model

The nonlinear FE model of the thoracolumbar (T7-L5) spine was developed based on the previously presented QCT scans of a healthy 24-year-old male (Figure 2a). A threshold-based segmentation process was employed to obtain the 3D geometric representation of the lumbar (L1-L5) and the thoracolumbar (T7-L1) spine segments in the Mimics software. Subsequently, the triangulated surface meshes were imported into 3-Matic software in STL format. Both the lumbar and thoracolumbar regions included the first lumbar vertebra, which served as a basis for the n-point rigid surface registration, creating the T7-L5 spine model in a common reference system (Figure 2b). The quality of the registration and alignment was checked by calculating the Hausdorff Distance (HD) with MeshLab software (Metro Tool, Visual Computing Lab, Pisa, Italy) (Figure 2c) (129).

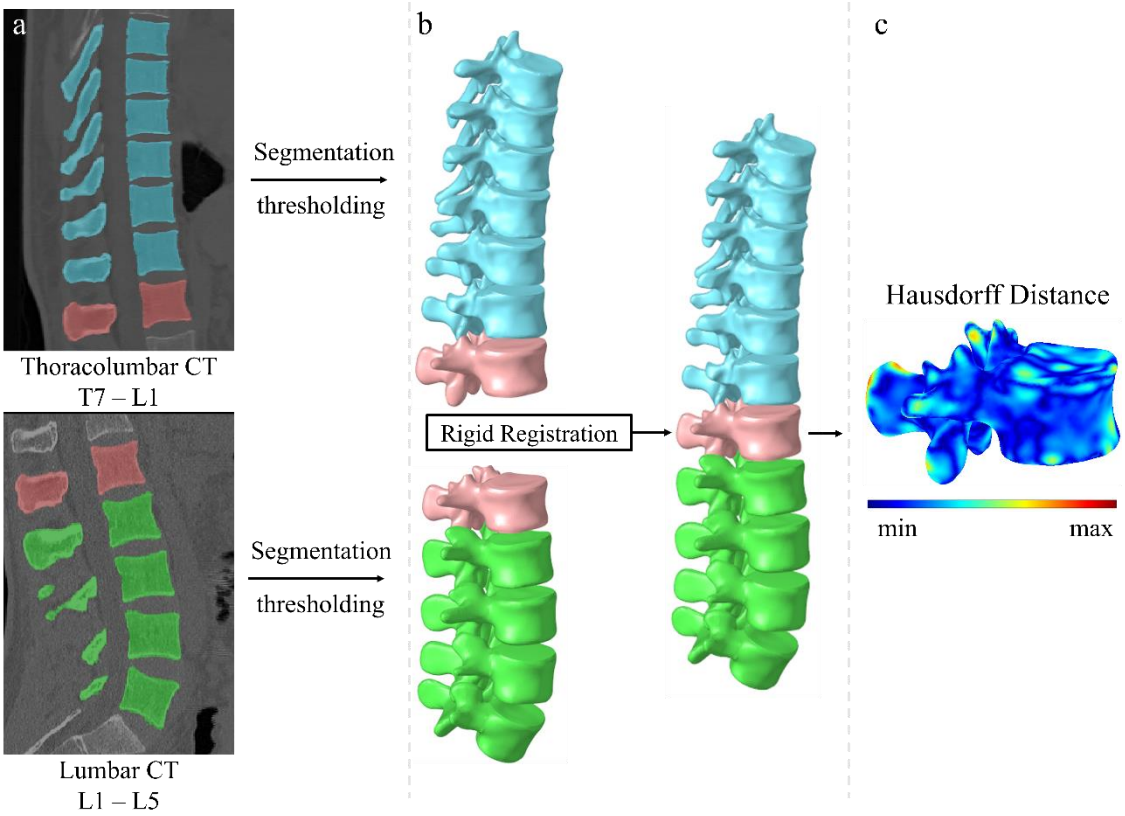

Figure 2. Overview of the modelling process. a) The segmentation of the lumbar and thoracolumbar regions. b) Rigid surface registration of the generated 3D lumbar and thoracolumbar models and the aligned T7-L5 geometry model. c) Visualisation of the HD between the two L1 geometries. Figure from Turbucz M and Fayad J et al. 2023 (91).

The aligned T7-L5 spine model was then imported into HyperWorks software, where the finalised FE model was constructed. The vertebrae were divided into the 1 mm thin cortical shell, the cancellous core, the 0.5 mm thin vertebral endplates, and the posterior elements (130,131). The bony components of the vertebral bodies were meshed with 1 mm linear tetrahedral elements. Linear elastic material properties were used for the cortical and cancellous bone, the vertebral endplate and the posterior elements (109,113,132).

Table 3. Summary of the applied material properties and element types used in the thoracolumbar FE model.

Material	Element type	Material properties	Reference
Cortical bone	C3D4	E=10,000; ν=0.3	(132)
Trabecular bone	C3D4	E=100; ν=0.2	(113)
Posterior elements	C3D4	E=3,500; ν=0.25	(113)
Vertebral endplate	C3D4	E=1,200; ν=0.29	(133)
CEP	C3D6, C3D8	E=23.8; ν=0.42	(109)
NP †	C3D8H	C10 = 0.12; C01 = 0.03	(110)
Facet Cartilage*	C3D6	C10 = 5.36; D1 = 0.04	(109)
AF GS †	C3D8H	Lumbar: C10=0.18; C01=0.045 Thoracic: calibrated stress-strain relationship.	(110,111)
AF fibres	T3D2	Lumbar: Nonlinear stress-strain curve; cross-section area values calculated at each layer from AF volume. Thoracic: calibrated stress-strain relationship.	(111–113)
Ligaments	SPRINGA	Nonlinear stress-strain curve	(114)

C10, C01, D1: Material constants; E: Young's modulus (in MPa), ν: Poisson's ratio

* = Neo-Hooke hyperelastic model, † = Mooney-Rivlin hyperelastic model

The soft tissues of the thoracolumbar FE model, specifically the IVD, facet joints, CEP, NP, AF GS, AF fibres, and spinal ligaments, have been modelled identically, as explained in 3.1.1. section. Therefore, the modelling of these spinal soft tissues is not repeated in this section. Nonetheless, the material properties of the thoracolumbar FE model are summarised in Table 3.

The material properties of the soft tissues in the thoracic region were derived from those in the lumbar region. However, to approximate the in vitro measured IVR values in the T7-L1 region, specific adjustments were made to the material properties of the IVDs. Two scalar calibration parameters were introduced for this purpose. λ_{GS} was employed to calibrate the material of the annulus GS, with values ranging from 0.0025 to 238, representing the physiological limits of the GS material. Additionally, λ_{FIBER} served as a weighting factor for the stress-strain relationship of the fibres and could vary between 0.3 and 2, as established by Schmidt et al. (111).

3.1.4. Loading and boundary conditions for the finite element analysis of the healthy thoracolumbar spine

To validate the T7-L5 intact spine model, pure bending moments were applied in the three anatomical planes to mimic flexion-extension, lateral bending, and axial rotation. Multiple FE models were created and loaded at the most cranial endplate, while the most caudal endplates were fixed in all degrees of freedom in each validation FE model (116). The calculated IVR values of the FE models were compared with the available in vitro data from the literature (123,134,135).

3.1.5. Development of the healthy pelvis finite element models

The geometric model of the intact pelvis was created using the anonymized QCT images from a 24-year-old male. The geometry was defined based on the QCT scans with segmentation (Figure 3a-b). Depending on the bone modelling strategy, two different FE models were developed in the HyperWorks FE pre-processor software. In the PSM, the sacrum and iliac bones were uniformly meshed using 1 mm linear tetrahedral elements to ensure that the elements were not larger than the slice thickness of the QCT scan. Subsequently, the equations listed in Table 1 were utilized to establish the relationship between HU values and elasticity moduli, following the method described in 3.1.1. section. Using Materialise Mimics, the bony elements were categorized into ten material

bins based on their average HU values (100). Elements with negative HU values were placed in an additional group, representing fat- and marrow-like materials (Figure 3c) (101).

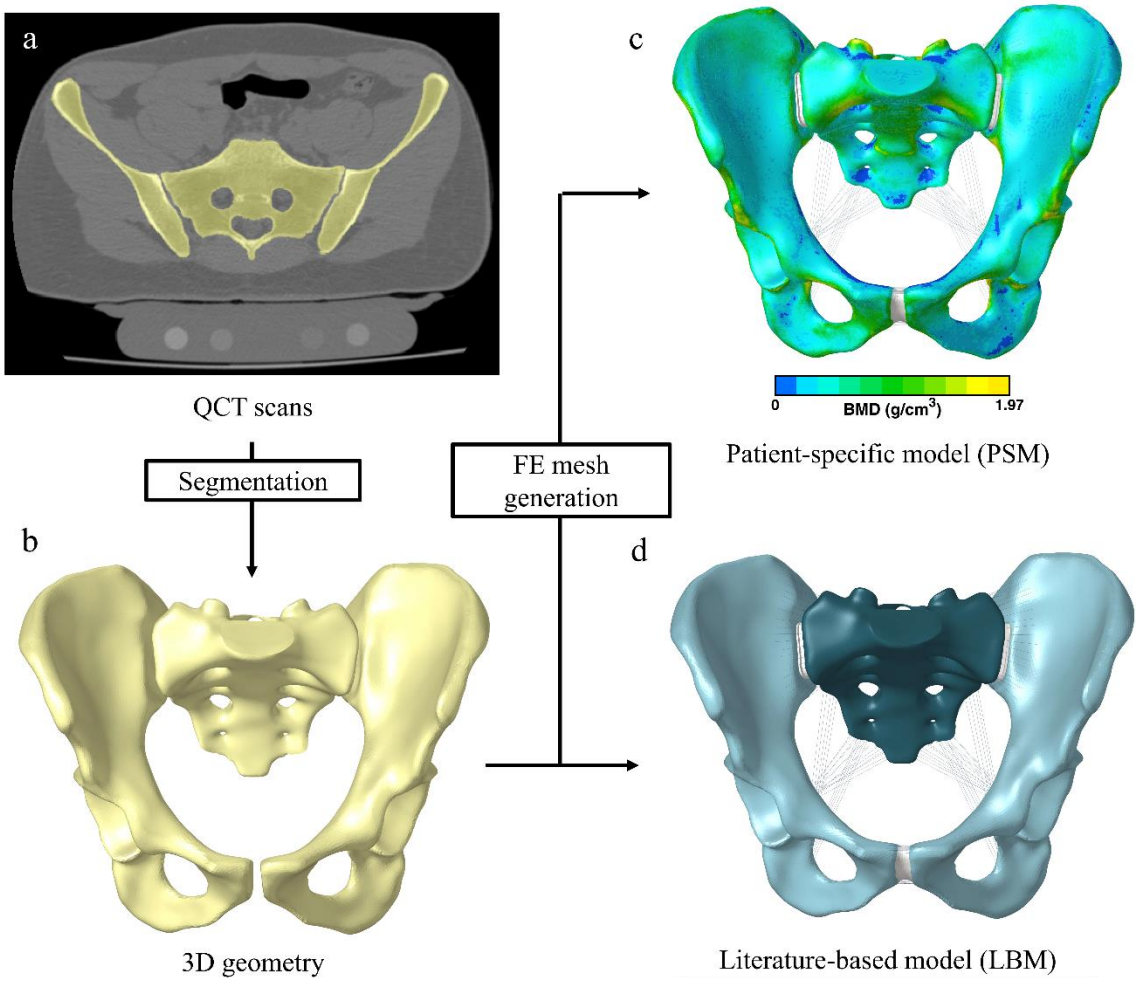

Figure 3. Construction of the two pelvis FE models. (a) QCT scans with the calibration phantoms. (b) 3D geometry was reconstructed with QCT scan-based segmentation. (c) Osseoligamentous FE model of the PSM with bone material properties assigned based on the QCT scans. (d) Osseoligamentous FE model of the LBM with bone material properties taken from the literature. Figure from Turbucz M et al. 2023 (136).

In the literature-based model (LBM), the sacrum included a trabecular core, an S1 bony endplate and a cortical layer, both 0.45 mm thick (137). The iliac bones were modelled with a 1 mm thick cortical shell and a trabecular core (137). All bony components were adaptively meshed with linear tetrahedral elements, ranging from a minimum of 1 mm to a maximum of 4 mm edge length, and assigned isotropic homogeneous linearly elastic

bone material properties obtained from the literature (Figure 3d) (56,133). The detailed material properties of the bony components can be found in Table 4.

Table 4. Applied material properties, including bone- and soft tissues and the implant.

Model	Material	Material properties	Reference
LBM	Cortical bone	E = 18,000, ν = 0.3	(56)
	Trabecular bone	E = 150 , ν = 0.2	(56)
	Bony endplate	E = 1,200, ν = 0.29	(133)
PSM	Bone	Relationship between the HU and the Young's moduli based on the QCT scans	(14,96–99)
LBM & PSM	Sacroiliac cartilage	E = 1,000, ν = 0.3	(56)
	Interpubic disc	E = 5 , ν = 0.3	(56)

E: Young's modulus (in MPa), ν: Poisson's ratio

The SIJ was developed as a true diarthrosis with an initial gap of 0.3 mm between the adjacent articular surfaces. Regions of the cartilages were defined based on the QCT scans and were modelled with a uniform sacral and iliac cartilage thickness of 2 mm and 1 mm, respectively (138). The SIJ was meshed with linear tetrahedral elements, while its material properties were assigned according to a previous in silico study (56). The interpubic disc was modelled as an interspace structure and meshed with tetrahedral elements (139).

Eight pelvic ligaments were included in the FE models: the superior pubic ligament, the arcuate pubic ligament, the anterior sacroiliac ligament, the interosseous sacroiliac ligament, the long posterior sacroiliac ligament, the short posterior sacroiliac ligament, the sacrospinous ligament and the sacrotuberous ligament. The attachment regions were selected based on available anatomic data in the literature (140). Ligaments were modelled as tension-only uniaxial spring elements with material properties obtained from the literature (56,141) and summarized in Supplementary Table 1.

3.1.6. Loading and boundary conditions for the finite element analysis of the healthy pelvis

To validate the LBM and PSM pelvis FE models, the displacement values of the sacrum under different loading conditions were measured and compared to the findings of a cadaveric study by Miller et al. and several in silico studies (137,142–144). Since the motion of the sacrum is primarily influenced by the soft tissues rather than the bone, the bony structures were modelled as rigid bodies for validation purposes (145). The virtual simulation closely replicated the original cadaveric experiment. Five translational loads (superior, inferior, anterior, posterior and mediolateral) and four rotational loads (flexion, extension, lateral bending and axial rotation) were applied to the sacrum, while both ilia were fixed. The displacement of a reference point representing the centre of the sacrum was recorded. A tight connection was set between the bony and soft tissues, and frictionless finite sliding was defined between the adjacent SIJ surfaces (56).

3.1.7. Development of the healthy lumbopelvic finite element models

The healthy lumbopelvic FE model was created by combining the FE models of the intact lumbar spine and pelvis, which were previously developed, verified, validated, and published (63,91,136). In addition, these FE models of the lumbar spine and the pelvis were presented in the previous sections of this PhD thesis. Therefore, the intact lumbopelvic FE model development is only concisely presented in the following sections. The lumbar part of the thoracolumbar FE model (presented in the 3.1.3. Development of the healthy thoracolumbar spine finite element model section) and the LBM pelvis FE model (presented in the 3.1.5. Development of the healthy pelvis finite element models section) were combined to develop the lumbopelvic FE model. Since these models were previously validated, the intact lumbopelvic FE model was considered suitable for further biomechanical analysis. However, the surgical lumbopelvic FE models were validated to increase the reliability of the FE predictions.

3.2. Part II. In silico investigation of different spinal fixation techniques in the thoracolumbar spinal region

3.2.1. Development of the surgical finite element models of spinal fixation techniques in the thoracolumbar spine

To investigate the biomechanical effect of different spinal fixation techniques on the onset of PJK, in addition to the healthy thoracolumbar spine (Figure 4a), the FE models of one rigid and two types of SFTs were developed:

1) TRF – model: posterior fusion of the spine from T8 to L5 using bilateral pedicle screws and Ø5.5 mm titanium rods (Figure 4c); 2) PRF – model: Ø5.5 mm PEEK rods between T8 and T9 combined with posterior stabilisation of the spine from T9 to L5 using bilateral pedicle screws and Ø5.5 mm titanium rods. A rod connector device was placed to connect the titanium and PEEK rods (Figure 4b); 3) MRF – model: five Ø1.9 mm titanium rods between T8 and T9 combined with a posterior fusion of the spine from T9 to L5 using bilateral pedicle screws and Ø5.5 mm titanium rods. A rod connector device was placed to connect the titanium and the multiple titanium rods (Figure 4d). The material properties and the element types of the titanium and PEEK material are summarized in Table 5.

Table 5. The material properties and the element types of the titanium and PEEK material

Material	Element type	Material properties	Reference
Titanium	C3D4	E=110,000; ν=0.3	(133)
PEEK	C3D4	E=3,600; ν=0.3	(133)

E: Young's modulus (in MPa), ν: Poisson's ratio

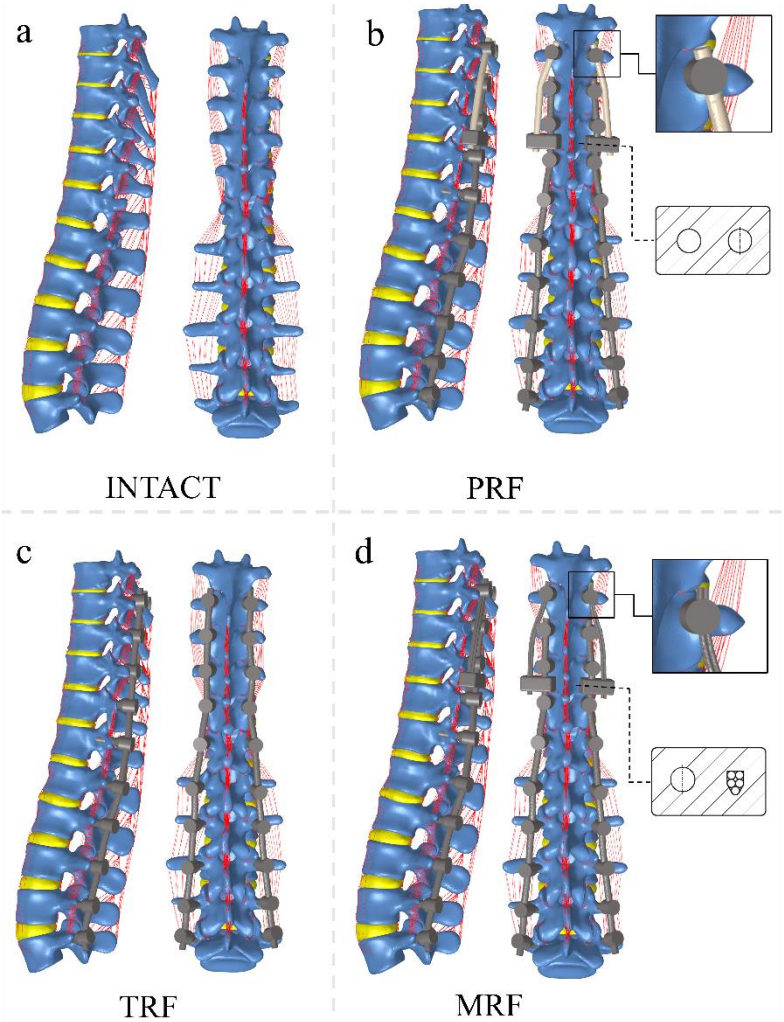

Figure 4. The analysed spinal fixation techniques in lateral and posterior views. a) The intact T7-L5 model, b) the PRF model, c) the TRF model, and d) the MRF model. Figure from Turbucz M and Fayad J et al. 2023 (91).

3.2.2. Loading and boundary conditions for the finite element analysis of different spinal fixation techniques

For all FE models, the loading was applied at the superior endplate of T7, while the inferior endplate of L5 was fixed in all degrees of freedom. For a proper biomechanical evaluation of adjacent segment effects, a modified multidirectional hybrid test protocol has been applied in this PhD thesis, consisting of two subsequential loading steps (146).

1. Load-controlled step: The intact T7-L5 and the instrumented FE models were loaded with 5 Nm pure bending moment in the anatomical planes to simulate flexion-extension, lateral bending, and axial rotation (35). IVR values of the intact spine and the spinal fixation techniques were measured. Then, the IVR of the intact spine were

used to normalise the results of the three instrumented FE models. For symmetrical load cases, such as lateral bending and axial rotation, the right and left sides' values were averaged.

2. Displacement-controlled step: For a physiologically realistic comparison, the displacement of the TRF technique obtained from the first loading step was used as an input for the second loading step. The maximum von Mises stress values in the pedicle screws and the stress distribution at the UIV level were analysed. The maximum stress values for lateral bending and axial rotation were averaged similarly to the first step.

3.3. Part III. In silico investigation of different sacral fracture fixation techniques using two sets of bone material properties

3.3.1. Development of the surgical finite element models of different iliosacral screw fixations in the case of sacral fractures

An AO Type B2 unilateral transforaminal sacral fracture was developed by cutting the healthy sacrum into two parts, with ligamentous tissues left intact in both the LBM and PSM (55,56). The fixations were developed by placing ISS and TISS in the fractured models (55,56). Screws with a diameter of 7.3 mm were inserted as described in the literature for fixing unilateral transforaminal sacral fractures (147). Thus, screws were perpendicular to the fracture plane with screw tips ending either near the counter lateral SIJ in the sacrum (ISS) or bridging both SIJ (TISS) (147).

Six types of fixations were constructed as follows: (1) ISS at S1 (ISS1, Figure 5a), (2) ISS at S2 (ISS2, Figure 5b), (3) ISS at S1 and S2 (ISS12, Figure 5c), (4) TISS at S1 (TISS1, Figure 5d), (5) TISS at S2 (TISS2, Figure 5e), and (6) TISS at S1 and S2 (TISS12, Figure 5f). Material properties of the ISS and TISS are detailed in Table 6.

Table 6. Applied material properties of the ISS and TISS.

Model	Material	Material properties	Reference
LBM & PSM	Screw	E = 114,000, ν = 0.3	(56)

E: Young's modulus (in MPa), ν: Poisson's ratio

An ideal connection was set between the bone and the screw bodies, while a penalty contact interaction with a friction coefficient of 0.3 was defined between the interfragmentary surfaces (56). Balanced standing on both feet was simulated with a vertical load of 600 N applied on the cranial endplate of the sacrum while both acetabula were fixed (147).

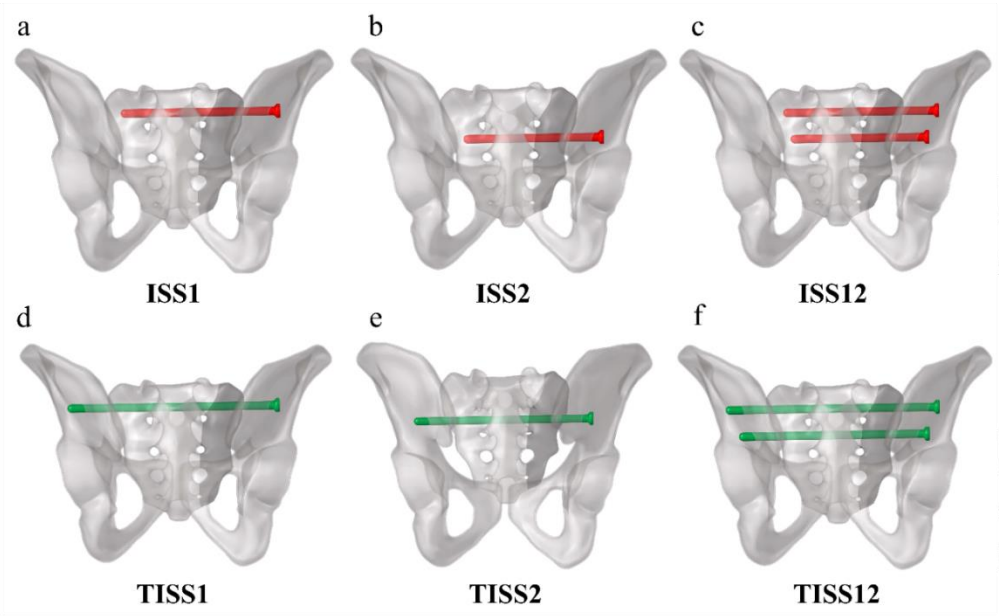

Figure 5. Fixation configurations investigated in this PhD thesis: a) ISS at S1 (ISS1), b) ISS at S2 (ISS2), c) ISS at S1 and S2 (ISS12), d) TISS at S1 (TISS1), e) TISS at S2 (TISS2), and f) TISS at S1 and S2 (TISS12). Figure from Turbucz M et al. 2023 (136).

3.3.2. Loading and boundary conditions for the finite element analysis of different iliosacral screw fixations in the case of sacral fractures

The vertical stiffness (VS) was determined by dividing the load by the vertical displacement of the sacrum (48,57). Then, these VS values were normalised to the corresponding intact sacrum for all fixation techniques in both the LBM and PSM. To evaluate the probability of implant failure, the maximum von Mises stress values in the screws were investigated (55,57,59,61). The relative interfragmentary displacement (RID) on the fracture interface was analysed to evaluate the fracture healing progress (43,48,57). RID distribution and the maximum RID values for both models were reported. In addition, the stress state of the fracture interface was investigated. Conventionally, fracture healing is characterised by examining the maximum stress values on the sacral fracture interface (55,57,59,61). However, due to the heterogeneity of locally defined

bone material properties in the PSM, relying solely on the maximum values can be misleading. Therefore, instead of focusing on the maximum stress values, nodes from both models falling within the top 1% of stress values were analysed to ensure more accurate results. A boxplot figure was created to illustrate the median, minimum, and maximum stress values (63).

Data management was performed using Microsoft Excel (Microsoft Corporation, Redmond, WA, USA), data processing was performed in the Python (Python Software Foundation, Wilmington, DE, USA) environment, and statistical analysis was conducted using IBM SPSS Statistics 25.0 (IBM Corp., Armonk, NY, USA).

The VS, the maximum von Mises stress, and the maximum RID values were compared among the six groups using a Wilcoxon signed-rank pair test ($p \leq 0.05$). Additionally, the distribution of the stress values falling within the top 1% of nodal stress was analysed using the two-sample Kolmogorov-Smirnov test ($p \leq 0.05$), both on the fracture and the bone-implant surface.

3.4. Part IV. In silico investigation of different lumbopelvic reconstruction techniques after total sacrectomy

3.4.1. Development of the lumbopelvic finite element models after total sacrectomy

To model total sacrectomy without LPDR, the sacrum was simply removed from the intact segmentation-based geometry model (Figure 6 a-b) without any further anatomical modification (Figure 6c). Subsequently, the sacrectomy FE model without LPDR was created (Figure 6d). To model total sacrectomy with LPDR, the anatomy after total sacrectomy was further modified by pulling down the lumbar spine by 1.1 cm. Furthermore, the iliac bones were moved inwards by 1.3 cm on the right side and by 1.5 cm on the left side towards the lumbar spine to achieve a distance reduction of ca. 1.7 cm on both iliac sides (Figure 6e). Finally, the sacrectomy FE model with LPDR was created, similar to that without LPDR (Figure 6f).

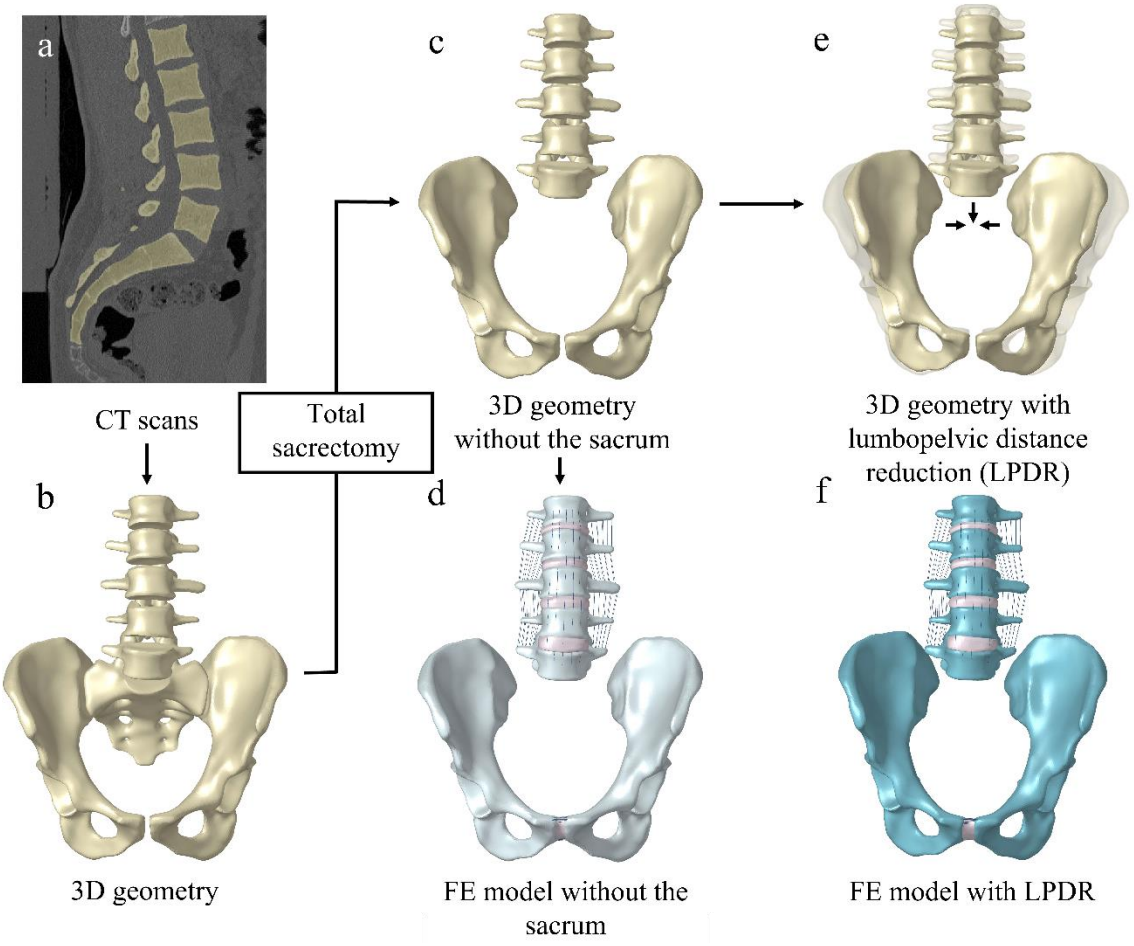

Figure 6. a) CT scans of the lumbopelvic region. b) Segmentation-based surface model of the intact lumbopelvic region. c) Surface model after the total sacrectomy without LPDR. d) Total sacrectomy FE model without LPDR. e) Surface model after the total sacrectomy with LPDR. f) Total sacrectomy FE model without LPDR. Figure from Turbucz M et al. 2024 (148).

3.4.2. Development of the surgical finite element models of lumbopelvic reconstruction techniques after total sacrectomy

Using the FE models with and without LPDR, four different LPRTs were analysed: the CLR, the SRR, the FRR, and the ICR techniques (Figure 7).

The CLR technique featured posterior stabilisation through pedicle screws between the L3 and L5 pedicles. Into the bilateral posterior inferior iliac bones, two iliac screws were inserted, the short and the long iliac screw. The pedicle and iliac screws were interconnected via a single U-shaped rod, with no additional anterior stabilisation (Figure 7a). In the FE model with LPDR, the U-shaped rod is shorter as the distance between the

screw heads decreases. Accordingly, the curvature of the rod is increased between the lumbar spine and the ileum (Figure 7e).

The posterior segment of the SRR technique included the same pedicle screws as the CLR technique, between the L3 and L5 pedicles, connected to the long iliac screws through two longitudinal rods. In the anterior part of the SRR, a horizontal sacral rod bridged the iliac bones and was attached to the inferior endplate of L5 using two screws (Figure 7b). In the case of LPDR, the sacral rod was slightly moved to align with the repositioned ileum (Figure 7f).

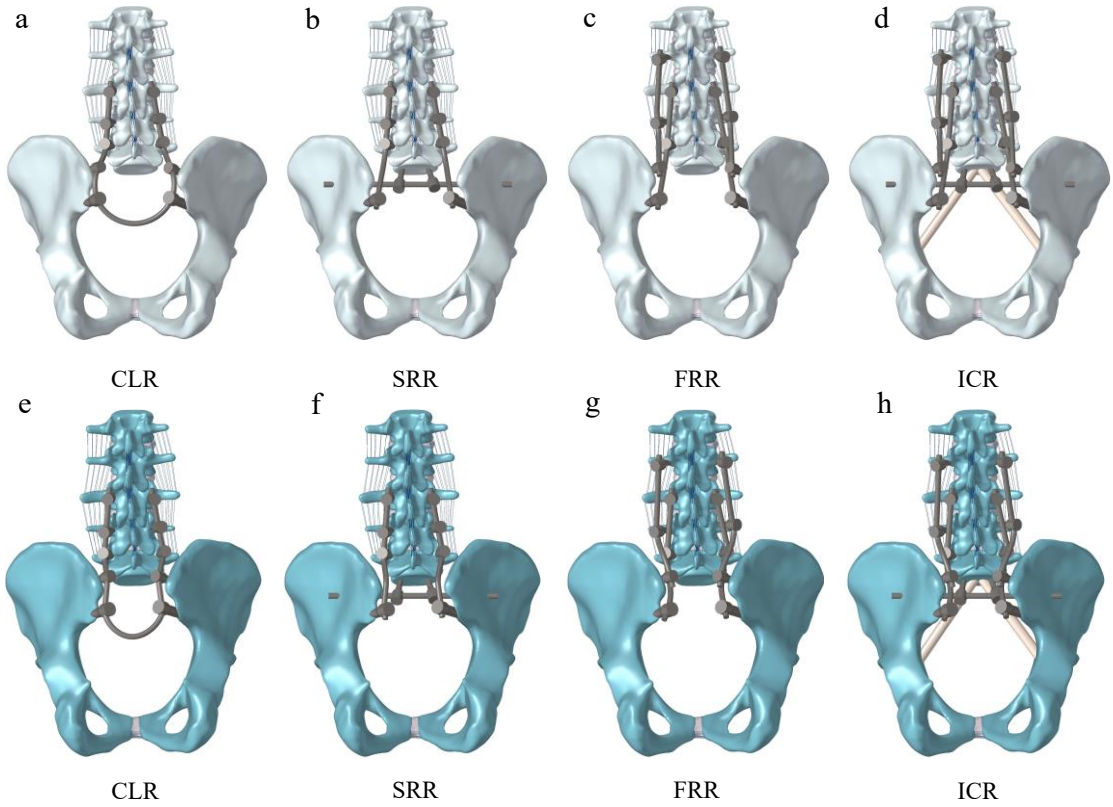

Figure 7. a) FE models of the CLR, b) the SRR, c) the FRR, d) and the ICR techniques without LPDR. e) FE models of the CLR, f) the SRR, g) the FRR, h) and the ICR techniques with LPDR. Figure from Turbucz M et al. 2024 (148).

The FRR technique included only posterior stabilisation. Pedicle screws were inserted between the L2 and L5 pedicles using the Roy-Camille screw placement at the medial side and the Magerl screw placement at the lateral side (74). Four longitudinal rods were utilised in this technique, with the lateral screws connected to the short iliac screws and the medial screws to the long iliac screw (Figure 7c). Following LPDR, the curvature of

the rods increased as the iliac screws were positioned closer to the midline of the spine (Figure 7g).

The ICR technique consisted of the posterior part of the FRR and the anterior stabilisation of the SRR technique. Additionally, two fibular flaps were positioned along the iliopectineal lines between the lumbar spine and the pelvis (Figure 7d). In the ICR after LPDR, the fibular grafts were repositioned to align with the modified iliopectineal line (Figure 7h). The LPRTs analysed in this current FE analysis are detailed in previous studies (67,78,82,83).

In all LPRTs, the diameters were as follows: 6 mm for the pedicle screws, 8 mm for the short iliac screws, 10 mm for the long iliac screws, 6 mm for the horizontal sacral rod, and 5.5 mm for the spinal rods (74,91). An ideal connection was modelled through shared nodes at the bone-screw and the screw-rod connections (91). Screws and rods were meshed with linear tetrahedron elements and were assigned with titanium material properties, as detailed in Table 5. The material properties of the lumbar spine (lumbar part of the thoracolumbar FE model) and the pelvis are detailed in Table 3 and Table 4, respectively.

3.4.3. Loading and boundary conditions for the finite element analysis of the lumbopelvic reconstruction techniques

The FE models of the intact lumbar spine and the pelvis were verified, validated, and published in previous publications (63,136). In addition, the pedicle screws and spinal rods were involved in a previous FE analysis with identical dimensions and mesh resolution (91). Therefore, no repeated mesh verification and intact model validation were carried out. However, validation of the surgical models is essential to ensure the reliability of the FE results and to draw adequate conclusions (149). The SRR, FRR, and ICR techniques were previously examined in a cadaveric in vitro study by Cheng et al. (83). Thus, validation was conducted for these three LPRTs using identical loading and boundary conditions.

The L1 and connected soft tissues were removed for validation. A vertical force of 500 N was applied at the superior endplate of L2, shifted anteriorly to the hip joint's centre of rotation, resulting in a moment of ca. 14 Nm (74). To simulate the hip function, the ileum could rotate in the sagittal plane with the two centre points of the hip joint being constrained (86). In addition, the pubis ramus was fixed in all degrees of freedom to

represent the metal hook used in the in vitro setup (86). Parameters for the validation were calculated as those in the cadaveric study. The shift-down displacement was defined as the vertical displacement of L5, and the relative sagittal rotation was calculated as the rotation of L5 in the sagittal plane relative to the ileum. To further increase the reliability of the FE models' predictions, results of a previous in silico study were also included in the validation (74). Since the in silico study by Zhu et al. did not include any anatomical modifications following total sacrectomy (74), the validation was performed using the sacrectomy FE models without LPDR.

Four loading cases were simulated to evaluate the LPRTs, employing combined follower load and bending moment (74). The follower load was applied along an optimised path through the lumbar vertebral bodies' centre of rotation (63,150), while the bending moment was applied at the superior endplate of L1 (7,63). For flexion, extension, lateral bending, and axial rotation, the follower load and bending moment pairs were 1175 N with 7.5 Nm, 500 N with 7.5 Nm, 700 N with 7.8 Nm, and 720 N with 5.5 Nm, respectively (7,74). For the evaluation of LPRTs, the lower part of the ileum was fixed in all degrees of freedom (74).

Lumbopelvic stability was assessed based on the shift-down displacement of L5 and the relative sagittal rotation of L5, both calculated using the same methodology as in the validation process (74,83). Additionally, the stress state at the bone-implant interface and within the rods was analysed to rank the reconstruction techniques regarding screw-loosening and implant safety.

Although the mesh resolution of the pedicle screws and rods had been verified previously (91), efforts were made to enhance the reliability of the predictions. Consequently, the mean von Mises stress, derived from the five nodes with the highest stress values, was employed instead of the maximum stress values measured in a single node (86). In the cases of symmetrical loading conditions, such as lateral bending and axial rotation, the averaged values, calculated from both right and left directions, were employed.

4. RESULTS

4.1. Part I. Results of the healthy finite element models validation

4.1.1. Results of the patient-specific lumbar spine finite element model validation

The mesh convergence test assessed von Mises stress percentage differences in the L4 vertebra between the finest and coarser mesh resolutions. Stress differences induced by the coarser mesh resolutions, in decreasing order of edge length, were 46.98%, 30.57%, 16.99%, and 2.73%. The 1 mm mesh demonstrated convergence, with a difference below 10%.

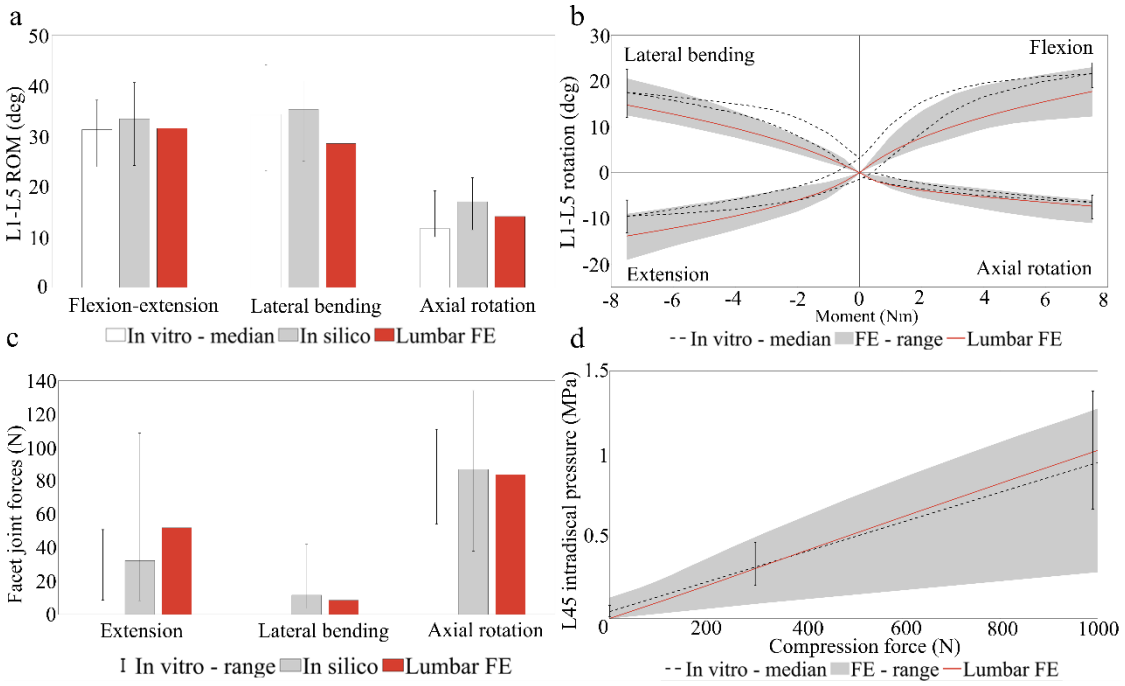

Figure 8. Results of the lumbar spine FE model (with red colour). a) L1-L5 ROM values in flexion-extension, lateral bending, and axial rotation against pure bending (7,123). b) Load-deflection curves (7,123) c) Mean FJF at all levels (7,124) d) IDP in the L4–L5 NP against compressive follower load (7,125).

Against pure bending moment load, the total L1–L5 ROM in flexion-extension, lateral bending, and axial rotation, the results were: 31.58°, 28.55° and 14.12°, respectively (Figure 8a). The nonlinear load-deflection curves illustrate the stiffening behaviour of the FE model against greater loads (Figure 8b). The mean FJF values were calculated as 51.94 N, 8.50 N, and 83.74 N in extension, lateral bending, and axial rotation, respectively (Figure 8c). IVR values occurred within the range of experimental measurements (126),

except at the L2–L3 and L4–L5 spinal levels in flexion, where the model slightly underestimated the in vitro measurement, although the results correlate well with the in silico data (Supplementary Figure 2a–d) (103).

Against pure compression load, the IDP value under the compressive follower load was 1.02 MPa The results were in good agreement with both the experimental results (125) and the in silico range (7) (Figure 8d).

Against combined load, the IVR results were consistent with the available literature data, although the results were outside the in vivo range in flexion at the L2–L3, L3–L4 and L4–D5 spinal levels (119–121). The in silico range (7) was not reached in flexion at L1–L2, in extension at L2–L3 and L4–L5, and in axial rotation at L1–L2, L2–L3 and L3–L4 (Supplementary Figure 2e-h). The IDP values showed good agreement with the published mean FE mid-values, while the simulation results approximated the available in vivo measurements (122) adequately (Supplementary Figure 3). The predicted FJF values were outside of the in silico range at L1–L2 and L2–L3 in axial rotation (7) (Supplementary Figure 4).

4.1.2. Results of the thoracolumbar spine finite element models calibration and validation

Weighting factor values for the annulus GS and fibres were between 0.28 and 0.5 and between 0.4 and 0.5, respectively. In more detail, the weighting factors obtained from the calibration process are given in the Appendix section in Supplementary Table 2. The IVR results of the thoracolumbar FE model were within the range of available in vitro measurements for all load cases, except at the T9-T10 spinal level for lateral bending (Supplementary Figure 6, Supplementary Figure 7, Supplementary Figure 8). In flexion-extension and axial rotation, the predicted values showed good agreement with the in vitro mid-values, while in lateral bending, the predictions of the FE model slightly underestimated the in vitro measurements.

4.1.3. Results of the sacrum finite element model validation

The comparison of the FE prediction to the results of Miller et al. showed excellent agreement (142). For each loading case, the results fell within the standard deviation and were close to the published median values of the experimental results (Figure 9). However, the FE model slightly underestimated the results of the cadaveric experiment in flexion and extension. In addition, good agreement was found with the result of

multiple in silico studies published in the literature (137,143,144). The detailed results of the model validation are represented in Figure 9.

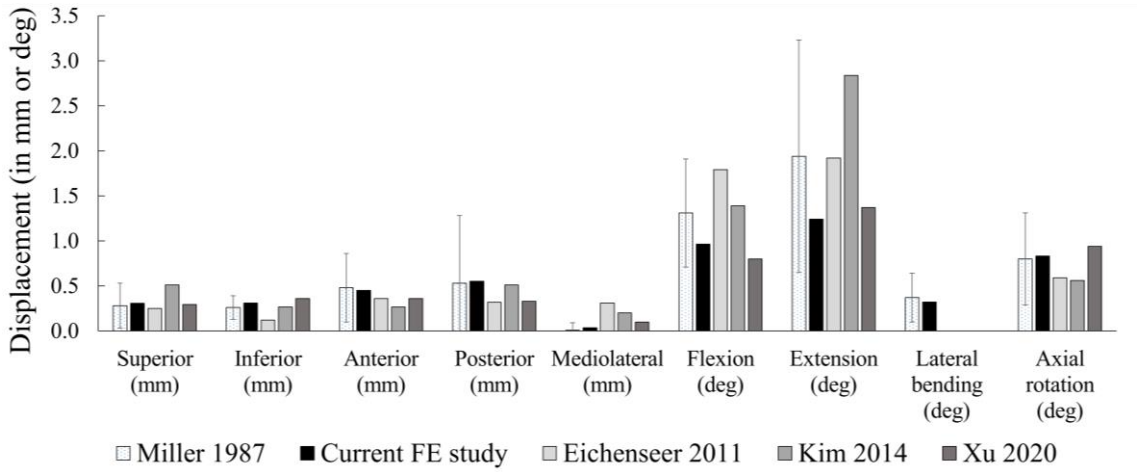

Figure 9. Results of the model validation with rigid body modelling of the bony regions. Sacral displacements and rotations were compared to the experimental results of Miller et al. and the in silico results of Eichenseer et al., Kim et al., and Xu et al. (137,142–144). Standard deviations are represented by error bars. Figure from Turbucz M et al. 2023 (136).

4.2. Part II. Results of the in silico investigation of different spinal fixation techniques in the thoracolumbar spinal region

4.2.1. Results of the of the alignment and registration

HD values were calculated to assess the quality of the alignment and registration. HD values were calculated between the segmented thoracolumbar-based L1 and the lumbar-based L1 vertebrae (Figure 2c). Minimum and maximum HD values were equal to 0 mm and 1.37 mm (mean= 0.15 mm, rms=0.2), respectively.

4.2.2. Results of the finite element analysis of different spinal fixation techniques

Load-controlled step: IVR values were measured against a pure bending moment of 5 Nm during this load step. The SFTs provided higher IVR values at the UIV level than the TRF (rigid) technique for all loading directions. At the UIV level, the IVR results normalised by the intact spine of the TRF, MRF and PRF models were 6.48%, 9.63%, and 12.90% for flexion (Figure 10a), and 7.0%, 10.02%, and 13.14% for extension (Figure 10b). For lateral bending, MRF and PRF gave 1.9 and 2.4 times higher IVR results than the TRF;

below the UIV level, all three fixation techniques gave values lower than 2.7% of the intact's IVR (Figure 10c). Among all the load cases, axial rotation gave the largest normalised IVR values with 8.76%, 44.77% and 60.51% for TRF, MRF and PRF, respectively (Figure 10d).

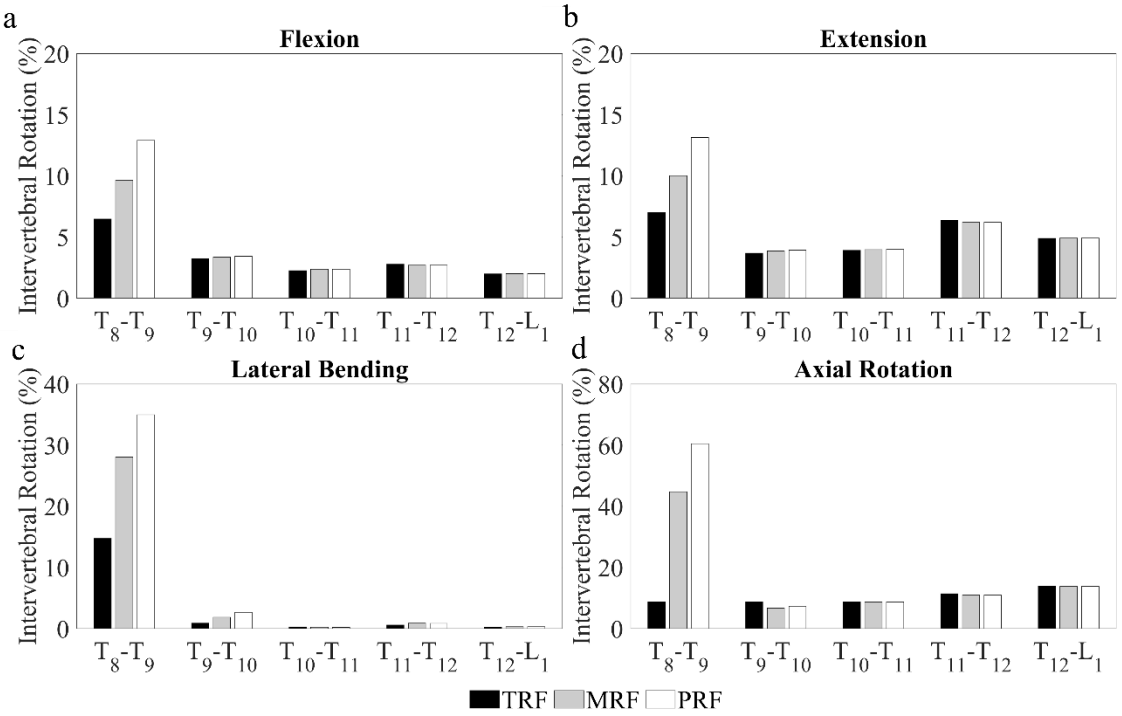

Figure 10. Calculated IVR angle values, normalised for the intact spine's results, against a pure bending moment of 5 Nm for a) flexion, b) extension, c) lateral bending, and d) axial rotation. Figure from Turbucz M and Fayad J et al. 2023 (91).

Displacement-controlled step: Maximum von Mises stress values of the screw bodies were analysed under identical displacements for all fixation techniques. In general, for all load directions, the TRF (rigid) model provided the largest, while PRF had the lowest peak stress values (Figure 11a-d). At the UIV level, TRF induced 37.26 MPa, 42.13 MPa, 44.4 MPa, and 44.59 MPa stress values in flexion, extension, lateral bending, and axial rotation, respectively. In comparison to the TRF, the application of the MRF and PRF technique reduced the maximum stress values by 17.28% and 27.72% for flexion, by 26.56% and 36.67% for extension, by 6.82% and 34.26% for lateral bending, and by 49.07% and 59.81% for axial rotation. In contrast to the other load cases, the maximum stress values below the UIV level were not reduced compared to the UIV level for axial rotation, as the results were 44.59 MPa, 45.99 MPa, 46.56 MPa, 53.26 MPa and 48.34 MPa, at T8, T9, T10, T11, and T12 respectively (Figure 11d).

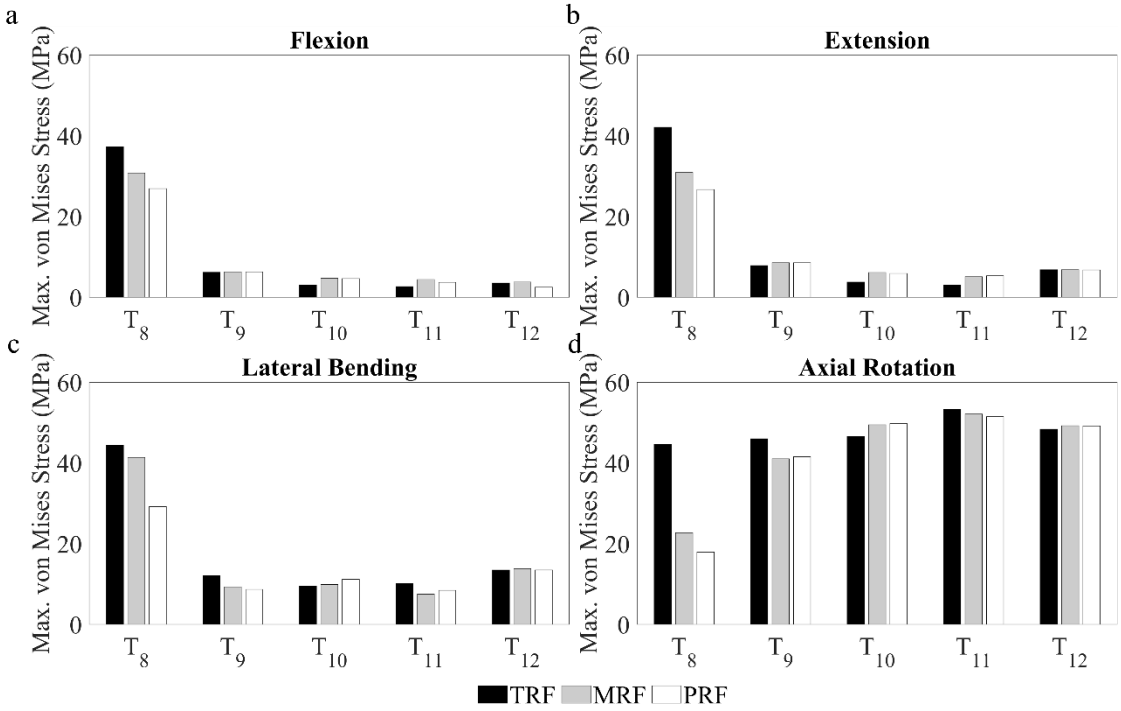

Figure 11. Maximum von Mises stress values in the pedicle screws against displacement-controlled load for a) flexion, b) extension, c) lateral bending, and d) axial rotation. Figure from Turbucz M and Fayad J et al. 2023 (91).

The distribution of the von Mises equivalent stress values at the UIV level (T8) was visualised and evaluated with an axial section of the pedicle screws. In general, the largest area with stress higher than 10 MPa was found in the TRF (rigid) model, while PRF (semirigid) included the least. The stress distributions in flexion and extension show a similar trend, i.e., the TRF technique results in much higher pedicle screw stress in both loading cases. In contrast, MRF gives less, while the PRF technique induces the least stress in both loading directions (Figure 12a-b). For right lateral bending, the stress distribution pattern of the MRF model shows similarity with the TRF model in the aspect of magnitude and expansion (Figure 12c). In contrast, for axial rotation, the peak stress values appeared at the outer edge of the screw bodies in the instrumented models, with the TRF model containing notably more area stress above 10 MPa than the MRF and PRF (Figure 12d).

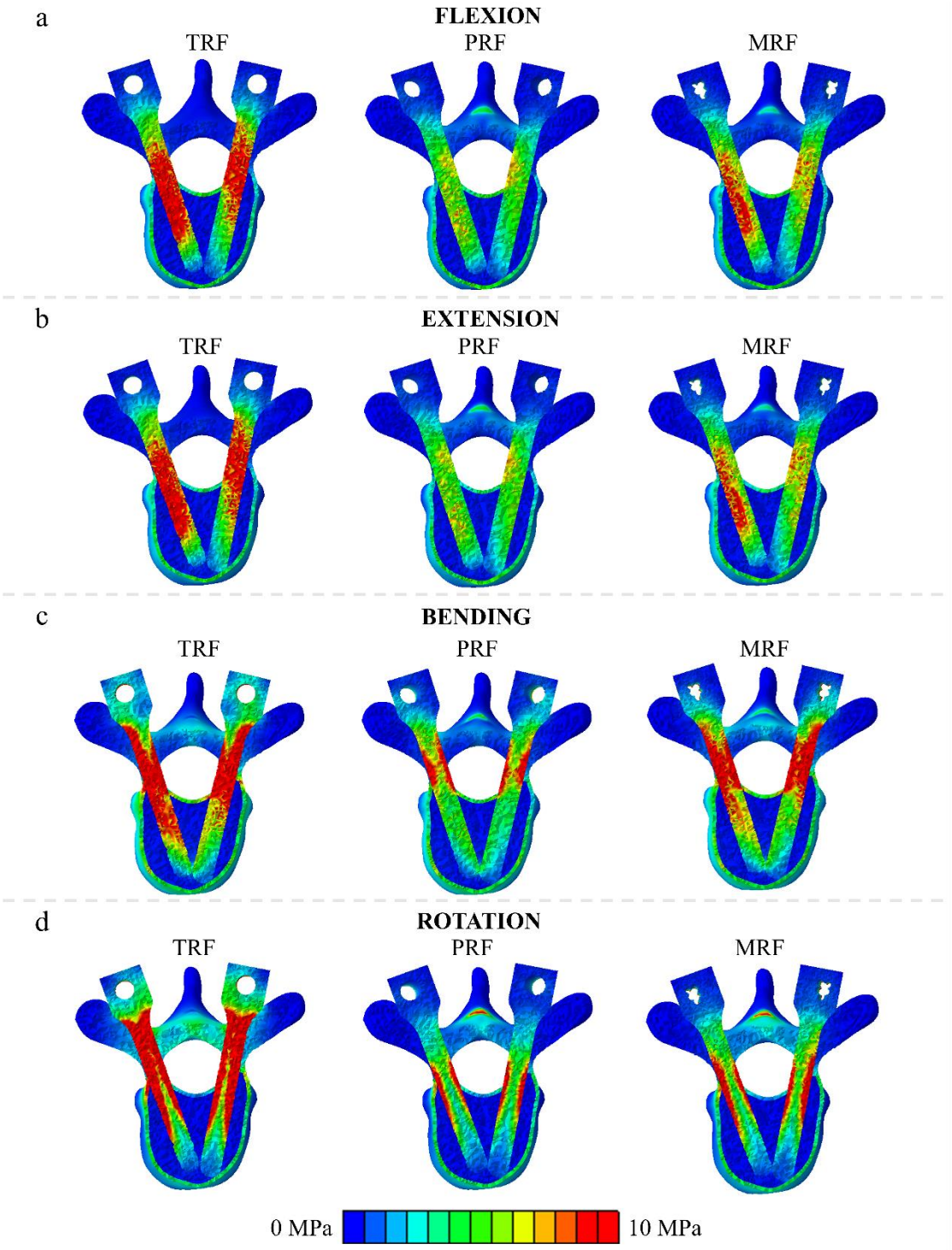

Figure 12. Von Mises stress distributions of the three fixation techniques at the UIV level for a) flexion, b) extension, c) right bending, and d) left rotation with the maximum scale value set to 10 MPa uniformly. Due to the symmetric stress distribution patterns, only one direction is considered for lateral bending and axial rotation. Figure from Turbucz M and Fayad J et al. 2023 (91).

4.3. Part III. Results of the in silico investigation of different sacral fracture fixation techniques using two sets of bone material properties

4.3.1. Results of the finite element analysis of different sacral fracture fixation techniques

Implementing different meshing algorithms in the two bone modelling approaches led to a greater number of elements in the PSM than in the LBM, with 3,997,316 and 1,998,737 elements, respectively. The simulation times for the PSM and LBM were 4,270 and 1,554 seconds, respectively, indicating that the PSM required approximately 2.7 times more time on average.

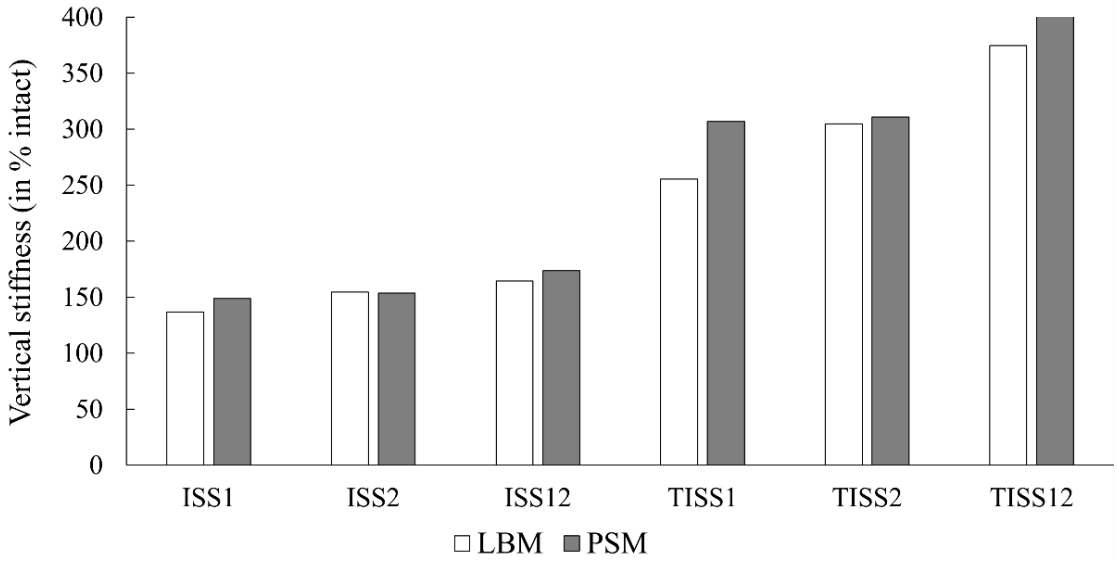

Figure 13. Normalised VS values of the different fixation techniques in LBM and PSM. Figure from Turbucz M et al. 2023 (136).

The VS results of each technique were normalised and presented in percentage, where 100% equalled the VS of the corresponding intact sacrum. The smallest VS was measured with the ISS1 technique, where LBM and PSM gave 137% and 149%, respectively, while the highest VS was achieved using the TISS12 configuration, where LBM and PSM gave 375% and 472%, respectively (Figure 13). No statistically significant difference was found between the LBM and PSM in terms of their VS predictions, as determined by the Wilcoxon signed-rank pair test ($p = 0.688$). The normalised VS results are detailed and shown in Figure 13.

The LBM's maximum von Mises stress value predictions in the implants were 73.3 MPa, 59.9 MPa, 40.4 MPa, 65.3 MPa, 44.2 MPa, and 35.2 MPa for ISS1, ISS2, ISS12, TISS1, TISS2 and TISS12, respectively. PSM, however, increased the maximum stress values

by 19.3%, 16.3%, 27.8%, 2.3%, 24.4% and 7.8%, respectively (Figure 14). A statistically significant difference was found between the LBM and PSM in terms of their maximum implant stress, as determined by the Wilcoxon signed-rank pair test ($p = 0.031$). The maximum stress values are shown in Figure 14.

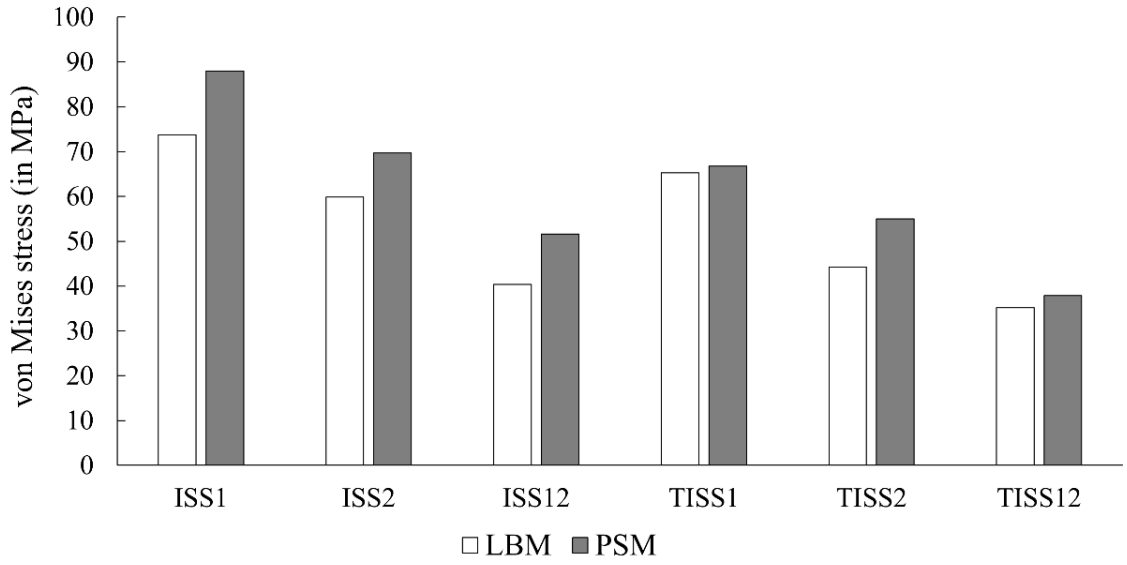

Figure 14. Maximum von Mises stress values in the implants for LBM and PSM. Figure from Turbucz M et al. 2023 (136).

The distribution of the RID values was analysed with the contact opening output from the Abaqus software. These values were plotted on the sacrum and shown in a sagittal view perpendicular to the fracture plane (Figure 15).

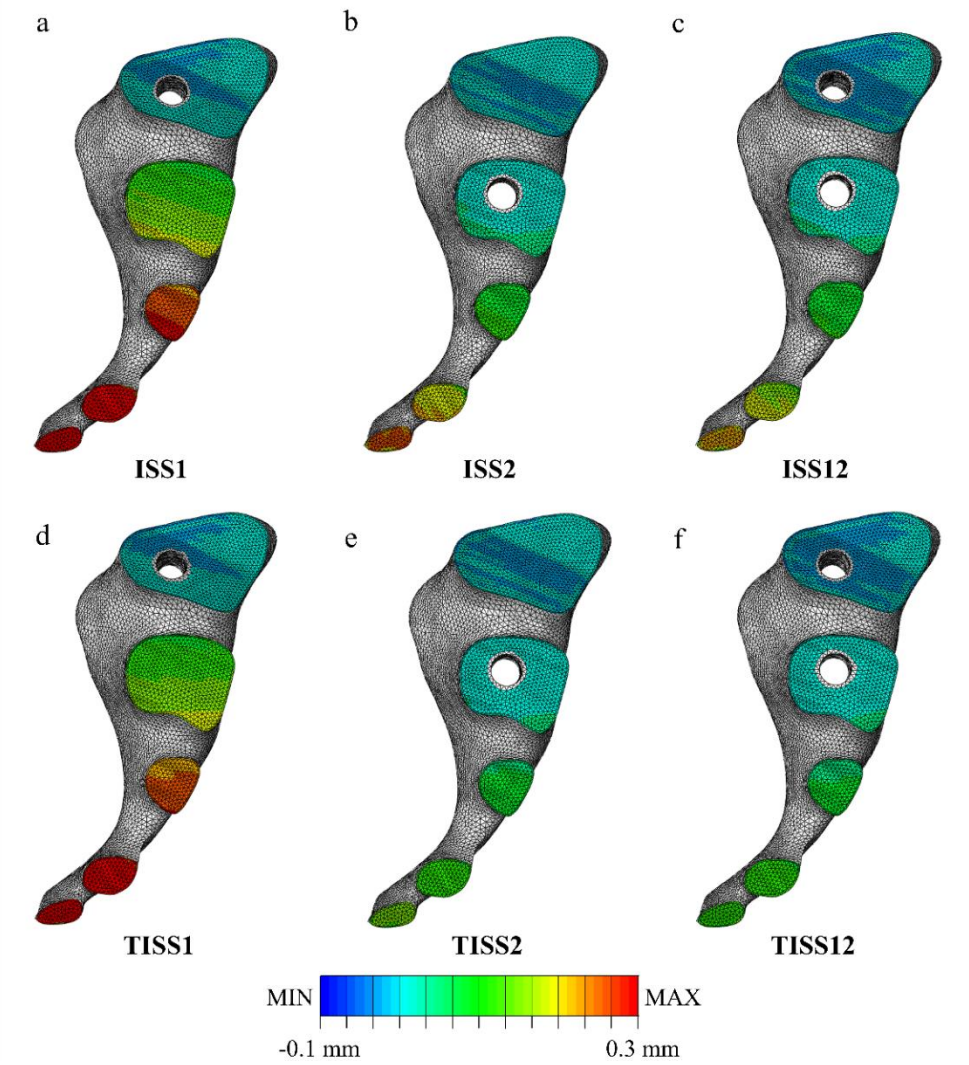

Figure 15. The distribution of the RID values in the LBM for (a) ISS1, (b) ISS2, (c) ISS12, (d) TISS1, (e) TISS2), and (f) TISS12 techniques with a uniform scale from -0.1 to 0.3 in mm. Figure from Turbucz M et al. 2023 (136).

In addition to the distribution, the maximum RID values were also recorded. They were between 0.10 mm and 0.47 mm for all fixation techniques in both models. In LBM, the maximum RID values were 0.47 mm, 0.27 mm, 0.25 mm, 0.37 mm, 0.15 mm and 0.14 mm for ISS1, ISS2, ISS12, TISS1, TISS2 and TISS12, respectively. No statistically significant difference was found between the LBM and PSM in terms of the maximum RID values, as determined by the Wilcoxon signed-rank pair test ($p = 0.438$). The maximum RID values are detailed in the Supplementary Figure 9.

Von Mises stress values on the fracture surface show distinctions between the two bone modelling strategies. The stress distribution between the LBM and PSM revealed strong

statistically significant differences across all fixation techniques ($p < 0.001$ for all pairs), as determined by the two-sample Kolmogorov-Smirnov test (Figure 16).

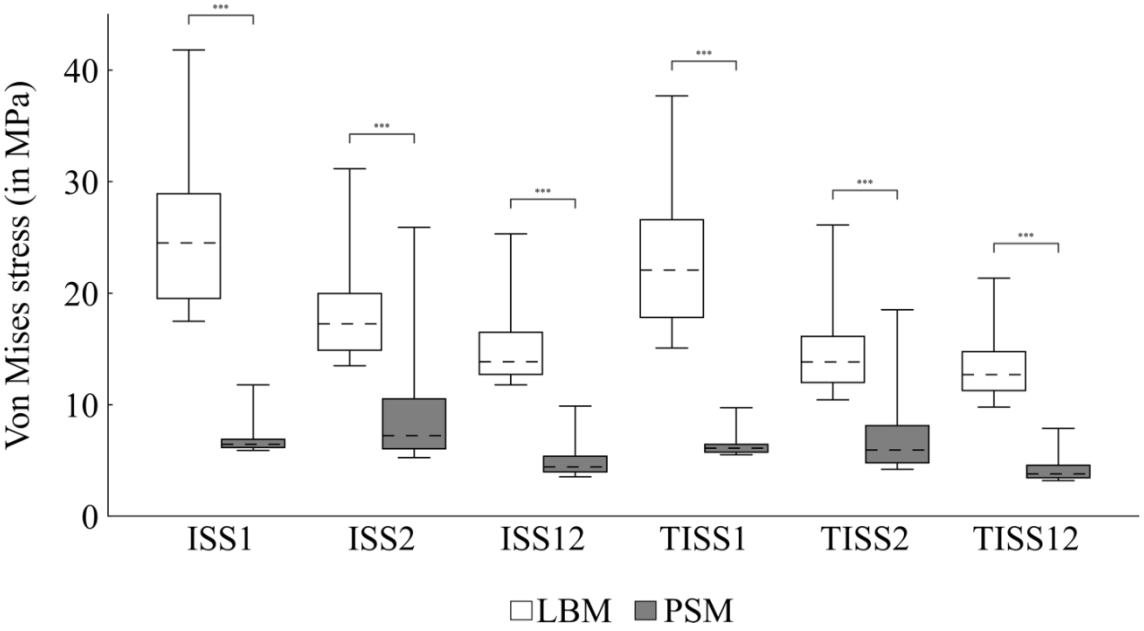

Figure 16. Boxplot figure with nodes from LBM and PSM that fell within the largest 1% of the von Mises stress values of the fracture surface. Median values are represented with black dashed lines, the minimum and maximum with error bars. (Two-sample Kolmogorov-Smirnov test, *** denotes p-values ≤ 0.001) Figure from Turbucz M et al. 2023 (136).

In the PSM, the median stress values were 6.5 MPa, 7.2 MPa, 4.4 MPa, 6.1 MPa, 6.0 MPa and 3.8 MPa for ISS1, ISS2, ISS12, TISS1, TISS2 and TISS12, respectively (Figure 16). However, LBM increased the median stress values by 280.1%, 138.8%, 212.9%, 261%, 132.4% and 234.7% compared to PSM. In the case of the maximum stress values, for ISS1, ISS2, ISS12, TISS1, TISS2 and TISS12, the LBM gave higher values by 255.1%, 20.3%, 156.4%, 286.9%, 41.1% and 171.1% compared to PSM (Figure 16). The boxplot figure of the stress values on the fracture surface, including the median, the minimum, the maximum values, and the statistical annotations, are shown in Figure 16.

4.4. Part IV. Results of the In silico investigation of different lumbopelvic reconstruction techniques after total sacrectomy

4.4.1. Results of the lumbopelvic reconstruction techniques validation

The shift-down displacement and relative sagittal rotation of L5 were calculated and compared to the findings of the cadaveric in vitro study by Cheng et al. and the in silico study by Zhu et al. (74,83). The results of this PhD thesis were within the standard deviation range of the in vitro experiment for all three reconstruction techniques (Figure 17). In the case of SRR and ICR, good agreement with the mean results of the in vitro experiment was observed, while for the FRR, the displacement and rotation of L5 were underestimated (83). However, excellent agreement was found with the in silico results for all LPRTs and both parameters (74). The validation results for the SRR, FRR, and ICR techniques are presented in Figure 17.

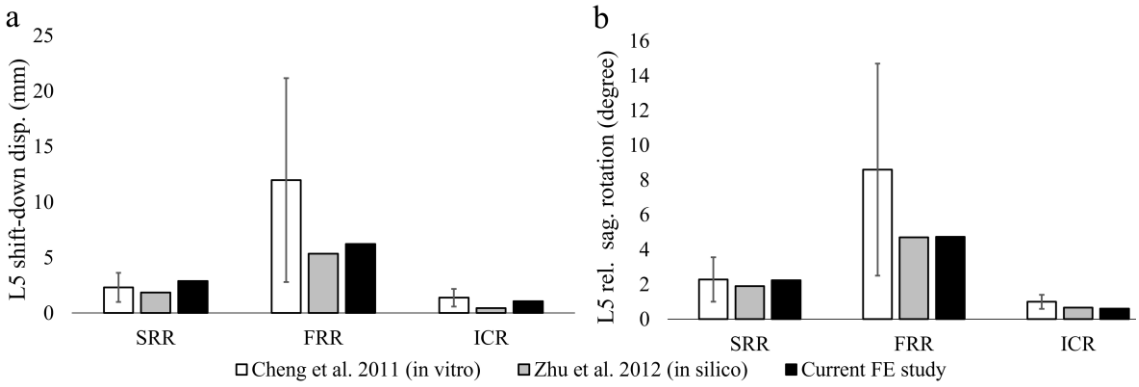

Figure 17. Results of the validation process. a) Shift-down displacement of L5 in mm calculated for the sacral-rod reconstruction (SRR), the FRR, and the ICR techniques. b) Relative sagittal rotation of L5 in degrees calculated for the SRR, the FRR, and the ICR techniques. The results of the PhD thesis were compared to previous in-vitro (83) and in-silico studies (74). Error bars represent the means and standard deviations. Figure from Turbucz M et al. 2024 (148).

4.4.2. Results of the finite element analysis of different lumbopelvic reconstruction techniques after total sacrectomy

The LPRTs ranked from smallest to highest displacement values as ICR<SRR<FRR<CLR for all loading cases, regardless of LPDR (Figure 18). For the ICR technique, the displacement values were 1.0 mm, 0.1 mm, 0.4 mm, and 0.4 mm for flexion, extension, lateral bending, and axial rotation, while for the CLR technique,

13.2 mm, 2.7 mm, 6.7 mm, and 6.9 mm, respectively. LPDR consistently reduced the displacement values. On average, the displacement was reduced by 25% in CLR, 61% in SRR, 15% in FRR, and 46% in ICR, based on all loading cases. The shift-down displacement values of L5 are detailed in Figure 18.

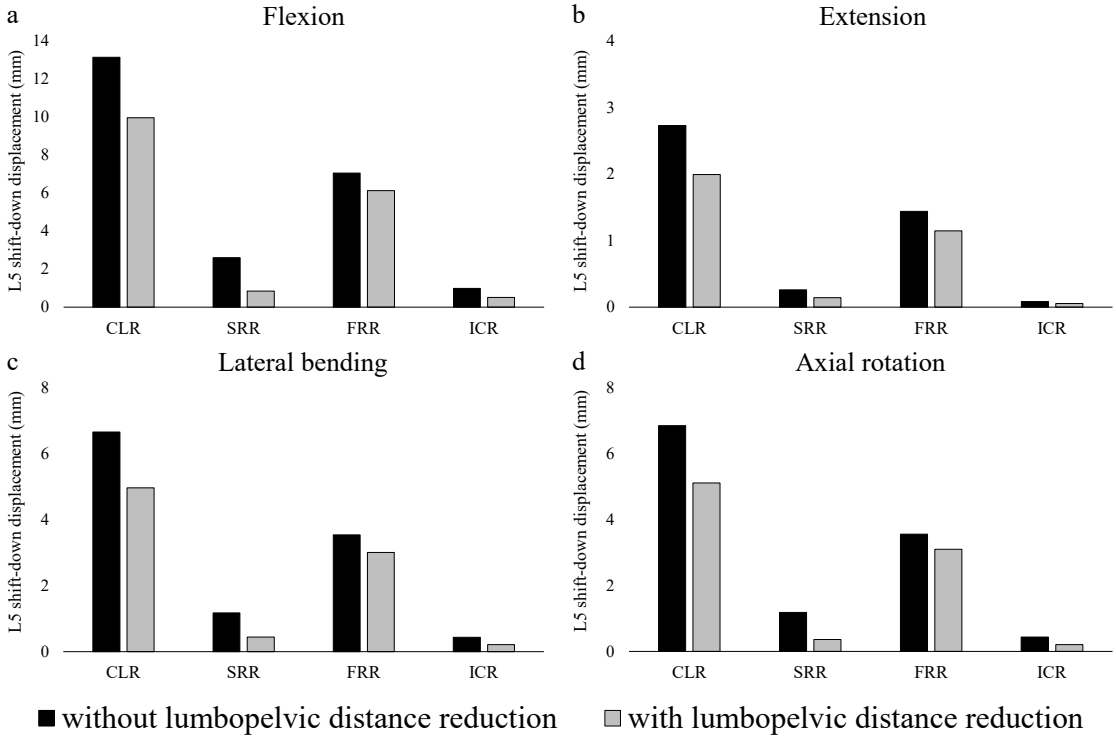

Figure 18. Shift-down displacement of L5, both with and without LPDR, in a) flexion (1175 N with 7.5 Nm), b) extension (500 N with 7.5 Nm), c) lateral bending (700 N with 7.8 Nm) and d) axial rotation (720 N with 5.5 Nm). Figure from Turbucz M et al. 2024 (148).

The LPRTs ranked from smallest to highest relative sagittal rotation values as ICR<SRR<FRR<CLR for all loading cases, regardless of LPDR (Figure 19). Without LPDR, the relative rotation values for the ICR technique were 1.0°, 0.2°, 0.5°, and 0.5° for flexion, extension, lateral bending, and axial rotation, while for the CLR technique, 10.8°, 2.3°, 5.5°, and 5.6°, respectively. LPDR consistently reduced the relative sagittal rotation of L5. On average, the rotation was reduced by 21% in CLR, 73% in SRR, 11% in FRR, and 53% in ICR, based on all loading cases. The relative sagittal rotation values of L5 are shown in Figure 19.

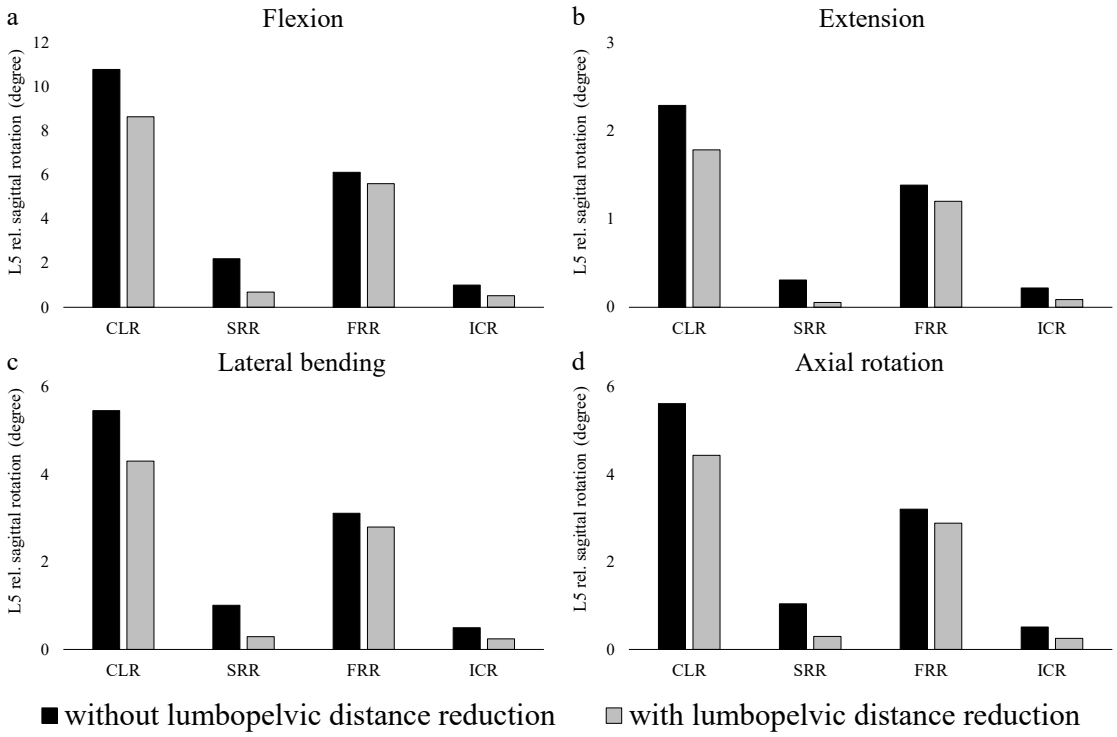

Figure 19. Relative sagittal rotation of L5, both with and without LPDR, in a) flexion (1175 N with 7.5 Nm), b) extension (500 N with 7.5 Nm), c) lateral bending (700 N with 7.8 Nm) and d) axial rotation (720 N with 5.5 Nm). Figure from Turbucz M et al. 2024 (148).

Without LPDR, the highest mean stress values were measured in the SRR technique with 217.5 MPa, 40.1 MPa, 105.9 MPa, and 108.8 MPa for flexion, extension, lateral bending, and axial rotation, respectively (Figure 20). With LPDR, the FRR technique gave the highest mean stress values for flexion, lateral bending, and axial rotation with 174.0 MPa, 82.1 MPa, and 89.1 MPa. However, in extension, the SRR technique induced the highest mean stress result with 36.1 MPa. With or without LPDR, the smallest mean stress predictions were given by the ICR technique for flexion, lateral bending, and axial rotation. Nonetheless, in extension, both with and without LPDR, the CLR technique yielded the smallest mean stress predictions with 32.3 MPa and 26.9 MPa, respectively. In general, LPDR decreased the mean stress values. On average, the mean stress values decreased by 13% in CLR, 26% in SRR, 19% in FRR, and 27% in ICR, based on all loading cases. The stress state of the bone-implant interface is detailed in Figure 20.

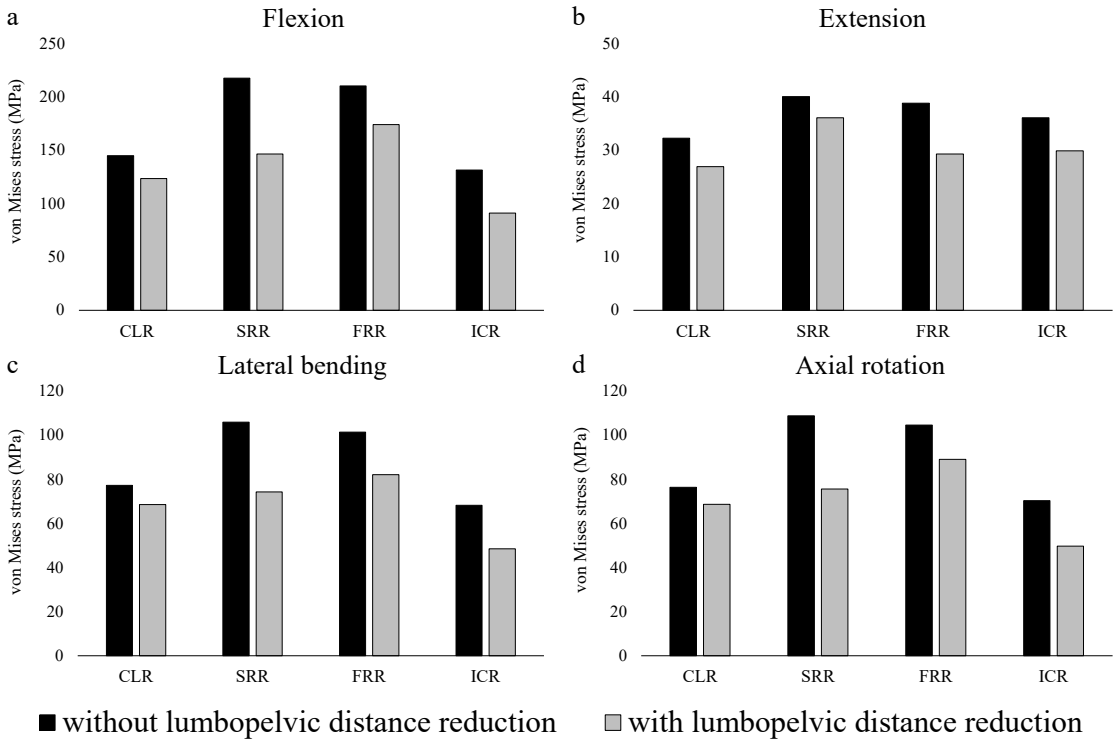

Figure 20. Mean von Mises stress calculated from the five nodes with the highest stress values at the bone-implant interface, both with and without LPDR, in a) flexion (1175 N with 7.5 Nm), b) extension (500 N with 7.5 Nm), c) lateral bending (700 N with 7.8 Nm) and d) axial rotation (720 N with 5.5 Nm). Figure from Turbucz M et al. 2024 (148).

The LPRTs ranked from smallest to highest mean stress values as ICR<SRR<FRR<CLR for all loading cases, regardless of LPDR. Without LPDR, in flexion, extension, lateral bending, and axial rotation, the ICR technique gave the smallest mean stress results with 346.5 MPa, 108.0 MPa, 186.2 MPa, and 199.7 MPa, while the CLR technique yielded the highest mean stress values with 955.9 MPa, 271.7 MPa, 585.6 MPa, and 585.0 MPa, respectively (Figure 21). Based on all loading cases, LPDR lowered the mean stress values within the rods by 25% and 12% in the SRR and ICR techniques, respectively. However, based on the average of all loading cases, in the FRR and CLR techniques, LPDR slightly increased the mean stress values by 5% and 2%, respectively. The stress state within the rods is detailed in Figure 21.

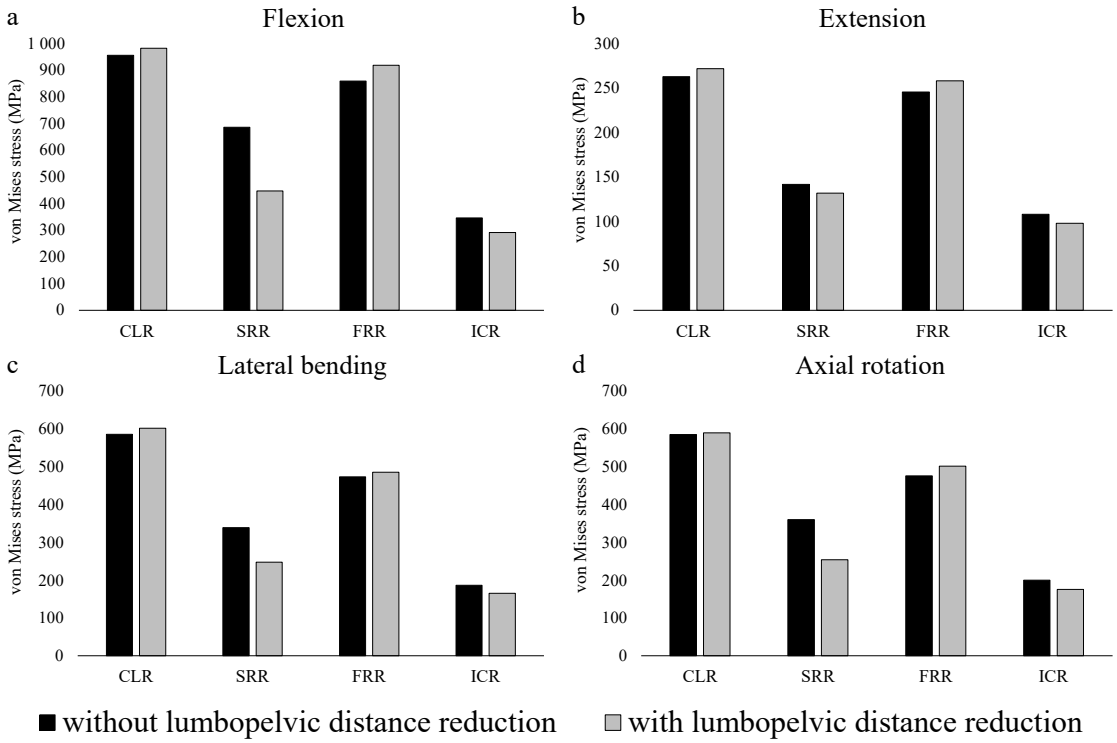

Figure 21. Mean von Mises stress calculated from the five nodes with the highest stress values within the rods, both with and without LPDR, in a) flexion (1175 N with 7.5 Nm), b) extension (500 N with 7.5 Nm), c) lateral bending (700 N with 7.8 Nm) and d) axial rotation (720 N with 5.5 Nm). Figure from Turbucz M et al. 2024 (148).

5. DISCUSSION

5.1. Part I. Validity of the healthy finite element models

Part I of this PhD thesis aimed to outline the validation procedures, which are an essential initial step for all in silico investigations using the FE method. First, the development and validation of the healthy human lumbar spine were presented, employing a patient-specific bone assignment approach. Subsequently, the thoracolumbar region of the spine was developed, calibrated, and validated using a literature-based bone modelling technique. Finally, the development and validation of the healthy human pelvis were presented with bony tissues modelled as rigid bodies.

Dreischarf et al. described that the validation via diverse results increases the accuracy and reliability of the developed models' predictions (7). Therefore, validation was performed utilising several published experimental and in silico results.

The results of the lumbar spine FE model were in good agreement with the published in silico and in vitro studies for L1–L5 ROM in flexion-extension, lateral bending, and axial rotation (Figure 8a). However, the nonlinear load-displacement curve demonstrates that in flexion and extension, the FE model is slightly outside the in vitro range (Figure 8b). A similar trend is reported by Dreischarf et al, that the majority of their assessed FE models overestimate the motion in extension and underestimate it in flexion (7).

In pure bending, the results of the lumbar spine FE model show good agreement with the available in vitro (124) and in silico (7) data, although a slight overestimation of the in vitro result appeared in extension (Figure 8c). The results indicate that the FJF in lateral bending is notably lower than in extension and axial rotation, which may originate from the patient-specific anatomy, agreeing with the findings of Woldtvedt et al. (151). In flexion, no FJF was transmitted due to the lack of contact (127). The IDP prediction of the FE model in pure compressive follower load showed excellent agreement with the median in vitro results at 300 N and 1000 N (Figure 8d).

The IVR values were obtained and evaluated for both pure and combined load cases (Supplementary Figure 2a–h). Wilke et al. previously reported that a pure bending moment of 7.5 Nm is the most appropriate for simulating the loads on the lumbar section to account for the effects of muscle forces (116). The IVR results of a cadaveric test by Panjabi et al. (126) and an FEA by Remus et al. (103) were used as a basis for comparison in the case of pure bending load.

The employed combined loads were determined by Rohlmann et al. and Dreischarf et al., using follower load and bending moment combination that most closely approximates the average of in vivo measurements reported in the literature (127,152,153). In the case of combined load, the average of three in vivo measurements (119–121) was used as a basis for comparison when evaluating the IVR results. In both load cases, the IVR predictions of the current FE study agree with the experimental results in extension, lateral bending, and axial rotation, while the simulations underestimated the experimental results in flexion (Supplementary Figure 2). The predictions of the current FE investigation are comparable to the in silico findings reported by Remus et al. and Dreischarf et al. (7,103). The predicted IDP values for combined load were compared to the mean of eight well-accepted in silico results (7) and to an in vivo analysis by Wilke et al. (122). Excellent agreement with the in vivo and in silico results indicates that the model can predict the IDP values accurately (Supplementary Figure 3).

In the case of combined load, the FJF values were compared to those mean in silico results reported by Dreischarf et al. (7) (Supplementary Figure 4). In general, the validated in silico studies show a significant variance regarding the FJF's magnitude, indicating that this force is sensitive to the FE modelling techniques and the patient-specific anatomy. This finding is also supported by Schmidt et al., who found that the FJF is highly dependent on the individual geometry of facet joint surfaces (154). In flexion, no force occurred due to the lack of contact. In extension, the magnitude of the FJF increases caudally, agreeing with the results reported by Remus et al. (103). In lateral bending, FJF occurred only at the L4–L5 spinal level, as it was reported in several models investigated by Dreischarf et al. (7).

Although the validation results of the LBM are not included in the current PhD work, the LBM and PSM were compared in terms of computational times. These comparisons are drawn from the publication entitled *"Development and Validation of Two Intact Lumbar Spine Finite Element Models for In Silico Investigations: Comparison of the Bone Modelling Approaches,"* co-authored by myself and Agoston Jakab Pokorni, who developed the literature-based lumbar spine FE model. Generally, employing the literature-based modelling approach reduced the required CPU time, as the PSM notably required more time to complete for both pure and combined loads. Notably, in the case

of patient-specific bone material assignment, the computational cost dramatically increased due to the different meshing algorithms applied (Supplementary Figure 5).

In this section of the PhD work, the objective was to develop, calibrate, and validate the literature-based FE model of the healthy thoracolumbar spine. As a starting point, the 3D geometry models of the thoracic and lumbar regions were registered and aligned based on the L1 vertebra. The HD is a well-accepted and widely used criterion for evaluating the quality and accuracy of the segmentation and registration process (155). The HD associated with the segmentation process represents the registration quality, as a lower HD value means higher accuracy (155). The average HD value between the L1 vertebrae of the lumbar and thoracolumbar regions (minimum = 0 mm, maximum = 1.37 mm, mean = 0.15 mm, root mean square = 0.2 mm) suggests that the registration quality is satisfactory and does not undermine the outcomes of subsequent biomechanical analysis. Previous studies described the material properties of the lumbar spine region; those parameters were adopted in the current FE investigation for the whole thoracolumbar (T7–L5) region (109,111,113,114,132,133). However, the biomechanical characteristics of the thoracic region differ from those of the lumbar spine (135). This difference is due to the smaller IVD height, the rib cage, the stabilisation effect of the thicker thoracic ligaments, and the presence of costovertebral joints (135). To offset this effect, a careful calibration was performed to adjust the IVR predictions of the thoracic region to multiple experimentally obtained in vitro results (123,134,135). The calibration process was accomplished by varying the weighting factor of the AF, considering the physiological limits reported in the literature (111). The calibration resulted in a T7-L5 FE model validated against IVR and ROM of the spinal segment, therefore suitable for further biomechanical analysis (Supplementary Figure 6, Supplementary Figure 7, Supplementary Figure 8).

Previously, a mesh convergency study was performed, which reported the adequate element sizes for both the LBM and the PSM to ensure accurate FE results (63). Dreischarf et al. emphasised the importance of validating anatomical FE models with diverse studies, enhancing their reliability and predictive capability (7). Therefore, displacement and rotation values of the SIJ were compared with an in vitro experiment by Miller et al. and various in silico studies. Overall, the validation results agreed well

with the published measurements (Figure 9) (137,142–144). Consequently, the developed healthy pelvis FE model is suitable for further in silico investigations.

5.2. Part II. In silico investigation of different spinal fixation techniques

Following a long-instrumented posterior spinal fusion, PJK remains a relatively common complication. This well-known mechanical complication is also present in the National Center for Spinal Disorders, making it crucial to analyse the biomechanics behind its phenomenon. The risk factors associated with PJK vary on an individual basis, such as older age, high body mass index, low BMD, comorbidities, the surgical approach, instrumentation type, amount of deformity corrections, position of the UIV, and number of fused vertebrae (156–158). Previously, the sudden change in mobility was also identified as one of the risk factors reported by Kim et al. (159). In line with this recognition, multiple surgical procedures and instrument types have been developed to dampen this phenomenon and help the transition to normal motion at the junctional level (29,30,34). The proposed surgical solutions include conserving the posterior ligament complex and augmentation with polymethyl methacrylate. Furthermore, the application of semirigid fixation systems, such as TPHs, transition rods, or various types of elastic tethers or tapes, was also investigated.

The results of this section of the PhD highlight that SFTs increase mobility and provide a more gradual transition in motion between the instrumented and non-instrumented spinal segments. The utilised FE method allows for comparing different techniques under identical anatomy and loading conditions, indicating that biomechanical differences are solely due to the fixation technique used.

A modified multidirectional hybrid test protocol was employed, originally introduced by Panjabi (146). This loading method is particularly suitable for investigating adjacent segment effects, as it consists of two successive and related loading steps. First, in the load-controlled step, a pure bending moment of 5 Nm was applied to the intact and instrumented models, and then the IVR results of the intact model were used to normalise the predictions of the fixation techniques for the sake of better comparison with other investigated SFTs (33–36). Subsequently, a displacement-controlled load was applied to the rigid and two SFTs until the desired ROM from the first step was achieved. Although Panjabi suggested using the displacement of the intact spinal segment, corresponding

values of the TRF technique were employed to obtain physiologically suitable results and ensure direct comparison based on the pedicle screw load.

The current FE investigation's findings agree with previously published in silico and in vitro studies (33,35) in that the SFTs allow a more gradual transition to normal motion. According to the current models' predictions, MRF and PRF behave less rigidly at the junctional level in all loading directions, especially in lateral bending and axial rotation. In axial rotation, the advantages of the SFTs are clearly visible as they provided substantially higher IVR values compared to the rigid technique. Similar findings were described by Doodkorte et al. (33), namely that in axial rotation, the semirigid spinal instrumentations behave less rigidly and increase the mobility of the spinal segments at the UIV level. In lateral bending, all fixation techniques significantly limit the motions below the UIV level; thus, the role of the "dampening zone" increases to help the transition between the instrumented and intact segments of the spine. In addition, similar results were found in a recent cadaveric in vitro experiment by Pereira et al., who investigated the biomechanical effect of PEEK rods connected to long posterior titanium fixation (160). They concluded that extension using PEEK rods allows redistribution of the load on the adjacent levels and decreases adjacent-level hypermobility that might be a risk factor to PJK.

The investigated SFTs countered the rigid technique in that a connector device was used to join the different systems. This connector itself can increase the mobility of the construct. Accordingly, to avoid biased conclusions, the effect of the connector device on mobility was investigated in Supplementary Study 1 by creating and analysing a theoretical titanium-titanium fixation technique. The results help separate the biomechanical effects of the connector device and the fixation techniques, thus allowing appropriate conclusions. Based on the results described in Supplementary Study 1, the connector device alone does not significantly influence mobility, and the SFTs are responsible for most mobility increases and load reduction.

Pedicle screw load is an essential factor when it comes to the comparison of different fixation techniques (35). The load of the pedicle screws indicates that the application of SFTs generally reduced the maximum stresses in all fixation techniques and for all loading directions at the UIV level. It is noteworthy that below the junctional level, the maximum stress values are relatively high for axial rotation compared to other loading

modes. The ability of SFTs to reduce the pedicle stresses also has clinical implications, as it means a lower probability of vertebral compression fractures and pedicle screw pullout (35). In addition, the decreased screw load helps prevent endplate fractures at the UIV+1 level (35). Based on these results, using SFTs reduced the load and increased the mobility at the UIV level; hence, these SFTs contribute to the unloading of the adjacent segment and thus reduce the risk of developing PJK.

Results of this part of the PhD thesis can serve as valuable input for future product development in the field of spinal fixation techniques. The connector device presented in Part II has received a utility model protection in 2022 from the Hungarian Intellectual Property Office (U 22 00053). These developments underscore the potential for innovation in spinal fixation. Based on these results, MRF and PRF techniques could reduce the risk of developing PJK after long thoracolumbar fusions. However, additional biomechanical studies and comprehensive clinical trials are recommended to analyse the clinical outcomes of these biomechanically supported load distributing SFTs.

5.3. Part III. In silico investigation of different sacral fracture fixation techniques

The surgical treatment of unstable posterior pelvic ring injuries caused by traumas is challenging due to the complex local anatomy and unique biomechanics (161). Extensive research has been conducted to investigate the fixation techniques, both experimentally and computationally (43,48,55–59). Despite the BMD difference between the S1 and S2 bodies reported in the literature (62), no previous biomechanical in silico study included patient-specific bone material properties. Therefore, this section of the PhD work aimed to investigate the biomechanical characteristics of ISS and TISS techniques using two bone modelling strategies. However, it is important to note that inserting any screws at the S2 level or TISSs at the S1 level may not be feasible due to individual morphological variations (51).

VS values are commonly used to assess biomechanical stability (57). Generally, the use of TISS allows higher stability regardless of the screw position compared to the configurations with ISS (Figure 13). The outcomes indicate that using even one TISS provides higher stability than inserting two ISSs. The statistical test revealed that the LBM and PSM predict similar trends regarding biomechanical stability. However, some differences can be observed. The VS predictions of the LBM suggest that placing one screw at the S2 level increases stability compared to the S1 placement. At the same time,

PSM demonstrates no change in VS (ISS1 vs ISS2 and TISS1 vs TISS2, Figure 13). These results indicate that the LBM underestimated the bone quality at the S1 level as PSM gave higher VS than the LBM in the case of ISS1 and TISS1.

Analysing the maximum von Mises stress in the screws is important for implant safety (57). In this PhD thesis, the maximum stress values remained below the yield stress of the titanium for all fixation techniques (57), indicating that the non-fatigue failure of the implants is not predicted. Applying two screws is beneficial, as the ISS12 and TISS12 gave the two lowest maximum stress values. The maximum stress values in the ISS2 and TISS2 were lower than in the ISS1 and TISS1, respectively, indicating that inserting the screw at the S2 level is more beneficial for implant safety. These results show excellent agreement with the findings of Fu et al., who showed that placing screws both at the S1 and S2 levels results in the lowest maximum stress values and found that TISS12 were the most effective for stress reduction. In addition, they concluded that placing screws at the S2 level is more advantageous compared to the S1 level placement concerning implant safety (55).

Despite the agreement in biomechanical stability, the stress distributions revealed significant differences between the LBM and PSM. On average, PSM gave 16% higher maximum stress values than the LBM, indicating that the heterogeneity of locally defined bone material properties increases the predicted von Mises stress values in the implant. The difference in the stress values confirms the findings by Synek et al., who reported that modelling the heterogenous and orthotropic properties of the bone influences the stress significantly in the inserted implant (162).

RID values are commonly used in the literature to evaluate the ability of fracture healing. The biomechanical studies by Acklin et al., Hu et al., Peng et al. and Zheng et al. all included this parameter to assess sacral fracture fixation techniques (43,48,57,59). Peng et al. reported that RID values below 1 mm meet the clinical requirement for biomechanical stability (43). The RID results from this section of the PhD work indicate that all configurations can provide biomechanically stable solutions for sacral fracture management, as the maximum RID values for all configurations remained below 1 mm, with the TISS12 and TISS2 techniques demonstrating the highest stability among the configurations (Supplementary Figure 9). The distribution of the RID values highlights the symmetry of the biomechanical stability of the fixation techniques, for which

analysing only the maximum values is not possible (Figure 16). Peng et al. compared the biomechanical properties of TISSs with lumbopelvic and bilateral triangular fixation, using multiple points to measure RID (43). They found that the TISS12 fixation can provide superior results, allowing more symmetrical displacement distribution. In this PhD thesis, TISS12 yielded the lowest RID values at the caudal part of the sacrum, indicating symmetrical behaviour besides its highest stability. The RID predictions of the LBM and PSM did not differ significantly, as shown by the statistical test, meaning that the locally defined material properties did not affect the maximum RID predictions (Supplementary Figure 9). For that reason, in Figure 15, only the results of the LBM are presented.

Claes et al. have performed a combined animal and in silico investigation to determine the role of stress and strain on fracture healing. They found that a relatively low-stress range promotes, while an excessive stress state retards osteoblast proliferation and activation (163). Therefore, the stress values allowed to rank the configurations based on their ability to promote fracture healing. Generally, the statistical test shows that stress values in the PSM were significantly lower than in the LBM (Figure 16). The locally defined bone materials in the PSM reveal that screw insertion at the S2 level notably increases the stress on the fracture surface. However, based on the LBM's prediction, a screw at the S2 level is more advantageous than a screw at the S1 level. Therefore, similarly to the VS predictions, the literature-based bone materials underestimated the bone quality at the S1 level, as both ISS1 and TISS1 revealed a low-stress state when modelled with patient-specific bone, indicating superior fracture healing promotion ability.

The stress distribution patterns on the fracture surface were also analysed, which revealed that in the LBM, the load is primarily borne by the cortical shell (Supplementary Figure 10). In contrast, in the PSM, the stress distribution patterns are more realistic than the stress distributions in the LBM (Supplementary Figure 11). These results suggest that the patient-specific bone modelling approach enables more accurate prediction of stress distributions, making it advantageous for ranking techniques in terms of fracture healing ability. The stress values on the bone-implant surface were also investigated (Supplementary Figure 12), demonstrating lower stress values with the PSM compared to the LBM for all configurations. Placing a single screw at the S2 level instead of the S1

level increased stress in the surrounding bone, increasing the probability of screw loosening (ISS2 vs ISS1 and TISS2 vs TISS1). These findings agree with the recommendation of Radley et al. to prioritise the S1 body over S2 in sacral fracture fixations (62).

The two bone modelling strategies consistently ranked the techniques based on vertical stability and maximum RID values. However, von Mises stress values revealed significant differences between the two approaches. On the fracture interface, PSM gave notably lower maximum stress values than LBM for all fixation types. On the other hand, PSM gave higher maximum implant stress values than LBM. Consequently, using locally defined bone material properties provides advantages in predicting the stress-shielding phenomenon, as opposed to relying on literature-based bone material properties. However, both bone modelling strategies can adequately rank fixation techniques based on global stability, reducing computational requirements. Therefore, both strategies are suitable for performing biomechanical studies.

5.4. Part IV. In silico investigation of different lumbopelvic reconstruction techniques

Over the past few decades, numerous LPRTs have been introduced and extensively analysed both in vitro (83–85,164–166) and in silico (74,76,82,86,167,168). However, the previous FE investigations did not consider the effect of LPDR. Therefore, the current section of the PhD thesis work assessed the biomechanical impact of LPDR on four LPRTs by evaluating both implant safety and lumbopelvic stability.

The FE models of the intact lumbar spine and pelvis were previously developed, verified, validated, and described in this PhD work. In addition, the FE mesh of the pedicle screws and spinal rods has been employed in previous research (91). However, to further increase the reliability of the current FE investigation (7), the shift-down displacement and relative sagittal rotation of L5 were compared with in vitro and in silico results for the SRR, FRR, and ICR techniques (74,83). Good agreement was found with the previously published results, although the FRR predictions slightly underestimated the in vitro mean results (Figure 17). Since the CLR technique is structurally similar to the other validated LPRTs, all techniques are suitable for comparative biomechanical analysis.

Shift-down displacement and relative sagittal rotation of L5 are commonly used to characterise the lumbopelvic stability of various LPRTs following total sacrectomy

(74,83,86). Both of these parameters consistently ranked the LPRTs, with the ICR technique demonstrating the highest lumbopelvic stability (Figure 18 and Figure 19). In their cadaveric in vitro study, Cheng et al. also concluded that the ICR technique, due to its combined anterior and posterior stabilisation, provides the highest biomechanical stability compared to other LPRTs, including the SRR and FRR techniques (83). Employing FE analyses, Zhu et al. arrived at the same conclusion and found that the ICR technique outperforms other investigated LPRTs from a mechanical perspective (74). In general, LPDR consistently improved lumbopelvic stability across all the analysed LPRTs and all loading conditions.

Among the investigated LPRTs, the CLR technique exhibited the lowest lumbopelvic stability with the highest shift-down displacement and relative sagittal rotation of L5. Eltes and Turbucz et al. reported a 6-year-long follow-up study of a patient stabilised with the CLR technique after total en bloc sacrectomy (88). They found that CLR technique provides a non-rigid fixation, as considerable rod deformation was measured during the study period (88). Despite this, adequate bony fusion was reported without any hardware failure (88). Considering that the CLR technique had the lowest lumbopelvic stability and given its reported favourable clinical results, it suggests that, from a biomechanical point of view, all the analysed LPRTs are suitable for lumbopelvic reconstruction.

Bone is an orthotropic material, meaning its mechanical properties, such as yield strength, vary in tension, compression, and torsion (169). Since, in this PhD thesis, bone tissues were assumed to have homogenous and isotropic linear elastic material properties, comparison to a single yield strength value oversimplifies the situation and may introduce potential errors (76,170). Therefore, the stress values were solely used to rank LPRTs based on the risk of promoting screw-loosening.

Without LPDR, the SRR technique induced the highest bone stress around the implant for all loading cases (Figure 20). These high stress values were located near the sacral rod, which aligns well with findings from the experimental study by Murakami et al. (76). Although the ICR technique also includes the sacral rod, it produced the lowest stress results in flexion, lateral bending, and axial rotation, and the second lowest to the CLR technique in extension. This suggests that the bilateral fibular graft construct and the four longitudinal rods effectively reduce stress concentrations in the bone. These results are consistent with the findings of Yu et al., who examined strain at the bone-implant

interface in both the SRR and ICR techniques (87). Their cadaveric in vitro study showed that the ICR technique is the most effective in load sharing among the LPRTs they studied (88). With LPDR, the FRR technique gave the highest stress in flexion, lateral bending, and axial rotation and the second highest in extension (Figure 20). The lowest stress values were recorded in the same techniques as without LPDR: ICR for flexion, lateral bending, and axial rotation, and CLR for extension. In general, LPDR decreased stress values in all techniques and loading directions, suggesting that reducing the lumbopelvic distance is advantageous in preventing possible screw-loosening (Figure 20).

The applied initial conditions significantly influence the stress values measured within the rods. An ideal, rigid connection was modelled between the screw heads and the rods. However, in reality, such connections often have some flexibility. To avoid potential errors and ensure adequate conclusions, the stress values were solely used to rank LPRTs based on implant safety, and they were not compared with any failure criteria. Interestingly, the influence of LPDR was less unidirectional compared to bone-implant stress (Figure 21). LPDR notably reduced stress values in the SRR and ICR techniques due to the reduced load on the horizontal sacral rods. Nonetheless, in the FRR and CLR techniques, stress even slightly increased. This might be because the rods are more bent to fit within the decreased lumbopelvic area, which bending then increases the peak stress values within the rods. However, on average, this stress increase was less than 5%.

In recent years, patient-specific 3D printed implants were introduced and analysed in the literature, offering an innovative solution for sacral replacement and lumbopelvic reconstruction (86,171). Although these implants have shown promising biomechanical results (86,171), the biomechanical impact of LPDR was not considered. Based on the findings of this section of the PhD work, it is recommended that future custom-made lumbopelvic reconstruction devices incorporate LPDR. Nonetheless, their clinical efficacy still needs to be verified in long-term clinical investigations.

In all the investigated LPRTs, LPDR consistently improved both lumbopelvic stability and implant safety. This anatomical modification notably reduced the shift-down displacement of L5, the relative sagittal rotation of L5, and the stress values at the bone-implant interface. Therefore, performing LPDR creates a biomechanically more advantageous environment regardless of the reconstruction techniques. The ICR technique demonstrated the highest lumbopelvic stiffness, contrasting with the CLR

technique, which resulted in the lowest stiffness. Nonetheless, based on the findings of this section of the PhD work, from a biomechanical point of view, all LPRTs are suitable for lumbopelvic reconstruction.

Sacrectomies were historically performed through combined anterior-posterior approaches. However, this procedure resulted in long operative times and significant trauma to the patient (172). To address these issues, a posterior-only approach was developed for tumours that did not invade the pelvic organs or extend beyond the lumbosacral junction (172). Nonetheless, it is important to note that performing a sacrectomy with an anterior-posterior approach does not necessarily indicate the need for combined anterior-posterior stabilization in subsequent lumbopelvic reconstruction techniques. However, while biomechanical factors hold significance, they alone are not decisive in selecting the suitable reconstruction technique. The selection of an appropriate technique should be a collaborative decision by the surgical team, considering their expertise and all available patient-specific information.

5.5 Limitations

Similar to all other in silico analyses, this PhD thesis contains limitations worth highlighting. All presented results are based on nonlinear static FE analysis, which cannot account for long-term physiological functions as it is based solely on mechanical theories (63,91). The healthy FE models developed in this PhD thesis were based on the anatomy of a healthy 24-year-old male, omitting anatomical variations associated with degeneration, age or sex.

In Part I, the viscoelastic and poroelastic characteristics of the IVDs were not considered since a static FEA was performed, and different time-dependent behaviours, such as creep, were outside the interest of the study. However, the presented patient-specific lumbar spine FE model can be further developed by increasing the number of material groups in the patient-specific bone material assignment or modelling the NP as an incompressible fluid cavity and including an initial hydrostatic pressure field. Although the model could be improved by addressing these simplifications, the presented patient-specific FE model is suitable for drawing conclusions and further biomechanical investigations.

In the FE model of the thoracolumbar spine, the stabilising effects of the rib cage, thoracic wall muscles, and costotransverse and costovertebral ligaments were not included, nor

was the effect of the upper body weight. Therefore, in Part II, only normalised IVR values were given to avoid including unrealistic motion values originating from the listed simplifications. Nevertheless, the current FE analysis allowed a direct biomechanical comparison between the presented rigid and semirigid spinal fixation techniques using identical anatomy and loading conditions. The computational model could be further developed by considering the mentioned limitations. However, the relative difference between the techniques would remain the same; thus, the presented results provide a satisfactory basis for comparison. However, the model could be extended cranially in future work to allow a more detailed biomechanical analysis at the UIV+2 and UIV+3 levels.

In Part III, the ISS geometries were simplified; therefore, the magnitude of the stress in the bone around the screw could not be predicted accurately (173). Due to the static load applied, accurately predicting time-dependent failure modes such as fatigue and creep was not possible. In addition, only standing on both feet was considered, and other physiological movements, such as flexion, extension, lateral bending and axial rotation, were not included. The employed relationship between the HU and elastic moduli was determined for the lumbar spine and not specifically for the pelvis. However, the relative difference between the techniques would remain the same after eliminating the mentioned limitations. Since the nature of FE analyses cannot accurately predict clinical outcomes, long-term clinical studies (multicentric, retrospective and prospective) are recommended.

In Part IV, the muscle forces were not considered. Due to the applied initial conditions between the screw heads and the rods, accurate prediction of the stress within the rods was not feasible. Additionally, the screw geometries were simplified, limiting the precise prediction of stress values at the bone-implant interface (173). Consequently, in Part IV, the stress-state analysis was employed primarily for ranking LPRTs based on their likelihood of screw-loosening and implant safety. Despite these acknowledged limitations, the FE analysis presented in Part IV enabled a direct biomechanical comparison between LPRTs with and without LPDR. Nevertheless, it is essential to emphasise the need for comprehensive clinical trials (multicentric, retrospective, and prospective) to interpret the findings of this biomechanical comparison adequately.

6. CONCLUSIONS

The main aim of this PhD thesis was to highlight the significance of using in silico methods to understand the biomechanics associated with different surgical interventions. In the development of the lumbar spine, the aim was to present the development and validation process of the healthy human lumbar spine FE model using a patient-specific bone material assigning technique. The mesh resolution was investigated to ensure accurate model predictions. The results of the FE model were compared with in vivo, in vitro, and well-accepted in silico data from the literature. Validation was performed considering ROM, IVR, IDP, and FJF variables against pure and combined loads. Based on the parameters and loads investigated, the developed FE model can be used to model the biomechanical properties, such as ROM, IVR, FJF, and IDP of the lumbar spine, as it is in good agreement with the previously published results in most investigated variables. However, substantial differences in computational time between the literature-based and patient-specific bone material assignment techniques were observed.

In part II, the previously developed and validated literature-based thoracolumbar spine FE model was used to investigate PJK, a frequent and clinically significant mechanical complication following long instrumented spine surgeries. In this part, FEA has been used to evaluate the effect of two SFTs compared to one conventional rigid fixation technique. In agreement with the literature, based on the findings in this FEA, less rigid fixations at the cranial part of the stabilisation construct allow a more gradual transition in motion between the instrumented and intact spine segments. Decreasing the load on the pedicle screws at the upper instrumented level could help prevent the development of PJK.

Part III of this PhD thesis used the previously developed healthy pelvis FE model to investigate different sacral fracture fixations. Since an increasing number of sacral fractures are undergoing surgical management, clinicians must know the biomechanical properties of the available fixation techniques. Part III analysed six fixation techniques for treating unilateral sacral fractures using FEA, employing both patient-specific and literature-based bone material properties. Only ISSs or TISSs were used for sacral fracture fixation, thus preserving lumbar mobility. Based on the results, all analysed configurations provide clinically sufficient stability. From a biomechanical perspective, TISS12 outperformed all other fixations, delivering the greatest vertical stability and the least interfragmentary displacement and implant stress. These findings suggest that sacral

fracture fixations should prioritise the S1 level over the S2 as both ISS2 and TISS2 increased the stress on the fracture interface and the bone-implant surface compared to ISS1 and TISS1, respectively. Both the PSM and LBM pelvis models consistently ranked the fixation techniques based on their ability to provide vertical stability and based on RID values. However, the observed differences in stress distribution emphasise the need for meticulous care when selecting the suitable bone modelling strategy depending on the aim of the study. It is important to note that the PSM while offering more realistic stress distribution results, requires additional computational resources compared to the LBM.

In Part IV, the lumbar part of the literature-based thoracolumbar spine FE model and the pelvis FE model were combined to evaluate and compare the biomechanical characteristics of four different LPRTs while considering the effect of LPDR. Regardless of the reconstruction techniques employed, LPDR improves lumbopelvic stability following total sacrectomy by reducing the shift-down displacement and relative sagittal rotation of L5. Furthermore, LPDR decreases the stress at the bone-implant interface, lowering the risk of screw loosening. This technique also reduces the stress within the rods, particularly in techniques combining both anterior and posterior stabilisation. The ICR technique demonstrated the highest lumbopelvic stiffness, while the CLR technique showed the lowest. However, based on the findings, all techniques are suitable for lumbopelvic reconstruction. The ultimate selection of the appropriate technique should be a decision made by the surgical team based on their expertise and various patient-specific aspects.

In conclusion, through the development and validation of FE models, insights were gained regarding the biomechanical properties of the lumbar spine, thoracolumbar spine, and pelvis, as well as various fixation techniques and reconstruction methods. These findings provide practical contributions to evidence-based clinical decision-making and potentially enhance patient outcomes in spinal care. Nonetheless, further biomechanical investigations and long-term clinical trials are recommended to validate the presented findings and ensure their applicability in real-world clinical practice.

7. SUMMARY

In Part I, three healthy FE models were developed and validated. Regarding bone modelling approaches, this section introduced two types of bone modelling strategies: a patient-specific approach for the lumbar spine and a literature-based technique for the thoracolumbar spine. The FE model of the healthy pelvis was developed using both strategies and was validated with bony tissues as rigid bodies. Based on the results of the validation processes, all three FE models are suitable for further biomechanical analysis, as they agree with available in vitro, in vivo and in silico data from the literature.

In Part II, the validated thoracolumbar spine FE model was utilized to investigate the biomechanical effect of one rigid and two types of SFTs on developing PJK. For the analysis, a modified multidirectional hybrid test protocol was used. First, a pure bending moment of 5 Nm was applied to measure the IVR angles. Second, the rigid technique's displacement from the first loading step was applied to the instrumented FE models to compare the pedicle screw stress values in the UIV. The FE analysis has shown that the SFTs increase the mobility at the upper instrumented segment and, therefore, provide a more gradual transition in motion between the instrumented and cranial non-instrumented spine segments. In addition, SFTs decrease the screw loads at the UIV level and hence could help reduce the risk for PJK.

In Part III, the validated pelvis FE model was used to evaluate and compare the biomechanical efficacy of six ISS fixation techniques for treating unilateral Denis Type II sacral fractures using literature-based (LBM) and QCT-based bone material properties (PSM) in FE models. The results demonstrated that all investigated techniques demonstrated clinically sufficient stability, with TISS12 being superior from a biomechanical standpoint. Both LBM and PSM models indicated a consistent trend in ranking the fixation techniques based on stability.

In Part IV, the lumbar part of the literature-based thoracolumbar spine and the pelvis FE model were combined to evaluate and compare the biomechanical characteristics of four LPRTs while considering the effect of LPDR. Based on the findings, LPDR significantly improved both lumbopelvic stability and implant safety in all reconstruction techniques after total sacrectomy. However, all four investigated LPRTs demonstrated suitability for lumbopelvic reconstruction, with the ICR technique exhibiting the highest lumbopelvic stiffness.

8. REFERENCES

1. Danchin A. In vivo, in vitro and in silico: an open space for the development of microbe-based applications of synthetic biology. Microb Biotechnol. 2022;15(1):42–64.
2. Pappalardo F, Russo G, Tshinanu FM, Viceconti M. In silico clinical trials: Concepts and early adoptions. Brief Bioinform. 2019;20(5):1699–1708.
3. Viceconti M. Biomechanics-based in silico medicine: The manifesto of a new science. J Biomech. 2015;48(2):193–194.
4. Brekelmans WAM, Poort HW, Slooff TJJH. A new method to analyse the mechanical behaviour of skeletal parts. Acta Orthop. 1972;43(5):301–317.
5. Fagan MJ, Julian S, Mohsen AM. Finite element analysis in spine research. Proc Inst Mech Eng H. 2002;216(5):281–298.
6. Schmidt H, Galbusera F, Rohlmann A, Shirazi-Adl A. What have we learned from finite element model studies of lumbar intervertebral discs in the past four decades? J Biomech. 2013;46(14):2342–2355.
7. Dreischarf M, Zander T, Shirazi-Adl A, Puttlitz CM, Adam CJ, Chen CS, Goel VK, Kiapour A, Kim YH, Labus KM, Little JP, Park WM, Wang YH, Wilke HJ, Rohlmann A, Schmidt H. Comparison of eight published static finite element models of the intact lumbar spine: Predictive power of models improves when combined together. J Biomech. 2014;47(8):1757–1766.
8. Little JP, Adam CJ. Geometric sensitivity of patient-specific finite element models of the spine to variability in user-selected anatomical landmarks. Comput Methods Biomech Biomed Engin. 2015;18(6):676–688.
9. Viceconti M, Pappalardo F, Rodriguez B, Horner M, Bischoff J, Musuamba Tshinanu F. In silico trials: Verification, validation and uncertainty quantification of predictive models used in the regulatory evaluation of biomedical products. Methods. 2021;185:120–127.
10. Viceconti M, Henney A, Morley-Fletcher E. In silico clinical trials: how computer simulation will transform the biomedical industry. Int J Clin Trials. 2016;3(2):37–46.

11. La Barbera L, Larson AN, Rawlinson J, Aubin CE. In silico patient-specific optimization of correction strategies for thoracic adolescent idiopathic scoliosis. Clinical Biomechanics. 2021;81.
12. Agarwal A, Agarwal AK, Jayaswal A, Goel VK. Outcomes of Optimal Distraction Forces and Frequencies in Growth Rod Surgery for Different Types of Scoliotic Curves: An In Silico and In vitro Study. Spine Deform. 2017;5(1):18–26.
13. Vergari C, Gaume M, Persohn S, Miladi L, Skalli W. From in vitro evaluation of a finite element model of the spine to in silico comparison of spine instrumentations. J Mech Behav Biomed Mater. 2021;123.
14. Costa MC, Eltes P, Lazary A, Varga PP, Viceconti M, Dall'Ara E. Biomechanical assessment of vertebrae with lytic metastases with subject-specific finite element models. J Mech Behav Biomed Mater. 2019;98:268–290.
15. Xiao Z, Wang L, Gong H, Zhu D, Zhang H. A non-linear finite element model of human L4-L5 lumbar spinal segment with three-dimensional solid element ligaments. Theoretical and Applied Mechanics Letters. 2011;1(6).
16. Faulkner KG, Cann CE, Hasegawa BH. Effect of bone distribution on vertebral strength: Assessment with patient-specific nonlinear finite element analysis. Radiology. 1991;179(3):669–674.
17. Crawford RP, Cann CE, Keaveny TM. Finite element models predict in vitro vertebral body compressive strength better than quantitative computed tomography. Bone. 2003;33(4):744–750.
18. Groenen KHJ, Bitter T, van Veluwen TCG, van der Linden YM, Verdonschot N, Tanck E, Janssen D. Case-specific non-linear finite element models to predict failure behavior in two functional spinal units. Journal of Orthopaedic Research. 2018;36(12):3208–3218.
19. O'Reilly MA, Whyne CM. Comparison of computed tomography based parametric and patient-specific finite element models of the healthy and metastatic spine using a mesh-morphing algorithm. Spine (Phila Pa 1976). 2008;33(17):1876–1881.
20. Sapin-De Brosses E, Jolivet E, Travert C, Mitton D, Skalli W. Prediction of the vertebral strength using a finite element model derived from low-dose biplanar

imaging: Benefits of subject-specific material properties. Spine (Phila Pa 1976). 2012;37(3):E156–E162.

21. Wall J, Wynne E, Krummel T. Biodesign process and culture to enable pediatric medical technology innovation. Semin Pediatr Surg. 2015;24(3):102–106.
22. Good CR, Auerbach JD, O'Leary PT, Schuler TC. Adult spine deformity. Curr Rev Musculoskelet Med. 2011;4(4):159–167.
23. DeWald CJ, Stanley T. Instrumentation-related complications of multilevel fusions for adult spinal deformity patients over age 65: Surgical considerations and treatment options in patients with poor bone quality. Spine . 2006;31(19 SUPPL.):S144–S151.
24. Glattes RC, Bridwell KH, Lenke LG, Kim YJ, Rinella A, Edwards II C. Proximal junctional kyphosis in adult spinal deformity following long instrumented posterior spinal fusion: Incidence, outcomes, and risk factor analysis. Spine . 2005;30(14):1643–1649.
25. Annis P, Lawrence BD, Spiker WR, Zhang Y, Chen W, Daubs MD. Predictive factors for acute proximal junctional failure after adult deformity surgery with upper instrumented vertebrae in the thoracolumbar spine. Evid Based Spine Care J. 2014;5(2):160–162.
26. Kim JS, Phan K, Cheung ZB, Lee N, Vargas L, Arvind V, Merrill RK, Gidumal S, Di Capua J, Overley S, Dowdell J, Cho SK. Surgical, Radiographic, and Patient-Related Risk Factors for Proximal Junctional Kyphosis: A Meta-Analysis. Global Spine J. 2019;9(1):32–40.
27. Kim HJ, Bridwell KH, Lenke LG, Park MS, Song KS, Piyaskulkaew C, Chuntarapas T. Patients with proximal junctional kyphosis requiring revision surgery have higher postoperative lumbar lordosis and larger sagittal balance corrections. Spine . 2014;39(9):E576–E580.
28. Sun X, Sun W, Sun S, Hu H, Zhang S, Kong C, Lu S. Which sagittal evaluation system can effectively predict mechanical complications in the treatment of elderly patients with adult degenerative scoliosis? Roussouly classification or Global Alignment and Proportion (GAP) Score. J Orthop Surg Res. 2021;16(1).

29. Bylski-Austrow DI, Glos DL, Bonifas AC, Carvalho MF, Coombs MC, Sturm PF. Flexible growing rods: A biomechanical pilot study of polymer rod constructs in the stability of skeletally immature spines. Scoliosis Spinal Disord. 2016;11(1).
30. Thawrani DP, Glos DL, Coombs MT, Bylski-Austrow DI, Sturm PF. Transverse process hooks at upper instrumented vertebra provide more gradual motion transition than pedicle screws. Spine . 2014;39(14):E826–E832.
31. Cahill PJ, Wang W, Asghar J, Booker R, Betz RR, Ramsey C, Baran G. The use of a transition rod may prevent proximal junctional kyphosis in the thoracic spine after scoliosis surgery: A finite element analysis. Spine . 2012;37(12):E687–E695.
32. Gornet MF, Chan FW, Coleman JC, Murrell B, Nockels RP, Taylor BA, Lanman TH, Ochoa JA. Biomechanical assessment of a PEEK rod system for semi-rigid fixation of lumbar fusion constructs. J Biomech Eng. 2011;133(8).
33. Doodkorte RJP, Roth AK, Arts JJ, Lataster LMA, van Rhijn LW, Willems PC. Biomechanical comparison of semirigid junctional fixation techniques to prevent proximal junctional failure after thoracolumbar adult spinal deformity correction. Spine Journal. 2021;21(5):855–864.
34. Viswanathan VK, Ganguly R, Minnema AJ, DeVries Watson NA, Grosland NM, Fredericks DC, Grossbach AJ, Viljoen S V, Francis Farhadi H. Biomechanical assessment of proximal junctional semi-rigid fixation in long-segment thoracolumbar constructs. J Neurosurg Spine. 2018;30(2):184–192.
35. Bess S, Harris JE, Turner AWL, LaFage V, Smith JS, Shaffrey CI, Schwab FJ, Haid Jr. RW. The effect of posterior polyester tethers on the biomechanics of proximal junctional kyphosis: A finite element analysis. J Neurosurg Spine. 2017;26(1):125–133.
36. Zhang M, Ren W, Mo Z, Li J, Pu F, Fan Y. Biomechanics of adjacent segment after three-level lumbar fusion, hybrid single-level semi-rigid fixation with two-level lumbar fusion. Comput Methods Biomech Biomed Engin. 2022;25(4):455–463.
37. Farkas J, Varga PP. Set of surgical instruments for the fixation of vertebrae. World Intellectual Property Organisation; 2002.
38. Beckmann NM, Chinapuvvula NR. Sacral fractures: classification and management. Emerg Radiol. 2017;24(6):605–617.

39. Yi C, Hak DJ. Traumatic spinopelvic dissociation or U-shaped sacral fracture: A review of the literature. Injury. 2012;43(4):402–408.
40. Nonne D, Capone A, Sanna F, Busnelli L, Russo AL, Marongiu G, Dessì G, Ferreli A. Suicidal jumper's fracture - Sacral fractures and spinopelvic instability: A case series. J Med Case Rep. 2018;12(1).
41. Santolini E, Kanakaris NK, Giannoudis P V. Sacral fractures: Issues, challenges, solutions. EFORT Open Rev. 2020;5(5):299–311.
42. Bydon M, De la Garza-Ramos R, Macki M, Abt NB, Sciubba DM, Wolinsky JP. Incidence of sacral fractures and in-hospital postoperative complications in the United States: an Analysis from 2002 to 2011. J Am Coll Surg. 2014;219:S67.
43. Peng Y, Zhang G, Zhang S, Ji X, Li J, Du C, Zhao W, Zhang L. Biomechanical study of transsacral-transiliac screw fixation versus lumbopelvic fixation and bilateral triangular fixation for "H"- and "U"-type sacrum fractures with traumatic spondylopelvic dissociation: a finite element analysis study. J Orthop Surg Res. 2021;16(1):428.
44. Reilly MC, Bono CM, Litkouhi B, Sirkin M, Behrens FF. The effect of sacral fracture malreduction on the safe placement of iliosacral screws. J Orthop Trauma. 2003;17(2):88–94.
45. Pohlemann T, Angst M, Schneider E, Ganz R, Tscherne H. Fixation of transforaminal sacrum fractures: A biomechanical study. J Orthop Trauma. 1993;7(2):107–117.
46. Dienstknecht T, Berner A, Lenich A, Nerlich M, Fuechtmeier B. A minimally invasive stabilizing system for dorsal pelvic ring injuries. Clin Orthop Relat Res. 2011;469(11):3209–3217.
47. Tian W, Chen WH, Jia J. Traumatic Spino-pelvic Dissociation with Bilateral Triangular Fixation. Orthop Surg. 2018;10(3):205–211.
48. Acklin YP, Zderic I, Richards RG, Schmitz P, Gueorguiev B, Grechenig S. Biomechanical investigation of four different fixation techniques in sacrum Denis type II fracture with low bone mineral density. Journal of Orthopaedic Research. 2018;36(6):1624–1629.

49. Chang TL, Sponseller PD, Kebaish KM, Fishman EK. Low profile pelvic fixation: Anatomic parameters for sacral alar-iliac fixation versus traditional iliac fixation. Spine (Phila Pa 1976). 2009;34(5):436–440.
50. Hoernschemeyer DG, Pashuck TD, Pfeiffer FM. Analysis of the s2 alar-iliac screw as compared with the traditional iliac screw: does it increase stability with sacroiliac fixation of the spine? Spine Journal. 2017;17(6):875–879.
51. König MA, Sundaram RO, Saville P, Jehan S, Boszczyk BM. Anatomical considerations for percutaneous trans ilio-sacroiliac S1 and S2 screw placement. European Spine Journal. 2016;25(6):1800–1805.
52. Bellabarba C. Treatment of B2 Transalar fracture with ISS fixation.
53. Miller AN, Routt Jr. MLC. Variations in sacral morphology and implications for iliosacral screw fixation. Journal of the American Academy of Orthopaedic Surgeons. 2012;20(1):8–16.
54. Zhao Y, Zhang S, Sun T, Wang D, Lian W, Tan J, Zou D, Zhao Y. Mechanical comparison between lengthened and short sacroiliac screws in sacral fracture fixation: A finite element analysis. Orthopaedics and Traumatology: Surgery and Research. 2013;99(5):601–606.
55. Fu S, Zhao Y, Lian W, Zou D, Sun T, Zhao Y, Tan J, Zhang S, Wang D. Comparison of the risk of breakage of two kinds of sacroiliac screws in the treatment of bilateral sacral fractures. European Spine Journal. 2014;23(7):1558–1567.
56. Zhao Y, Li J, Wang D, Liu Y, Tan J, Zhang S. Comparison of stability of two kinds of sacro-iliac screws in the fixation of bilateral sacral fractures in a finite element model. Injury. 2012;43(4):490–494.
57. Zheng J, Feng X, Xiang J, Liu F, Leung FKL, Chen B. S2-alar-iliac screw and S1 pedicle screw fixation for the treatment of non-osteoporotic sacral fractures: a finite element study. J Orthop Surg Res. 2021;16(1).
58. Dilogo IH, Satria O, Fiolin J. Internal fixation of S1-S3 iliosacral screws and pubic screw as the best configuration for unstable pelvic fracture with unilateral vertical sacral fracture (AO type C1.3): A biomechanical study. Journal of Orthopaedic Surgery. 2017;25(1).

59. Hu P, Wu T, Wang HZ, Qi XZ, Yao J, Cheng XD, Chen W, Zhang YZ. Biomechanical Comparison of Three Internal Fixation Techniques for Stabilizing Posterior Pelvic Ring Disruption: A 3D Finite Element Analysis. Orthop Surg. 2019;11(2):195–203.
60. Futamura K, Baba T, Mogami A, Morohashi I, Obayashi O, Iwase H, Kaneko K. A biomechanical study of sacroiliac rod fixation for unstable pelvic ring injuries: verification of the "within ring" concept. Int Orthop. 2018;42(4):909–914.
61. Gierig M, Liu F, Weiser L, Lehmann W, Wriggers P, Marino M, Saul D. Biomechanical Effects of a Cross Connector in Sacral Fractures – A Finite Element Analysis. Front Bioeng Biotechnol. 2021;9.
62. Radley JM, Hill BW, Nicolaou DA, Huebner SB, Napier KB, Salazar DH. Bone density of first and second segments of normal and dysmorphic sacra. Journal of Orthopaedics and Traumatology. 2020;21(1).
63. Turbucz M, Pokorni AJ, Szőke G, Hoffer Z, Kiss RM, Lazary A, Eltes PE. Development and Validation of Two Intact Lumbar Spine Finite Element Models for In Silico Investigations: Comparison of the Bone Modelling Approaches. Applied Sciences (Switzerland). 2022;12(20).
64. Cheng JS, Song JK. Anatomy of the sacrum. Neurosurg Focus. 2003;15(2).
65. Varga PP. Spinopelvic Reconstruction/Fixation and Fusion. In: Vialle LR, Fisher CG, Gokaslan ZL, Boriani S, editors. AOSpine Master Series - Primary Spinal Tumors. 1st ed. Stuttgart: Georg Thieme Verlag KG; 2015. p. 147–156.
66. Choudry UH, Moran SL, Karacor Z. Functional reconstruction of the pelvic ring with simultaneous bilateral free fibular flaps following total sacral resection. Ann Plast Surg. 2006;57(6):673–676.
67. Varga PP, Bors I, Lazary A. Sacral Tumors and Management. Orthopedic Clinics of North America. 2009;40(1):105–123.
68. Bederman SS, Shah KN, Hassan JM, Hoang BH, Kiester PD, Bhatia NN. Surgical techniques for spinopelvic reconstruction following total sacrectomy: A systematic review. European Spine Journal. 2014;23(2):305–319.
69. Sciubba DM, Petteys RJ, Garces-Ambrossi GL, Noggle JC, McGirt MJ, Wolinsky JP, Witham TF, Gokaslan ZL. Diagnosis and management of sacral tumors: A review. J Neurosurg Spine. 2009;10(3):244–256.

70. Varga PP, Szoverfi Z, Lazary A. Surgical resection and reconstruction after resection of tumors involving the sacropelvic region. Neurol Res. 2014;36(6):588–596.
71. Shikata J, Yamamuro T, Kotoura Y, Mikawa Y, Iida H, Maetani S. Total sacrectomy and reconstrucion for primary tumors. Report of two cases. Journal of Bone and Joint Surgery - Series A. 1988;70(1):122–125.
72. Yamamoto Y, Takeda N, Sugihara T. Pelvic ring reconstruction with a vascularized bone flap of femur. Plast Reconstr Surg. 1997;100(2):415–417.
73. Tomita K, Tsuchiya H. Total sacrectomy and reconstruction for huge sacral tumors. Spine (Phila Pa 1976). 1990;15(11):1223–1227.
74. Zhu R, Cheng LM, Yu Y, Zander T, Chen B, Rohlmann A. Comparison of four reconstruction methods after total sacrectomy: A finite element study. Clinical Biomechanics. 2012;27(8):771–776.
75. Allen Jr. BL, Ferguson RL. The galveston technique for L rod instrumentation of the scoliotic spine. Spine (Phila Pa 1976). 1982;7(3):276–284.
76. Murakami H, Kawahara N, Tomita K, Sakamoto J, Oda J. Biomechanical evaluation of reconstructed lumbosacral spine after total sacrectomy. Journal of Orthopaedic Science. 2002;7(6):658–664.
77. Dickey ID, Rugate Jr. RR, Fuchs B, Yaszemski MJ, Sim FH. Reconstruction after total sacrectomy: Early experience with a new surgical technique. Clin Orthop Relat Res. 2005;438:42–50.
78. Shen FH, Harper M, Foster WC, Marks I, Arlet V. A novel “four-rod technique” for lumbo-pelvic reconstruction: Theory and technical considerations. Spine (Phila Pa 1976). 2006;31(12):1395–1401.
79. Gokaslan ZL, Romsdahl MM, Kroll SS, Walsh GL, Gillis TA, Wildrick DM, Leavens ME. Total sacrectomy and Galveston L-rod reconstruction for malignant neoplasms: Technical note. J Neurosurg. 1997;87(5):781–787.
80. Guo W, Tang X, Zang J, Ji T. One-stage total en bloc sacrectomy: A novel technique and report of 9 cases. Spine (Phila Pa 1976). 2013;38(10):E626–E631.
81. Zhang HY, Thongtrangan I, Balabhadra RS, Murovic JA, Kim DH. Surgical techniques for total sacrectomy and spinopelvic reconstruction. Neurosurg Focus. 2003;15(2).

82. Kawahara N, Murakami H, Yoshida A, Sakamoto J, Oda J, Tomita K. Reconstruction after total sacrectomy using a new instrumentation technique: A biomechanical comparison. Spine (Phila Pa 1976). 2003;28(14):1567–1572.
83. Cheng L, Yu Y, Zhu R, Lv H, Jia Y, Zeng Z, Chen B, Ding Z. Structural stability of different reconstruction techniques following total sacrectomy: A biomechanical study. Clinical Biomechanics. 2011;26(10):977–981.
84. Kelly BP, Shen FH, Schwab JS, Arlet V, Diangelo DJ. Biomechanical testing of a novel four-rod technique for lumbo-pelvic reconstruction. Spine (Phila Pa 1976). 2008;33(13):E400–E406.
85. Macki M, De La Garza-Ramos R, Murgatroyd AA, Mullinix KP, Sun X, Cunningham BW, McCutcheon BA, Bydon M, Gokaslan ZL. Comprehensive biomechanical analysis of three reconstruction techniques following total sacrectomy: An in vitro human cadaveric model. J Neurosurg Spine. 2017;27(5):570–577.
86. Huang S, Ji T, Guo W. Biomechanical comparison of a 3D-printed sacrum prosthesis versus rod-screw systems for reconstruction after total sacrectomy: A finite element analysis. Clinical Biomechanics. 2019;70:203–208.
87. Yu Y, Zhu R, Zeng ZL, Jia YW, Wu ZR, Ren YL, Chen B, Ding ZQ, Cheng LM. The strain at bone-implant interface determines the effect of spinopelvic reconstruction following total sacrectomy: A strain gauge analysis in various spinopelvic constructs. PLoS One. 2014;9(1).
88. Eltes PE, Turbucz M, Fayad J, Bereczki F, Szőke G, Terebessy T, Lacroix D, Varga PP, Lazary A. A Novel Three-Dimensional Computational Method to Assess Rod Contour Deformation and to Map Bony Fusion in a Lumbopelvic Reconstruction After En-Bloc Sacrectomy. Front Surg. 2022;8.
89. Lim SH, Jo DJ, Kim SM, Lim YJ. Reconstructive surgery using dual U-shaped rod instrumentation after posterior en bloc sacral hemiresection for metastatic tumor: Case report. J Neurosurg Spine. 2015;23(5):630–634.
90. Choi MK, Jo DJ, Kim SB. Pelvic Reconstruction Surgery Using a Dual-Rod Technique with Diverse U-Shaped Rods After Posterior En Bloc Partial Sacrectomy for a Sacral Tumor: 2 Case Reports and a Literature Review. World Neurosurg. 2016;95:619.e11.

91. Turbucz M, Fayad J, Pokorni AJ, Varga PP, Eltes PE, Lazary A. Can semirigid fixation of the rostral instrumented segments prevent proximal junctional kyphosis in the case of long thoracolumbar fusions? A finite element study. J Neurosurg Spine. 2023;38(6):662–672.
92. Van Rijsbergen M, Van Rietbergen B, Barthelemy V, Eltes P, Lazáry A, Lacroix D, Noailly J, Tho MCHB, Wilson W, Ito K. Comparison of patient-specific computational models vs. clinical follow-up, for adjacent segment disc degeneration and bone remodelling after spinal fusion. PLoS One. 2018;13(8).
93. Aryanto KYE, Oudkerk M, van Ooijen PMA. Free DICOM de-identification tools in clinical research: functioning and safety of patient privacy. Eur Radiol. 2015;25(12):3685–3695.
94. Bereczki F, Turbucz M, Kiss R, Eltes PE, Lazary A. Stability Evaluation of Different Oblique Lumbar Interbody Fusion Constructs in Normal and Osteoporotic Condition – A Finite Element Based Study. Front Bioeng Biotechnol. 2021;9.
95. Morgan EF, Bayraktar HH, Keaveny TM. Trabecular bone modulus-density relationships depend on anatomic site. J Biomech. 2003;36(7):897–904.
96. Tawara D, Sakamoto J, Murakami H, Kawahara N, Oda J, Tomita K. Mechanical evaluation by patient-specific finite element analyses demonstrates therapeutic effects for osteoporotic vertebrae. J Mech Behav Biomed Mater. 2010;3(1):31–40.
97. Nishiyama KK, Gilchrist S, Guy P, Cripton P, Boyd SK. Proximal femur bone strength estimated by a computationally fast finite element analysis in a sideways fall configuration. J Biomech. 2013;46(7):1231–1236.
98. Dragomir-Daescu D, Op Den Buijs J, McEligot S, Dai Y, Entwistle RC, Salas C, Melton III LJ, Bennet KE, Khosla S, Amin S. Robust QCT/FEA models of proximal femur stiffness and fracture load during a sideways fall on the hip. Ann Biomed Eng. 2011;39(2):742–755.
99. Schileo E, Dall'Ara E, Taddei F, Malandrino A, Schotkamp T, Baleani M, Viceconti M. An accurate estimation of bone density improves the accuracy of subject-specific finite element models. J Biomech. 2008;41(11):2483–2491.
100. Mills MJ, Sarigul-Klijn N. Validation of an in vivo medical image-based young human lumbar spine finite element model. J Biomech Eng. 2019;141(3).

101. Rezaei A, Carlson KD, Giambini H, Javid S, Dragomir-Daescu D. Optimizing Accuracy of Proximal Femur Elastic Modulus Equations. Ann Biomed Eng. 2019;
102. Zeng ZL, Zhu R, Wu YC, Zuo W, Yu Y, Wang JJ, Cheng LM. Effect of Graded Facetectomy on Lumbar Biomechanics. J Healthc Eng. 2017;2017.
103. Remus R, Lipphaus A, Neumann M, Bender B. Calibration and validation of a novel hybrid model of the lumbosacral spine in ArtiSynth—The passive structures. PLoS One. 2021;16(4 April).
104. Park WM, Kim K, Kim YH. Effects of degenerated intervertebral discs on intersegmental rotations, intradiscal pressures, and facet joint forces of the whole lumbar spine. Comput Biol Med. 2013;43(9):1234–1240.
105. White AA, Panjabi MM. Clinical Biomechanics of the Spine. Lippincott; 1990.
106. Noailly J, Wilke HJ, Planell JA, Lacroix D. How does the geometry affect the internal biomechanics of a lumbar spine bi-segment finite element model? Consequences on the validation process. J Biomech. 2007;40(11):2414–2425.
107. Rohlmann A, Burra NK, Zander T, Bergmann G. Comparison of the effects of bilateral posterior dynamic and rigid fixation devices on the loads in the lumbar spine: A finite element analysis. European Spine Journal. 2007;16(8):1223–1231.
108. Lu YM, Hutton WC, Gharpuray VM. Do bending, twisting, and diurnal fluid changes in the disc affect the propensity to prolapse? A viscoelastic finite element model. Spine (Phila Pa 1976). 1996;21(22):2570–2579.
109. Finley SM, Brodke DS, Spina NT, DeDen CA, Ellis BJ. FEBio finite element models of the human lumbar spine. Comput Methods Biomech Biomed Engin. 2018;21(6):444–452.
110. Schmidt H, Heuer F, Drumm J, Klezl Z, Claes L, Wilke HJ. Application of a calibration method provides more realistic results for a finite element model of a lumbar spinal segment. Clinical Biomechanics. 2007;22(4):377–384.
111. Schmidt H, Heuer F, Simon U, Kettler A, Rohlmann A, Claes L, Wilke HJ. Application of a new calibration method for a three-dimensional finite element model of a human lumbar annulus fibrosus. Clinical Biomechanics. 2006;21(4):337–344.
112. Lu Y, Rosenau E, Paetzold H, Klein A, Püschel K, Morlock MM, Huber G. Strain changes on the cortical shell of vertebral bodies due to spine ageing: A parametric

study using a finite element model evaluated by strain measurements. Proc Inst Mech Eng H. 2013;227(12):1265–1274.

113. Shirazi-Adl A, Ahmed AM. Mechanical response of a lumbar motion segment in axial torque alone and combined with compression. Spine (Phila Pa 1976). 1986;11(9):914–927.
114. Rohlmann A, Bauer L, Zander T, Bergmann G, Wilke HJ. Determination of trunk muscle forces for flexion and extension by using a validated finite element model of the lumbar spine and measured in vivo data. J Biomech. 2006;39(6):981–989.
115. Naserkhaki S, Arjmand N, Shirazi-Adl A, Farahmand F, El-Rich M. Effects of eight different ligament property datasets on biomechanics of a lumbar L4-L5 finite element model. J Biomech. 2018;70:33–42.
116. Wilke HJ, Wenger K, Claes L. Testing criteria for spinal implants: Recommendations for the standardization of in vitro stability testing of spinal implants. European Spine Journal. 1998;7(2):148–154.
117. Dreischarf M, Zander T, Bergmann G, Rohlmann A. A non-optimized follower load path may cause considerable intervertebral rotations. J Biomech. 2010;43(13):2625–2628.
118. Xu M, Yang J, Lieberman IH, Haddas R. Lumbar spine finite element model for healthy subjects: development and validation. Comput Methods Biomech Biomed Engin. 2017;20(1):1–15.
119. Pearcy MJ, Tibrewal SB. Axial rotation and lateral bending in the normal lumbar spine measured by three-dimensional radiography. Spine (Phila Pa 1976). 1984;9(6):582–587.
120. Pearcy MJ, Portek I, Shepherd J. Three-dimensional X-ray analysis of normal movement in the lumbar spine. Spine (Phila Pa 1976). 1984;9(3):294–297.
121. Pearcy MJ. Stereo radiography of lumbar spine motion. Acta Orthop Scand. 1985;56(SUPPL. 212).
122. Wilke HJ, Neef P, Hinz B, Seidel H, Claes L. Intradiscal pressure together with anthropometric data - A data set for the validation of models. Clinical Biomechanics. 2001;16(SUPPL. 1):S111–S126.

123. Rohlmann A, Neller S, Claes L, Bergmann G, Wilke HJ. Influence of a follower load on intradiscal pressure and intersegmental rotation of the lumbar spine. Spine (Phila Pa 1976). 2001;26(24):E557-561.
124. Wilson DC, Niosi CA, Zhu QA, Oxland TR, Wilson DR. Accuracy and repeatability of a new method for measuring facet loads in the lumbar spine. J Biomech. 2006;39(2):348–353.
125. Brinckmann P, Grootenboer H. Change of disc height, radial disc bulge, and intradiscal pressure from discectomy: An in vitro investigation on human lumbar discs. Spine (Phila Pa 1976). 1991;16(6):641–646.
126. Panjabi MM, Oxland TR, Yamamoto I, Crisco JJ. Mechanical behavior of the human lumbar and lumbosacral spine as shown by three-dimensional load-displacement curves. Journal of Bone and Joint Surgery. 1994;76(3):413–424.
127. Rohlmann A, Zander T, Rao M, Bergmann G. Realistic loading conditions for upper body bending. J Biomech. 2009;42(7):884–890.
128. Ayturk UM, Puttlitz CM. Parametric convergence sensitivity and validation of a finite element model of the human lumbar spine. Comput Methods Biomech Biomed Engin. 2011;14(8):695–705.
129. Cignoni P, Rocchini C, Scopigno R. Metro: Measuring Error on Simplified Surfaces. Computer Graphics Forum. 1998;17(2):167–174.
130. Baroud G, Nemes J, Heini P, Steffen T. Load shift of the intervertebral disc after a vertebroplasty: A finite-element study. European Spine Journal. 2003;12(4):421–426.
131. Shirazi-Adl SA, Shrivastava SC, Ahmed AM. Stress analysis of the lumbar disc-body unit in compression. A three-dimensional nonlinear finite element study. 1984;9(2):120–134.
132. Rohlmann A, Zander T, Schmidt H, Wilke HJ, Bergmann G. Analysis of the influence of disc degeneration on the mechanical behaviour of a lumbar motion segment using the finite element method. J Biomech. 2006;39(13):2484–2490.
133. Li J, Shang J, Zhou Y, Li C, Liu H. Finite Element Analysis of a New Pedicle Screw-Plate System for Minimally Invasive Transforaminal Lumbar Interbody Fusion. PLoS One. 2015 Dec 9;10(12).

134. Couvertier M, Germaneau A, Saget M, Dupré JC, Doumalin P, Brémand F, Hesser F, Brèque C, Roulaud M, Monlezun O, Vendeuvre T, Rigoard P. Biomechanical analysis of the thoracolumbar spine under physiological loadings: Experimental motion data corridors for validation of finite element models. Proc Inst Mech Eng H. 2017;231(10):975–981.
135. Wilke HJ, Herkommer A, Werner K, Liebsch C. In vitro analysis of the segmental flexibility of the thoracic spine. PLoS One. 2017;12(5).
136. Turbucz M, Pokorni AJ, Bigdon SF, Hajnal B, Koch K, Szoverfi Z, Lazary A, Eltes PE. Patient-specific bone material modelling can improve the predicted biomechanical outcomes of sacral fracture fixation techniques: A comparative finite element study. Injury. 2023;54(12).
137. Eichenseer PH, Sybert DR, Cotton JR. A finite element analysis of sacroiliac joint ligaments in response to different loading conditions. Spine (Phila Pa 1976). 2011;36(22):E1446–E1452.
138. McLauchlan GJ, Gardner DL. Sacral and iliac articular cartilage thickness and cellularity: Relationship to subchondral bone end-plate thickness and cancellous bone density. Rheumatology. 2002;41(4):375–380.
139. Dalstra M, Huiskes R, van Erning L. Development and validation of a three-dimensional finite element model of the pelvic bone. J Biomech Eng. 1995;117(3):272–278.
140. Gray H, Goss CM. Anatomy of the human body. Am J Phys Med Rehabil. 1974;53(6):293.
141. Phillips ATM, Pankaj P, Howie CR, Usmani AS, Simpson AHRW. Finite element modelling of the pelvis: Inclusion of muscular and ligamentous boundary conditions. Med Eng Phys. 2007;29(7):739–748.
142. Miller JAA, Schultz AB, Andersson GBJ. Load-displacement behavior of sacroiliac joints. Journal of Orthopaedic Research. 1987;5(1):92–101.
143. Xu Z, Li Y, Zhang S, Liao L, Wu K, Feng Z, Li D. A finite element analysis of sacroiliac joint displacements and ligament strains in response to three manipulations. BMC Musculoskelet Disord. 2020;21(1).

144. Kim YH, Yao Z, Kim K, Park WM. Quantitative investigation of ligament strains during physical tests for sacroiliac joint pain using finite element analysis. Man Ther. 2014;19(3):235–241.
145. Shirazi-Adl A. Analysis of role of bone compliance on mechanics of a lumbar motion segment. J Biomech Eng. 1994;116(4):408–412.
146. Panjabi MM. Hybrid multidirectional test method to evaluate spinal adjacent-level effects. Clinical Biomechanics. 2007;22(3):257–265.
147. Gänsslen A, Lindahl J, Grechenig S, Füchtmeier B. Pelvic Ring Fractures. Pelvic Ring Fractures. Springer International Publishing; 2020. 1–640 p.
148. Turbucz M, Pokorni AJ, Hajnal B, Koch K, Szoverfi Z, Varga PP, Lazary A, Eltes PE. The biomechanical effect of lumbopelvic distance reduction on reconstruction after total sacrectomy: a comparative finite element analysis of four techniques. Spine Journal. 2024;in press.
149. Viceconti M, Olsen S, Nolte LP, Burton K. Extracting clinically relevant data from finite element simulations. Clinical Biomechanics. 2005;20(5):451–454.
150. Patwardhan AG, Havey RM, Meade KP, Lee B, Dunlap B. A follower load increases the load-carrying capacity of the lumbar spine in compression. Spine (Phila Pa 1976). 1999;24(10):1003–1009.
151. Woldtvedt DJ, Womack W, Gadomski BC, Schuldt D, Puttlitz CM. Finite element lumbar spine facet contact parameter predictions are affected by the cartilage thickness distribution and initial joint gap size. J Biomech Eng. 2011;133(6).
152. Dreischarf M, Rohlmann A, Bergmann G, Zander T. Optimised loads for the simulation of axial rotation in the lumbar spine. J Biomech. 2011 Aug 11;44(12):2323–2327.
153. Dreischarf M, Rohlmann A, Bergmann G, Zander T. Optimised in vitro applicable loads for the simulation of lateral bending in the lumbar spine. Med Eng Phys. 2012 Jul 1;34(6):777–780.
154. Schmidt H, Heuer F, Claes L, Wilke HJ. The relation between the instantaneous center of rotation and facet joint forces – A finite element analysis. Clinical Biomechanics. 2008 Mar 1;23(3):270–278.

155. Karimi D, Salcudean SE. Reducing the Hausdorff Distance in Medical Image Segmentation with Convolutional Neural Networks. IEEE Trans Med Imaging. 2020;39(2):499–513.
156. DIebo BG, Jalai CM, Challier V, Marascalchi BJ, Horn SR, Poorman GW, Bono OJ, Cherkalin D, Worley N, Oh J, Naziri Q, Spitzer A, Radcliff K, Patel A, Lafage V, Paulino CB, Passias PG. Novel Index to Quantify the Risk of Surgery in the Setting of Adult Spinal Deformity: A Study on 10,912 Patients from the Nationwide Inpatient Sample. Clin Spine Surg. 2017;30(7):E993–E999.
157. Kim DK, Kim JY, Kim DY, Rhim SC, Yoon SH. Risk factors of proximal junctional kyphosis after multilevel fusion surgery: More than 2 years follow-up data. J Korean Neurosurg Soc. 2017;60(2):174–180.
158. Park SJ, Lee CS, Chung SS, Lee JY, Kang SS, Park SH. Different risk factors of proximal junctional kyphosis and proximal junctional failure following long instrumented fusion to the sacrum for adult spinal deformity: Survivorship analysis of 160 patients. Neurosurgery. 2017;80(2):279–286.
159. Kim YJ, Bridwell KH, Lenke LG, Kim J, Cho SK. Proximal junctional kyphosis in adolescent idiopathic scoliosis following segmental posterior spinal instrumentation and fusion: Minimum 5-year follow-up. Spine (Phila Pa 1976). 2005;30(18):2045–2050.
160. Pereira B de A, Lehrman JN, Sawa AGU, Wangsawatwong P, Godzik J, Xu DS, Turner JD, Kelly BP, Uribe JS. Biomechanical Effects of Proximal Polyetheretherketone Rod Extension on the Upper Instrumented and Adjacent Levels in a Human Long-Segment Construct: A Cadaveric Model. Neurospine. 2022 Sep 30;19(3):828–837.
161. Moshirfar A, Rand FF, Sponseller PD, Parazin SJ, Jay Khanna A, Kebaish KM, Stinson JT, Riley III LH. Pelvic fixation in spine surgery. Historical overview, indications, biomechanical relevance, and current techniques. Journal of Bone and Joint Surgery. 2005;87(12 II SUPPL.):89–106.
162. Synek A, Chevalier Y, Baumbach SF, Pahr DH. The influence of bone density and anisotropy in finite element models of distal radius fracture osteosynthesis: Evaluations and comparison to experiments. J Biomech. 2015;48(15):4116–4123.

163. Claes LE, Heigele CA. Magnitudes of local stress and strain along bony surfaces predict the course and type of fracture healing. J Biomech. 1999;32(3):255–266.
164. Clark AJ, Tang JA, Leasure JM, Ivan ME, Kondrashov D, Buckley JM, Deviren V, Ames CP. Gait-simulating fatigue loading analysis and sagittal alignment failure of spinal pelvic reconstruction after total sacrectomy: Comparison of 3 techniques: Laboratory investigation. J Neurosurg Spine. 2014;20(4):364–370.
165. Yu BS, Zhuang XM, Zheng ZM, Li ZM, Wang TP, Lu WW. Biomechanical advantages of dual over single iliac screws in lumbo-iliac fixation construct. European Spine Journal. 2010;19(7):1121–1128.
166. Yu BS, Zhuang XM, Li ZM, Zheng ZM, Zhou ZY, Zou XN, Lu WW. Biomechanical effects of the extent of sacrectomy on the stability of lumbo-iliac reconstruction using iliac screw techniques: What level of sacrectomy requires the bilateral dual iliac screw technique? Clinical Biomechanics. 2010;25(9):867–872.
167. Sakamoto J, Oda J, Kakuuchi A, Akamaru T, Kawahara N, Tomita K. A study of mechanical evaluation of reconstruction method after total en bloc spondylectomy. Nippon Kikai Gakkai Ronbunshu, A Hen/Transactions of the Japan Society of Mechanical Engineers, Part A. 2003;69(1):128–134.
168. Zheng L, Li Z, Li Q, Ji F, Cai Z. Finite element analysis of lumbosacral reconstruction after partial sacrectomy. Medical Science Monitor. 2014;20:889–893.
169. Mirzaali MJ, Schwiedrzik JJ, Thaiwichai S, Best JP, Michler J, Zysset PK, Wolfram U. Mechanical properties of cortical bone and their relationships with age, gender, composition and microindentation properties in the elderly. Bone. 2016;93:196–211.
170. Morgan EF, Unnikrisnan GU, Hussein AI. Bone Mechanical Properties in Healthy and Diseased States. Annu Rev Biomed Eng. 2018;20:119–143.
171. Morales-Codina AM, Martín-Benlloch JA. Sacral Prosthesis Substitution as a System of Spinopelvic Reconstruction after Total Sacrectomy: Assessment Using the Finite Element Method. Int J Spine Surg. 2022;16(3):512–520.
172. Bydon M, De La Garza-Ramos R, Gokaslan ZL. Editorial: Total sacrectomy for malignant sacral tumors via a posterior-only approach. J Neurosurg Spine. 2015;22(6):561–562.

173. Shin JK, Lim BY, Goh TS, Son SM, Kim HS, Lee JS, Lee CS. Effect of the screw type (S2-alar-iliac and iliac), screw length, and screw head angle on the risk of screw and adjacent bone failures after a spinopelvic fixation technique: A finite element analysis. PLoS One. 2018;13(8).

9. BIBLIOGRAPHY OF THE CANDIDATE'S PUBLICATIONS

9.1. Publications that formed the basis of the dissertation

1. **Turbucz M**, Pokorni AJ, Szőke G, Hoffer Z, Kiss RM, Lazary A, Eltes PE. Development and Validation of Two Intact Lumbar Spine Finite Element Models for In Silico Investigations: Comparison of the Bone Modelling Approaches. Applied Sciences (Switzerland). 2022;12(20).

2. **Turbucz M**, Fayad J, Pokorni AJ, Varga PP, Eltes PE, Lazary A. Can semirigid fixation of the rostral instrumented segments prevent proximal junctional kyphosis in the case of long thoracolumbar fusions? A finite element study. J Neurosurg Spine. 2023;38(6):662–672.

3. **Turbucz M**, Pokorni AJ, Bigdon SF, Hajnal B, Koch K, Szoverfi Z, Lazary A, Eltes PE. Patient-specific bone material modelling can improve the predicted biomechanical outcomes of sacral fracture fixation techniques: A comparative finite element study. Injury. 2023;54(12).

4. **Turbucz M**, Pokorni AJ, Hajnal B, Koch K, Szoverfi Z, Varga PP, Lazary A, Eltes PE. The biomechanical effect of lumbopelvic distance reduction on reconstruction after total sacrectomy: a comparative finite element analysis of four techniques. Spine Journal. 2024;in press.

9.2. Publication in the field of in silico medicine as co author

1. Bereczki F, **Turbucz M**, Kiss R, Eltes PE, Lazary A. Stability Evaluation of Different Oblique Lumbar Interbody Fusion Constructs in Normal and Osteoporotic Condition – A Finite Element Based Study. Front Bioeng Biotechnol. 2021;9.

2. Eltes PE, **Turbucz M**, Fayad J, Bereczki F, Szőke G, Terebessy T, Lacroix D, Varga PP, Lazary A. A Novel Three-Dimensional Computational Method to Assess Rod Contour Deformation and to Map Bony Fusion in a Lumbopelvic Reconstruction After En-Bloc Sacrectomy. Front Surg. 2022;8.

3. Hajnal B, Eltes PE, Bereczki F, **Turbucz M**, Fayad J, Pokorni AJ, Lazary A. New method to apply the lumbar lordosis of standing radiographs to supine CT-based virtual 3D lumbar spine models. Sci Rep. 2022;12(1).

4. Pokorni AJ, **Turbucz M**, Kiss RM, Eltes PE, Lazary A. Comparison of anterior column reconstruction techniques after en bloc spondylectomy: a finite element study. Sci Rep. 2023;13(1).

5. Bereczki F, **Turbucz M**, Pokorni AJ, Hajnal B, Rónai M, Klemencsics I, Lazary A, Eltes PE. The effect of polymethylmethacrylate augmentation on the primary stability of stand-alone implant construct versus posterior stabilization in oblique lumbar interbody fusion with osteoporotic bone quality– a finite element study. The Spine Journal. 2024.

9.3 Publication in the field of spine surgery as co author

1. Fayad J, **Turbucz M**, Hajnal B, Bereczki F, Bartos M, Bank A, Lazary A, Eltes PE. Complicated Postoperative Flat Back Deformity Correction With the Aid of Virtual and 3D Printed Anatomical Models: Case Report. Front Surg. 2021;8.

9.4 Patents in the field of spine surgery as co-inventor

1. Eltes P, Lazary A, **Turbucz M**, Varga PP. Set Of Surgical Instruments For The Fixation Of Vertebrae, U2200053, 2022.09.19

10. ACKNOWLEDGEMENTS

I am deeply grateful to my co-supervisor, Péter Endre Éltes, for his mentorship and for providing me the opportunity to work in the newly established In Silico Biomechanics Laboratory in 2018. His unwavering support, patience, and willingness to discuss my ideas and address my concerns have been remarkable and have ensured the successful completion of this thesis.

I am also thankful to my other co-supervisor, Áron Lazáry, the head of the R&D department at the National Center for Spinal Disorders, for his guidance and support during my doctoral program.

I would like to express my sincere appreciation to my colleagues at the In Silico Biomechanics Laboratory, Benjamin Hajnal, Ferenc Bereczki, Márton Bartos, and distinguished to Ágoston Jakab Pokorni for their constant support, inspiring discussions, and contributions to the pleasant working atmosphere.

To all my colleagues at the R&D Department of the National Center for Spinal Disorders, especially Julia Szita, your collaboration has been invaluable throughout this journey.

I am thankful to János Gyurka, my former high school headmaster, whose guidance towards natural sciences was crucial to starting my academic journey.

My entire family, including my parents and siblings, deserves my gratitude for their unwavering support and encouragement.

I want to express my heartfelt appreciation to my beloved wife, Kinga. Without her steadfast support, this work would not have been possible. She alone understands the dedication, frustration, and joy behind every line of this thesis.

Finally, I would like to dedicate this PhD thesis to my late sister Virág, who always showed genuine interest in my research. Sadly, she never had the chance to see this work.

Thank you all for your contributions, encouragement, and belief in me.

APPENDIX

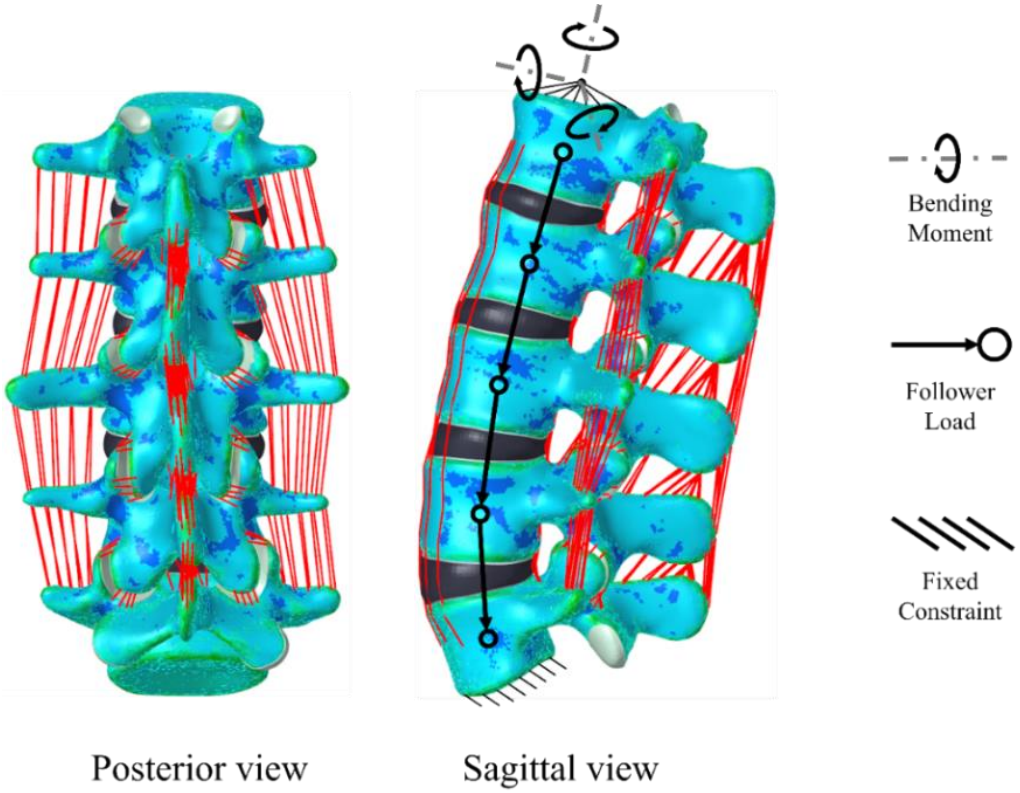

Supplementary Figure 1. FE model of the patient-specific lumbar spine with the applied loads and constraints.

Supplementary Table 1. Applied material properties of the pelvic ligaments.

Ligament	K (N/mm)	Number of elements	Reference
Arcuate Pubic Ligament	500	10	Li et al. 2015
Superior Pubic Ligament	500	10	Li et al. 2015
Long Posterior Sacroiliac Ligament	1400	10	Zhao et al. 2012
Short Posterior Sacroiliac Ligament	1400	34	Zhao et al. 2012
Interosseous Sacroiliac Ligament	2800	44	Zhao et al. 2012
Anterior Sacroiliac Ligament	700	24	Zhao et al. 2012
Sacrotuberous Ligament	1500	20	Zhao et al. 2012
Sacrospinous Ligament	1400	26	Zhao et al. 2012

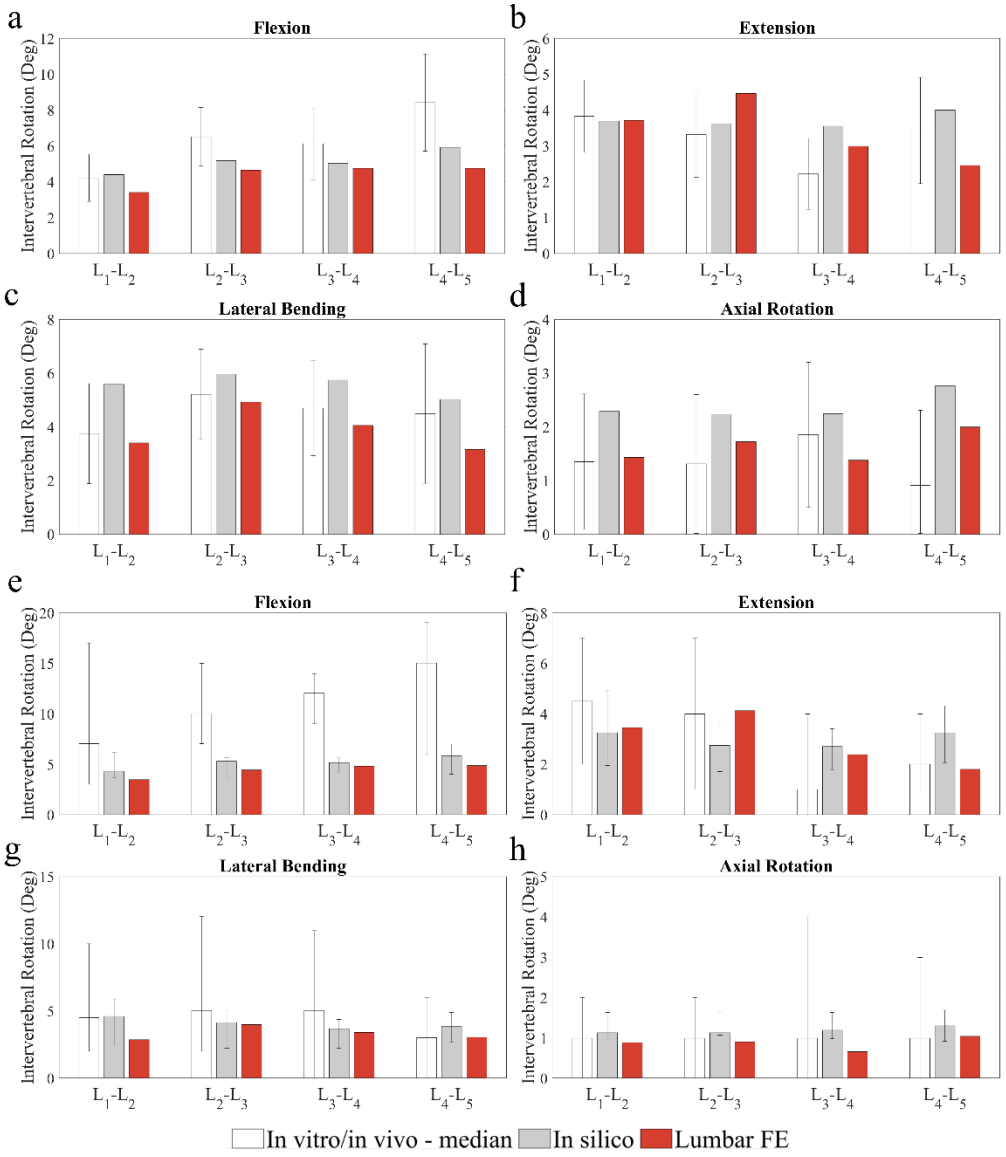

Supplementary Figure 2. IVR results of the lumbar spine FE model at different spinal levels (with red colour). (a) Pure bending of 7.5 Nm in flexion, (b) extension, (c) lateral bending and (d) axial rotation. The white bars and their range correspond to the median, minimum and maximum values of an in vitro measurement (Panjabi et al. 1994). The grey bars and their range correspond to the median and range of results of a calibrated FE simulation (Remus et al. 2021). (e) IVR results of lumbar spine FE model at different spinal levels against combined loads in flexion, (f) extension, (g) lateral bending, and (h) axial rotation. The white bars and their range correspond to the median, minimum, and maximum values of multiple in vivo measurements (Pearcy 1985, Pearcy et al. 1984, Pearcy et al. 1985). The grey bars and their range correspond to the median and range of multiple validated FE model results (Dreischarf et al. 2014).

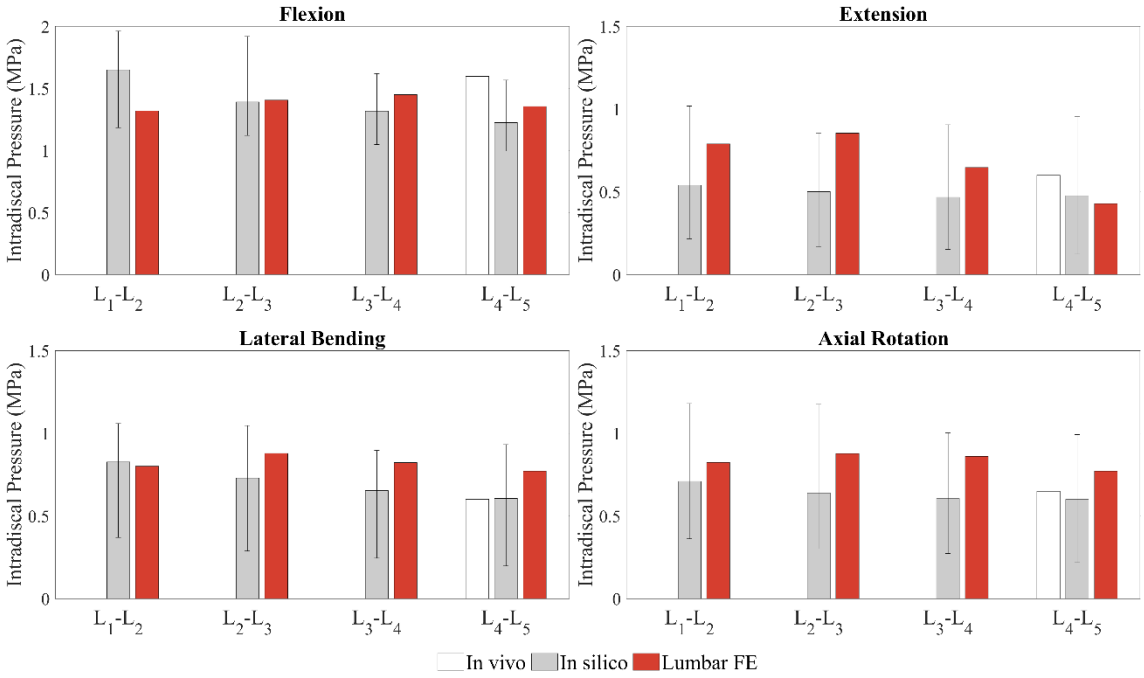

Supplementary Figure 3. Predicted IDP values of the lumbar spine FE model at different spinal levels for combined loads (with red colour) in (a) flexion, (b) extension, (c) lateral bending, and (d) axial rotation. The white bars correspond to the median values of an in vivo measurement (Wilke et al. 2001). The grey bars and their range illustrate the median and range of multiple validated and published FE model results (Dreischarf et al. 2014).

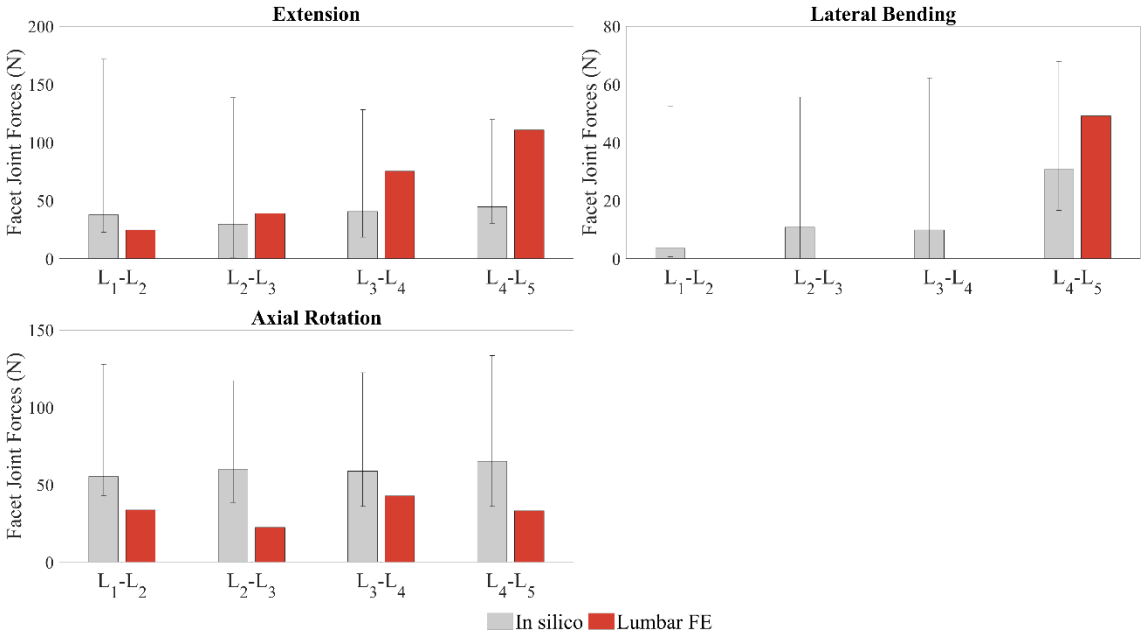

Supplementary Figure 4. Predicted FJF values at different spinal levels of the lumbar spine FE model (with red colour) for (a) extension, (b) lateral bending, and (c) axial rotation for the FE models. The grey bars and their range illustrate the median, minimum, and maximum results of multiple FE models (Dreischarf et al. 2014).

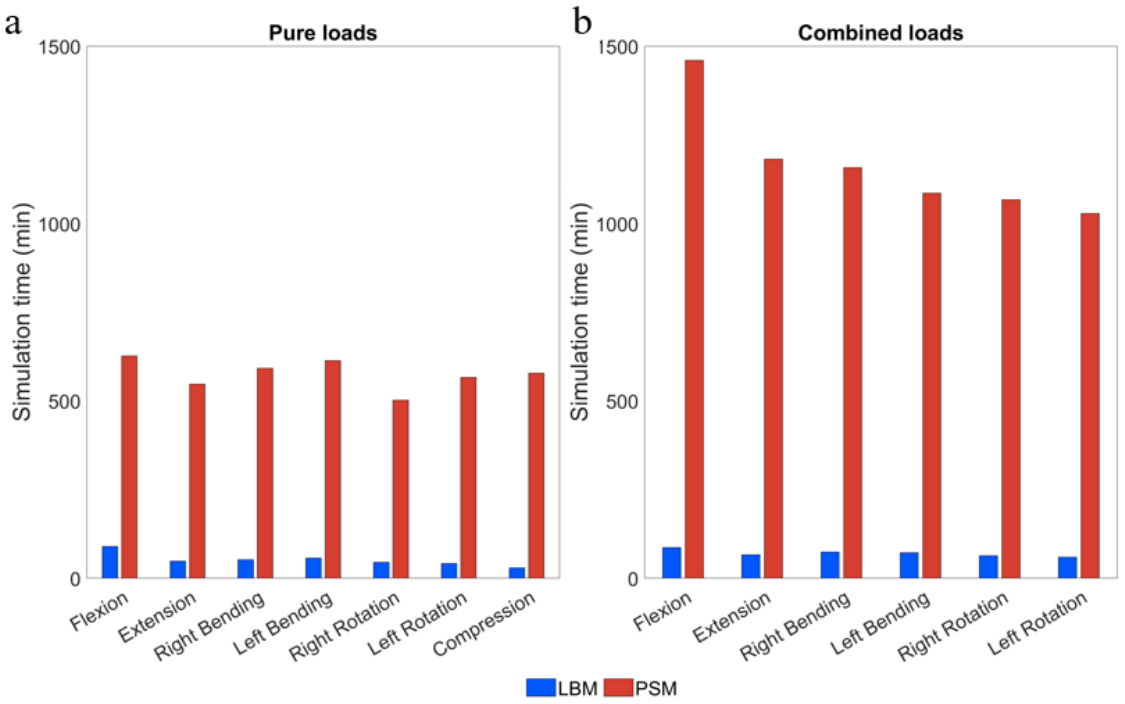

Supplementary Figure 5. Required computational times for the LBM and PSM against (a) pure and (b) combined. Figure from Turbucz M and Pokorni AJ et al. 2022. (Turbucz and Pokorni et al. 2022)

Supplementary Table 2. Weighting factors obtained from the calibration process.

Spinal level	λ_{GS}	λ_{fiber}
T7 - T8	0.32	0.47
T8 - T9	0.28	0.4
T9 - T10	0.3	0.42
T10 - T11	0.5	0.45
T11 - T12	0.5	0.45
T12 – L1	0.5	0.5

λ_{GS} = Calibration factor for the annulus ground substance, λ_{fiber} = Calibration factor for the annulus fibers

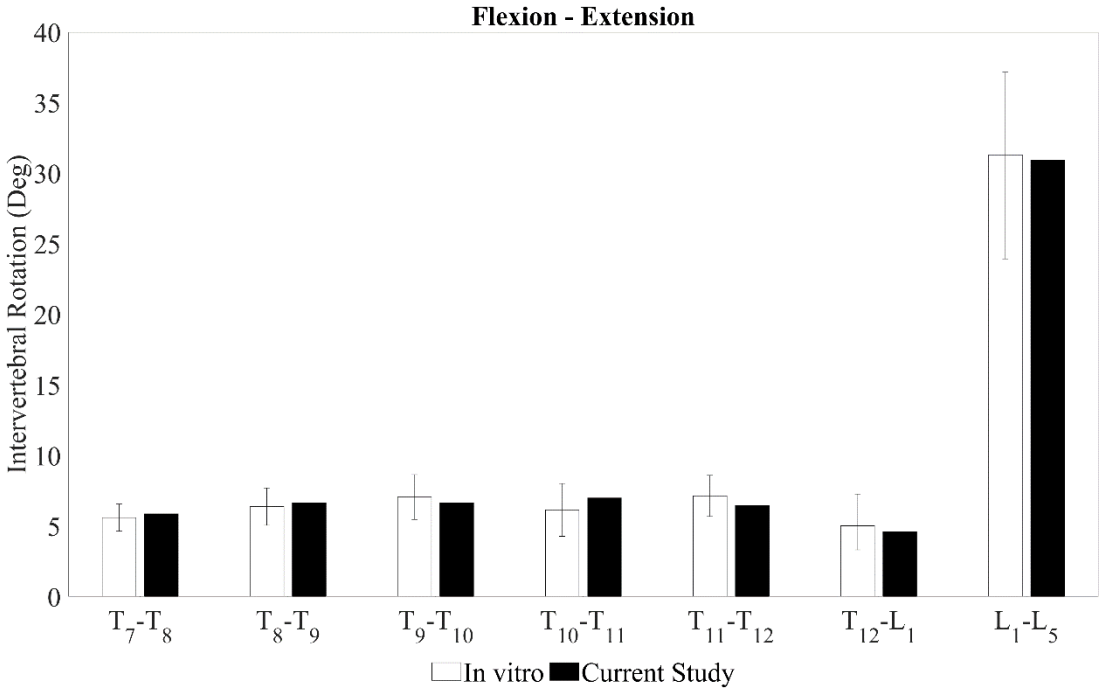

Supplementary Figure 6. Obtained intervertebral rotation angle values in flexion-extension compared to the available in vitro measurements (Rohlmann et al. 2001, Couvertier et al. 2017, Wilke et al. 2017).

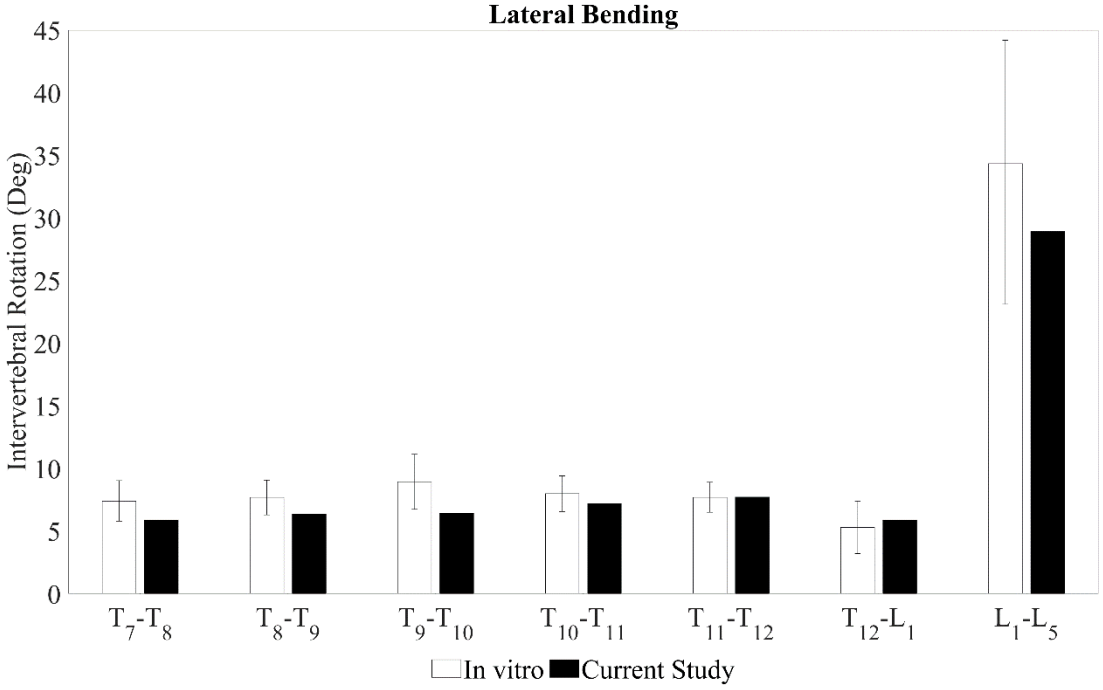

Supplementary Figure 7. Obtained intervertebral rotation angle values in lateral bending compared to the available in vitro measurements (Rohlmann et al. 2001, Couvertier et al. 2017, Wilke et al. 2017).

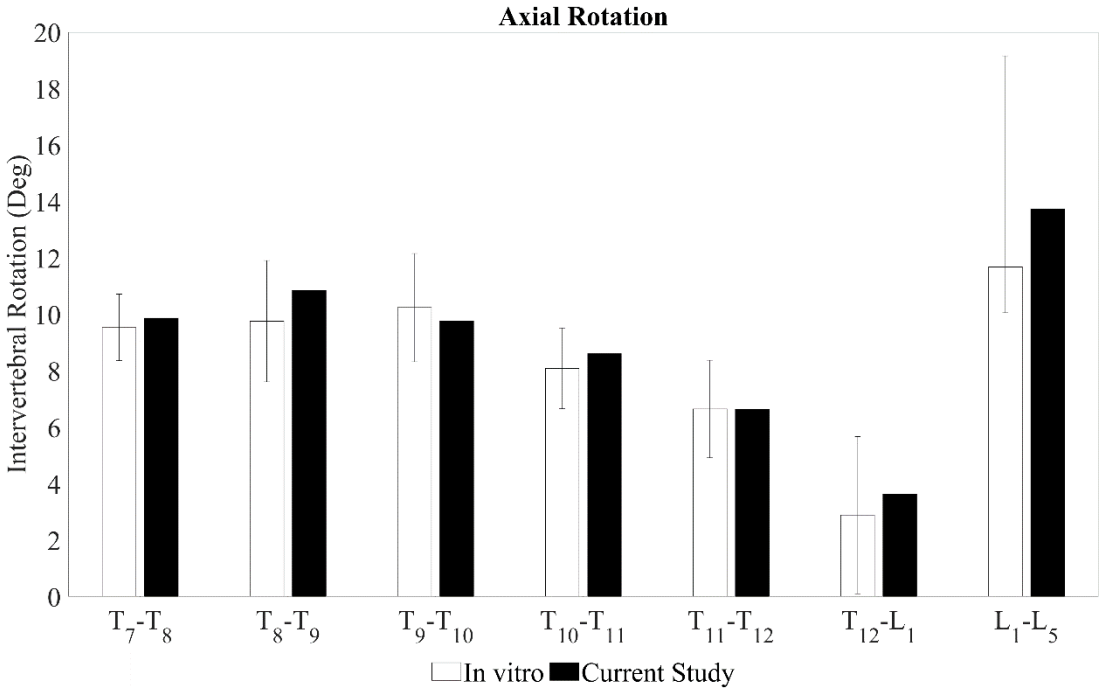

Supplementary Figure 8. Obtained intervertebral rotation angle values in axial rotation compared to the available in vitro measurements (Rohlmann et al. 2001, Couvertier et al. 2017, Wilke et al. 2017).

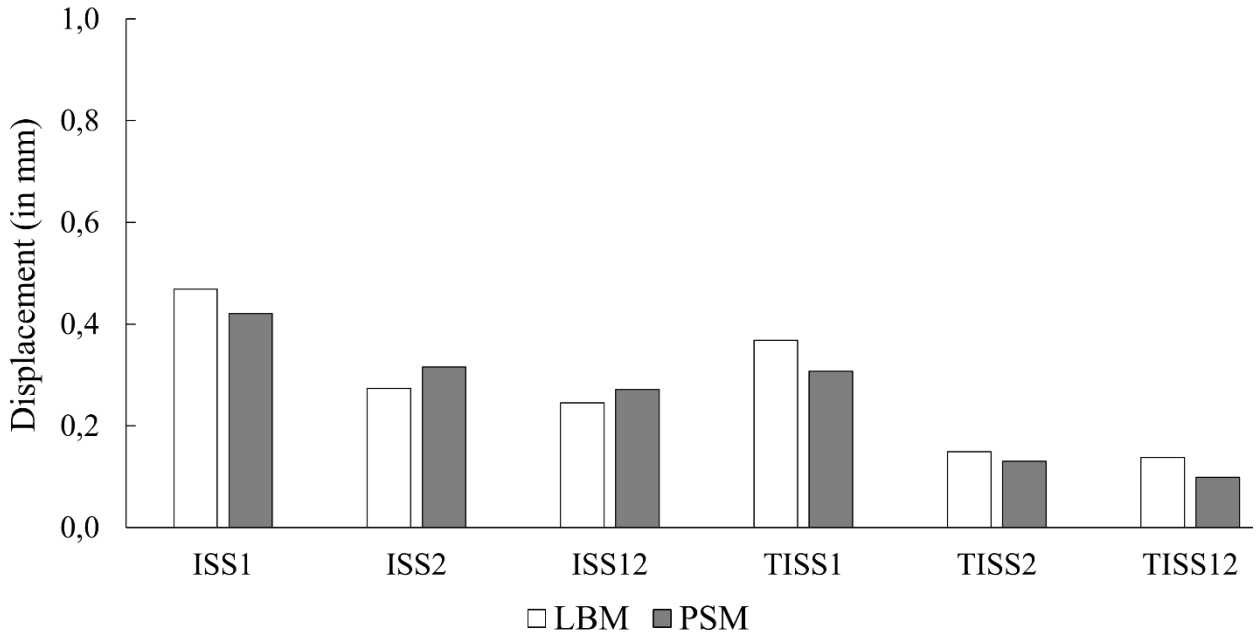

Supplementary Figure 9. Maximum relative interfragmentary displacements on the fracture surface for LBM and PSM.

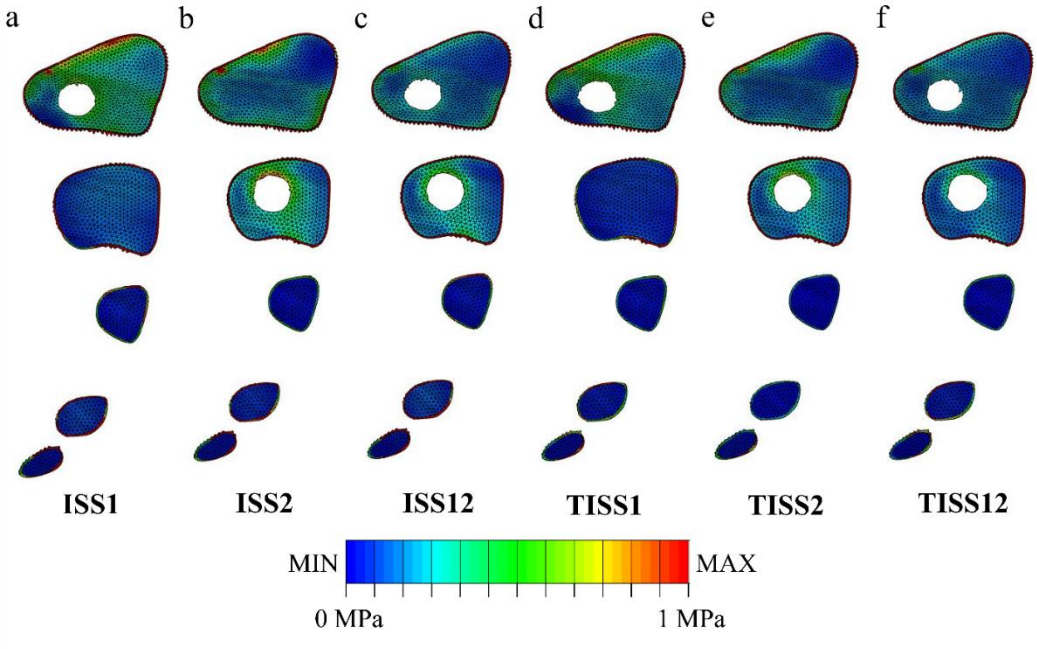

Supplementary Figure 10. Von Mises stress distribution on the fracture surface in the LBM for a) ISS1, b) ISS2, c) ISS12, d) TISS1, e) TISS2), and f) TISS12 with a uniform scale from 0 to 1 in MPa.

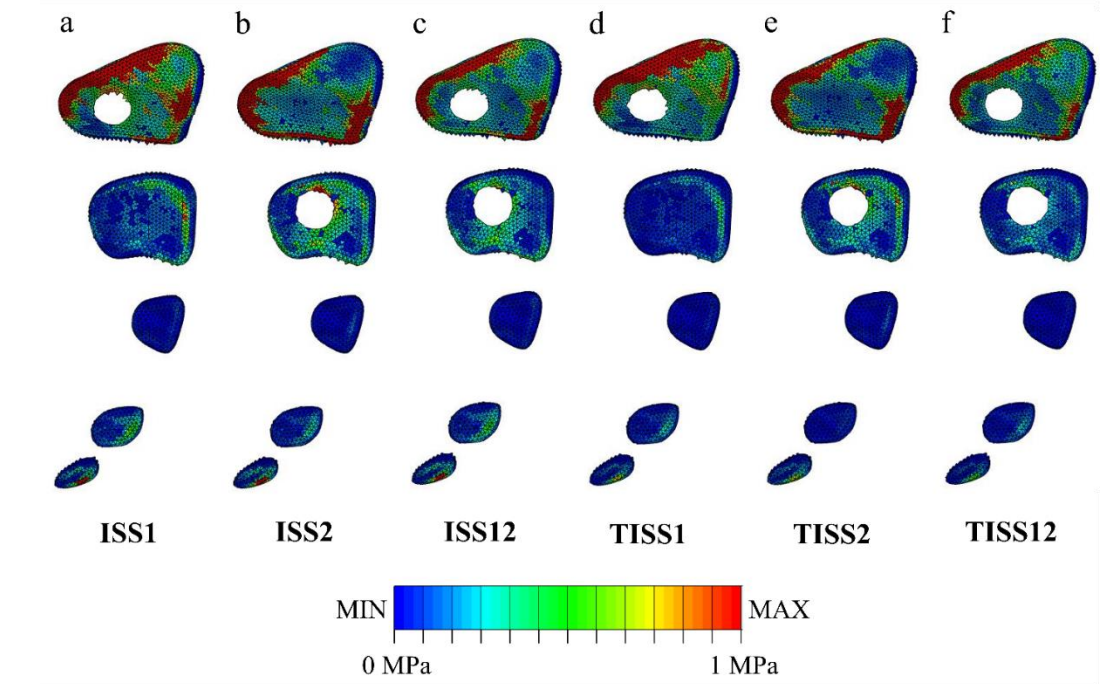

Supplementary Figure 11. Von Mises stress distribution on the fracture surface in the PSM for a) ISS1, b) ISS2, c) ISS12, d) TISS1, e) TISS2), and f) TISS12 with a uniform scale from 0 to 1 in MPa.

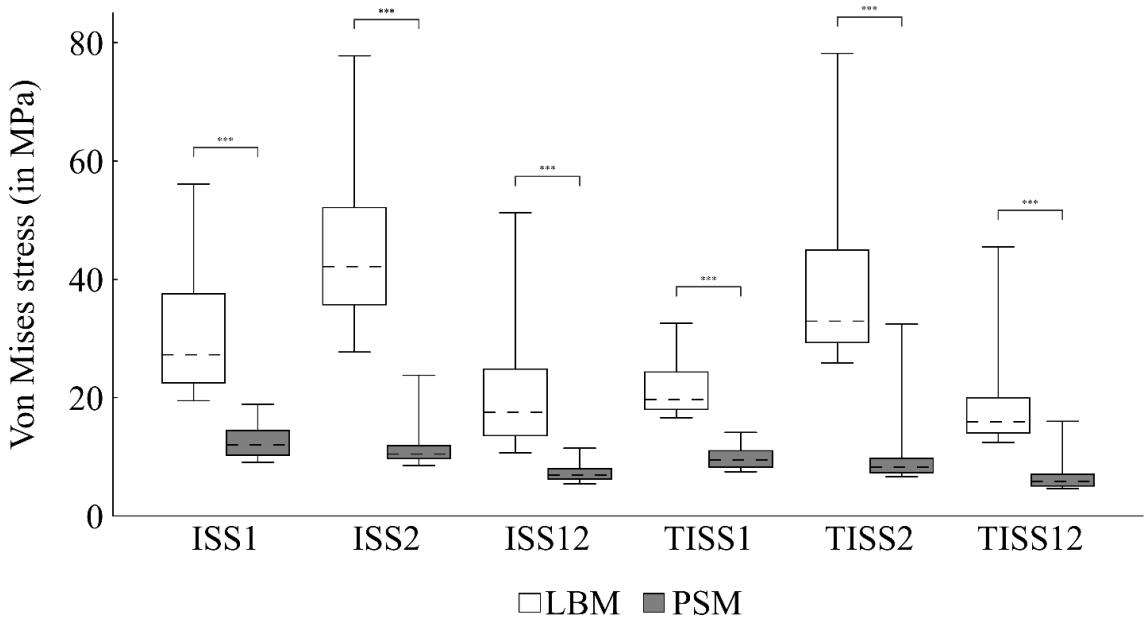

Supplementary Figure 12. Boxplot figure with nodes from LBM and PSM that fell within the largest 1% of the von Mises stress values on the bone-implant surface. Median values are represented with black dashed lines, while minimum and maximum with error bars. (Two-sample Kolmogorov-Smirnov test, *** denotes p-values ≤ 0.001)

Supplementary Study 1 – The biomechanical effect of the connector device

The spinal fixation techniques (SFT) analysed in this PhD thesis use a connector device to join the conventional titanium rod to a less rigid peek rod or multiple thin titanium rods. A theoretical titanium rod fixation (TTRF) technique connecting titanium rod with titanium rod was modelled and compared with the TRF model to evaluate the biomechanical effect of the connector device. Identical boundary and loading conditions were applied: the inferior surface of L5 was fixed, while the load was applied at the superior endplate of the T7 vertebra. Two sets of loading were used to test the fixation techniques. First, a pure bending moment of 5 Nm was applied to measure the intervertebral rotation (IVR) values. Second, the displacement of the TRF model was applied to the TTRF to allow the comparison of the stress values under identical motion.

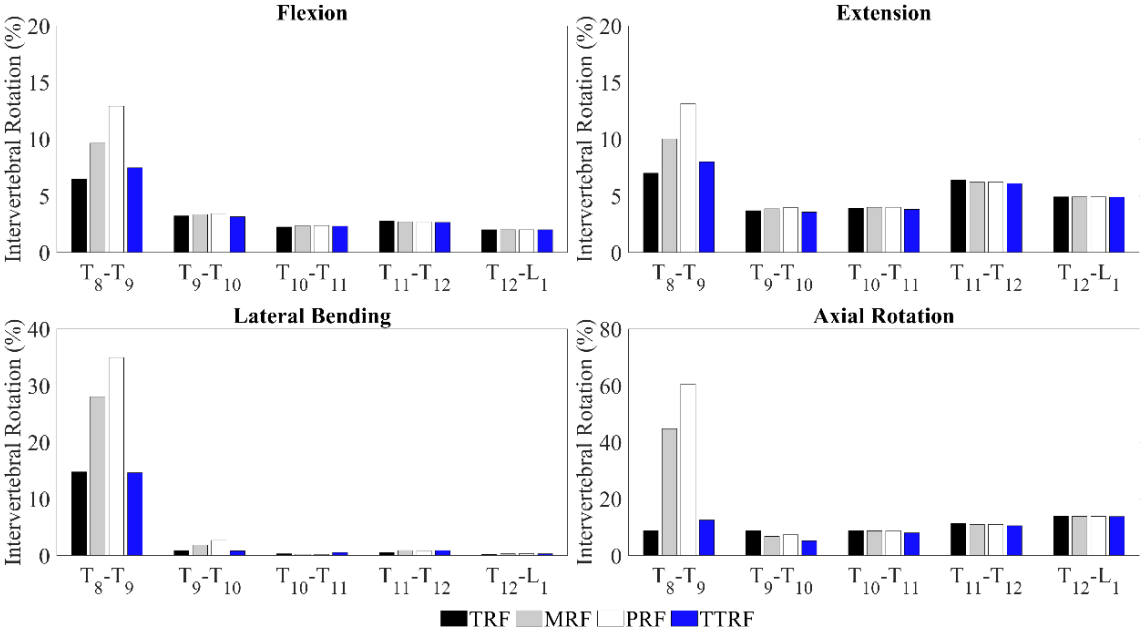

Supplementary Figure 13. Obtained IVR values of the TRF, MRF, PRF and TTRF models in a) flexion, b) extension, c) lateral bending, and d) axial rotation.

In the load-controlled step, the IVR values normalized by the intact spine results were measured for TTRF in addition to the SFTs. At the T8-T9 level, the TTRF model gave 0.99%, 0.99%, and 3.68% larger IVR values than TRF in flexion, extension, and axial

rotation, respectively (Supplementary Figure 13a, b, d). Meanwhile, in lateral bending, the TTRF's IVR was reduced by 0.2% (Supplementary Figure 13c).

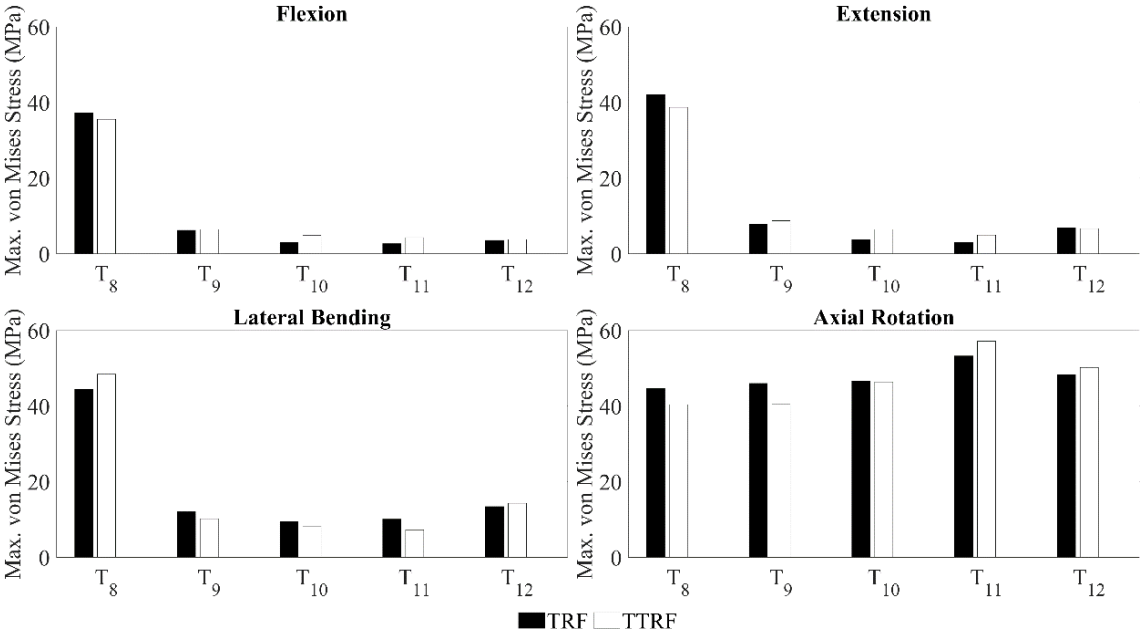

Supplementary Figure 14. Obtained maximum pedicle screw values of the TRF and TTRF models in a) flexion, b) extension, c) lateral bending, and d) axial rotation.

In addition to the IVR predictions, the maximum stress values in the pedicle screws were measured and compared in the displacement-controlled load step (Supplementary Figure 14a-d). At the uppermost instrumented vertebra (UIV), the TTRF model reduced the maximum stress by 1.67 MPa, 3.37 MPa, and 4.18 MPa in flexion, extension, and axial rotation, respectively (Supplementary Figure 14a, b, d). In lateral bending, the maximum stress value was larger in the case of TTRF by 4.05 MPa compared to the TRF model (Supplementary Figure 14c).

The results of this current supplementary study allowed to separate the biomechanical effects of the presence of the connector device from the mechanical properties of SFTs. The results indicate that connecting two titanium rods via a connector device increases mobility and reduces screw stress for flexion, extension, and axial rotation. However, the opposite is observed for lateral bending, i.e., mobility decreases and pedicle stress increases. This phenomenon is not observed in the case of connector devices combined with SFTs, such as the MRF and PRF, as they gave higher mobility and lower stresses in all load directions than the TRF technique. Furthermore, compared to the TTRF, the SFTs

increase mobility substantially more, which is well visualized in Supplementary Figure 13a-d.

In conclusion, although the connector device somewhat increases the upper instrumented segment's mobility, it is much less compared to the mobility of the different SFTs. This highlights that the connector device alone does not significantly influence the mobility and the SFTs are responsible for most mobility increase and load reduction.